Transport Properties of 2-FPTf and TFMSA Monohydrate

by

Mohammed Abdullah

A Dissertation Presented in Partial Fulfillment
of the Requirements for the Degree
Doctor of Philosophy

Approved November 2015 by the
Graduate Supervisory Committee:

Robert Marzke, Chair
Dominic Gervasio
Ralph Chamberlin
Ricardo Alarcon

ARIZONA STATE UNIVERSITY

December 2015

ABSTRACT

Proton and fluorine diffusivity and ionic conductivity of 2-fluoropyridinium triflate (2-FPTf) and proton and fluorine diffusivity, ionic conductivity, and viscosity of trifluoromethanesulfonic acid (TFMSA) monohydrate have been measured over a wide range of temperatures. Diffusivities were measured using the pulsed-gradient spin-echo (PGSE) technique on a 300 MHz NMR spectrometer. Conductivities were measured using electrochemical impedance spectroscopy (EIS) on standard equipment and viscosities were determined using a Cannon-Ubbelohde viscometer. For 2-FPTF, the diffusivity of mobile protons increased from 1.84+/-0.06 x 10(-11) m2/s at 55 degC to 1.64+/-0.05 x 10(-10) m2/s at 115 degC while the diffusivity of 2-fluoropyridine fluorines increased from 2.22+/-0.07 x 10(-11) m2/s at 70 degC to 9.40+/-0.28 x 10(-11) m2/s at 115 degC. For TFMSA monohydrate, the diffusivity of protons increased from 7.67+/-0.23 x 10(-11) m2/s at 40 degC to 3.92+/-0.12 x 10(-10) m2/s at 110 degC while the diffusivity of fluorines increased from 4.63+/-0.14 x 10(-11) m2/s at 40 degC to 2.79+/-0.08 x 10(-10) m2/s at 110 degC, protons diffusing approximately 1.5 times faster than fluorines over the entire temperature range. NMR spectra indicate that proton diffusion occurs via direct hopping from TFMSA molecule to molecule. The conductivity of 2-FPTf varied from 0.85+/-0.03 mS/cm to 35.9+/-1.08 mS/cm between 25 and 110 degC. The conductivity of TFMSA monohydrate varied from 6.60+/-0.2 mS/cm to 84.6+/-2.5 mS/cm between 23 and 139 degC and its viscosity varied from 27.5+/-1.4 mPa.s to 4.38+/-0.22 mPa.s between 49 and 121.5 degC, in good agreement with literature values. Temperature dependences of the measured properties showed Arrhenius behavior with activation energies for proton diffusion, fluorine diffusion and ionic

conduction for 2-FPTf above the melting point of 16.9+/-0.8 kJ/mol, 48.0+/-2.4 kJ/mol and 27.8+/-1.4 kJ/mol respectively. Activation energies for proton diffusion, fluorine diffusion, ionic conduction and viscosity for TFMSA monohydrate were 23.4+/-1.2 kJ/mol, 26.0+/-1.3 kJ/mol, 22.1+/-1.1 kJ/mol, and 26.9+/-1.3 kJ/mol respectively. The degree of dissociation of the charged species, calculated using the Nernst-Einstein relation, varied from 13 to 24% for 2-FPTf and from 25 to 29% for TFMSA monohydrate over the temperature range.

DEDICATION

To my parents

ACKNOWLEDGMENTS

I would like first to thank my supervisor, Dr. Robert F. Marzke for his guidance and patience during my Ph.D. study at ASU. The research in this thesis could not be done without his invaluable knowledge and encouragement.

I would also like to thank the assistance from all the faculty members who have served as my committee: Dr. Dominic Gervasio, Dr. Ralph Chamberlin and Dr. Ricardo Alarcon.

I would like to thank Dr. Gervasio specially for helping me make the 2-FPTf samples.

Finally, I would like to thank all the staff working for the Physics Department, who have always been supportive, and who made the experience of studying great at the Physics Department of ASU.

TABLE OF CONTENTS

Page

CHAPTER Page

CHAPTER Page

CHAPTER Page

CHAPTER Page

CHAPTER Page

LIST OF TABLES

LIST OF FIGURES

Table Page

Table Page

Table Page

Table Page

MOTIVATION FOR THIS THESIS

In recent years, there has been a revolution in the field of ionic liquids research. Ionic liquids, formerly known as molten salts, are salts that usually exist in liquid phase well below room temperature up to a temperature as high as 200°C. In these media a variety of organic and inorganic solutes dissolve partially or completely into separated anions and cations. In addition to being outstandingly good solvents, their extremely low vapor pressure makes them desirable "green" substitutes for traditional industrial solvents, in particular volatile organic compounds, a major source of industrial pollutants.

Protic ionic liquids are a class of ionic liquids with interesting properties and applications. They are produced through the combination of a Brønsted acid and a Brønsted base. The key property that distinguishes protic ionic liquids from other ionic liquids is proton transfer from acid to base. This leads to the presence of proton-donor and proton-acceptor sites, which can be used to build up a hydrogen-bonded network. Due to their protonic conductivity, protic ionic liquids are being investigated as proton conducting media used for proton exchange membrane (PEM) fuel cells.

Currently, Nafion® (Fig. 1, (a)) by DuPont is the most widely used proton conductor for PEM fuel cells. It is a perfluorinated synthetic polymer with ionic properties (an ionomer) and consists of a hydrophobic Teflon backbone with pendant side chains terminating with perfluoromethylsulfonic acid groups ($-CF_2SO_3H$). These sulfonic acid functional groups are hydrophilic and preferentially hydrated. The Nafion membrane functions as both an electrode separator and an electrolyte in the fuel cell, because it is an electron insulator and, when properly hydrated, a proton conductor. The internal resistance and overall performance of the fuel cell are strongly influenced by the membrane's proton

conductivity, which itself is a function of hydration. Extensive experimental measurement of the electro-osmotic drag coefficient (the number of water molecules carried across the membrane per proton transported) for various sulfonated membranes over a wide range of water content has suggested that the proton transport is dominated by sulfonic acid and water interactions.

One drawback of hydrated PEM's is that they cannot operate above 100°C as water boils and the membrane becomes dry. Neat (water-free) ionic liquids are being investigated as alternatives over conventional water bases acid electrolytes for fuel cell operations. Dr Gervasio's group has synthesized and studied several neat protic ionic liquids under fuel cell conditions. Among them, 2-fluoropyridinium triflate (2-FPTf) showed the highest conductivity and the best fuel cell performance. We have investigated, for the first time, the transport properties of 2-FPTf over a wide range of temperatures. Our measurements can improve our understanding of the mechanism of proton conduction in neat protic ionic liquids. To understand this complex process in hydrated PEM's at a molecular level, we have also investigated the transport properties (diffusivity, conductivity, and viscosity) of trifluoromethanesulfonic acid monohydrate (abbreviated as TFMSA monohydrate or $CF_3SO_3H:H_2O$). TFMSA monohydrate can model many properties of hydrated Nafion, and our measurements can improve our understanding of the mechanism of proton conduction in Nafion.

CHAPTER 1

THEORETICAL BACKGROUND

1.1 Basics of NMR

1.1.1 NMR

Nuclear magnetic resonance (NMR) originally referred to a physical phenomenon that occurs when nuclei with intrinsic magnetic dipole moments are immersed in a static magnetic field and experience interactions with other time-dependent magnetic fields, leading to the absorption and emission of electromagnetic oscillations. Whether any given nucleus will experience this phenomenon depends upon a property called spin. Spin can be thought of as a small angular momentum $\hbar\mathbf{I}$ associated with a magnetic moment $\boldsymbol{\mu}=\hbar\gamma\mathbf{I}$, where γ is a characteristic property giving the size of the moment, typically in ergs/gauss (or in N-m^2) of the nucleus. Motions of $\boldsymbol{\mu}$ in magnetic fields produce the observed electromagnetic oscillations. Not all nuclei possess spin. All isotopes that contain an odd number A of protons and neutrons have an intrinsic magnetic moment and angular momentum, leading to a half-integer spin, while all nuclides with even numbers of both have a total integer spin usually 0 or 1 in stable nuclei. The most commonly studied nuclei in NMR in chemistry are ^{1}H and ^{13}C,which have spin ½, although nuclei from isotopes of all stable odd-A isotopes of elements have been observed by high-field NMR spectroscopy as well.

1.1.2 History

In the 1920's, quantum theory was used to explain atomic spectral phenomena where classical mechanics failed. This theory, initially proposed by Bohr in 1913, was essential

to the understanding of optical absorption and emission spectra of atoms. In 1922 Stern and Gerlach carried out atomic and molecular beam experiments which revealed a new aspect of matter, the intrinsic angular momentum called spin, whose properties obeyed the rules of quantum theory and could only be understood by its use. A beam of silver atoms was formed in high vacuum and passed through an inhomogeneous magnetic field, splitting the beam into two components that revealed the existence of half-integral intrinsic angular momenta, having only two time-independent directions of their momenta in the field. In 1925, Uhlenbeck and Goudsmit introduced the quantum mechanical concept of spin with a resultant angular momentum that gave rise to the electron's intrinsic magnetic dipole moment. In 1926 Schrodinger and Heisenberg formulated quantum mechanics. This new branch of quantum physics replaced the old quantum theory. In 1927 Pauli and Darwin included electron spin in quantum mechanics and in 1928 Dirac gave its theoretical explanation in terms of his relativistic quantum mechanical equation. Then, in 1933 Stern and Gerlach measured the effect of nuclear spin by increasing the sensitivity of their molecular beam apparatus, enabling them to detect nuclear magnetic moments. They observed and measured the deflection of a beam of hydrogen molecules. In 1936, the Dutch physicist C. J. Gorter used the resonance property of nuclear spin in the presence of a static magnetic field to study nuclear paramagnetism. Although his experiment was unsuccessful, the results were published and this brought attention to the potential of resonance methods. In 1937, Rabi predicted and observed nuclear magnetic resonance in an experiment involving passing a beam of LiCl through a strong static magnetic field where a smaller oscillating magnetic field was then applied at right angles to the initial field. When the frequency of the oscillating field

approached the Larmor frequency of the precessing Li nucleus in the static field, resonant absorption of energy by the nuclei of Li occurred. The absorption of energy was recorded as a dip in the beam intensity as the static magnetic field's current was increased. In 1943, Otto Stern was awarded the Nobel Prize in physics for his contribution to the development of the molecular beam method and discovery of the magnetic moment of the proton. In 1944 Rabi was awarded the Nobel Prize in physics for his work in molecular beams, especially the resonance method. In 1945, at Harvard, Purcell, Torey and Pound observed NMR in a bulk material (1 kg of paraffin wax) by assembling an apparatus designed to detect transitions between nuclear magnetic energy levels using radiofrequency methods. In 1952 Bloch and Purcell shared the Nobel Prize in physics for their development of new methods for nuclear magnetic precession measurements and discoveries in connection therewith. In 1953, A. Overhouser predicted that a small alteration in the electron spin populations will produce a large change in the nuclear spin population. This theory was later named the Overhouser effect and is now a very important tool for the determination of complex molecular structure. In 1957 P. Lauterbur and C. Holm independently recorded the first ^{13}C NMR spectra in an organic liquid compound. Despite the low natural abundance of the NMR- active isotope, the recorded spectra showed a signal to noise ratio as high as 50. This was owing to the extremely narrow width of the line caused by the rapid Brownian motion of the molecules of the liquid.

1.1.3 Spin

Spin is a fundamental property of nature like electrical charge or mass. It is an intrinsic form of angular momentum carried by elementary particles, composite particles, and

atomic nuclei. The existence of spin angular momentum is inferred from experiments, such as the Stern-Gerlach experiment, in which particles are observed to possess angular momentum that cannot be accounted for by orbital angular momentum alone. Spin comes in multiples of half ħ, and its projection along a magnetic field can be positive or negative. Individual unpaired electrons, protons, and neutrons each possess a spin one half. Two or more particles with spins having opposite signs can pair up to eliminate the observable manifestations of spin. In nuclear magnetic resonance, only unpaired nuclear spins can be observed.

1.1.4 Properties of Spin

When placed in a magnetic field of strength B, a particle with a net spin and its associated magnetic moment $\boldsymbol{\mu}$ can absorb a photon, of frequency ν. The frequency ν depends on the gyromagnetic ratio, γ of the particle, which is a characteristic of any given nucleus, varying from the largest – that of ^{1}H, the proton – down to much smaller values. These values have been studied and modeled in nuclear theory, and their origins are reasonably well understood. This absorption and emission frequency is characteristic of the Larmor precession of the nuclear magnetic moment in a static magnetic field, which is directly observed in current NMR spectrometers from the small Faraday induction emfs that it produces in radio-frequency receivers. These emfs are amplified and observed in real time, following application of radio-frequency pulses very close to the Larmor frequency. The r.f. pulses induce the Larmor precession, and the highly accurate measurement of electromagnetic signal frequencies allows extremely accurate measurement of values of γ, to parts per billion. This accuracy in turn allows observation of multiple effects that are orders of magnitude smaller than those produced solely by strong external magnetic field

$\mathbf{B_0}$, involving for example very weak fields due to the electrons in the atom containing the nucleus or to the presence of other nuclei in close proximity in a molecule. It is this accuracy that accounts for much of the importance of NMR in the study of bulk matter, especially with regard to molecular structure.

The units in which γ is expressed arise from the Zeeman energy of interaction of $\boldsymbol{\mu}$ with an external magnetic field **B,** which has the familiar form $-\boldsymbol{\mu}.\mathbf{B}$. This leads to a frequency proportional to B, from the quantum mechanical relation between energy and frequency $E = h\nu = \hbar\omega$:

$$\hbar\omega = -\gamma\hbar\mathbf{I}.\mathbf{B} \qquad (1.1)$$

In a static field $\mathbf{B_0} = B_0\mathbf{k}$ (along the field axis **k**):

$$\hbar\omega = -\gamma\hbar I_z B_0 \qquad (1.2)$$

This gives two stationary energy states for spin I = ½ , where the expectation values of I_z are $\pm 1/2$, and the spin is oriented parallel or antiparallel to the field, with the parallel orientation at the lower energy. The energies are $E(+/-) = \mp\gamma\hbar B_0/2$ and their angular frequency difference is $\hbar\Delta\omega = \hbar\gamma B_0 \Rightarrow \Delta\omega = \gamma B_0$. Emission and absorption between these two stationary states thus occur at the Larmor frequency $\nu = \frac{\gamma}{2\pi}B_0$. The dynamical equation of motion of the spin in a field $\mathbf{B_0}$ when it is not oriented along the Z axis is given by classical mechanics:

$$\frac{d}{dt}(\hbar\mathbf{I}) = \boldsymbol{\mu} \times \mathbf{B} = \hbar\mathbf{I} \times \mathbf{B_0}, \qquad (1.3)$$

which leads to the Larmor precession of the expectation values observed for **I**, which are time-dependent. The frequency of this precession motion is exactly $\omega = \gamma B_0$ (in either Gaussian of SI units for γ or B_0).

Some of the nuclei routinely used in NMR are listed below.

Table 1.1: Nuclei routinely used in NMR

Nuclei	Unpaired Protons	Unpaired Neutrons	Net Spin	γ (10^6 rad s^{-1} T^{-1})
^{1}H	1	0	1/2	267.51
^{2}H	1	1	1	41.07
^{31}P	1	0	1/2	108.29
^{23}Na	1	2	3/2	70.76
^{14}N	1	1	1	19.33
^{13}C	0	1	1/2	67.26
^{19}F	1	0	1/2	251.66
^{27}Al	1	0	5/2	69.76
^{29}Si	1	0	1/2	-53.19

To understand in more detail how particles with spin behave in a magnetic field $\mathbf{B_0}$, consider a proton. When the proton is placed in an external magnetic field, the magnetic moment vector $\boldsymbol{\mu}$ of the particle aligns itself with the external field as does the spin vector

I. From quantum mechanics, there is a low energy state where the spin is aligned and a high energy state where the spin is opposite to the magnetic field.

This proton can undergo a transition between the two energy states by the absorption of a photon. A particle in the lower energy state absorbs a photon and ends up in the higher energy state. The energy of this photon must nearly match the energy difference between the two states (an emitted photon will exactly match this difference). As outlined above, then, the energy E, of the photon is related to its frequency, ν, by Planck's constant h, so that:

$$E = h\nu = \hbar\omega = \hbar\gamma B_0 \qquad (1.4)$$

In NMR, the quantity ν is called either the resonance frequency or the Larmor frequency. The energy of the two spin states is represented on a two-level energy diagram. Since $\nu = \frac{\gamma}{2\pi} B$ and $E = h\nu$, the energy of the photon needed to cause a transition between the two spin states is:

$$E = h\frac{\gamma}{2\pi}B_0 = \hbar\omega_0 \qquad (1.5)$$

When the energy of the photon matches the energy difference between the two spin states, absorption of energy occurs. In the NMR experiment, the frequency of the photon, ν is in the radio frequency range. For the hydrogen nuclei, ν is commonly between 60 and 800 MHz, depending on the size of B_0.

When a group of spins is placed in a magnetic field, each spin aligns in one of the two possible orientations, the lower energy level, N^+, and the higher energy level, N^-. From Boltzmann statistics:

$$N^-/N^+ = e^{-E/kT} \quad (1.6)$$

Here E is the difference in energy between the two states, k is the Boltzmann's constant, and T is the absolute temperature. As the temperature decreases, so does the ratio N^-/N^+. As the temperature increases, the ratio approaches one. At room temperature, N^+ is only slightly higher than than N^-, owing to the small value of E in even the largest B_0 fields, but this slight difference allows a net NMR signal from a sample to be observed, even at high temperature.

This signal results from the difference between the energy absorbed by the lower-state spins, which make a transition from the lower energy state to the higher energy state and the energy emitted by the by the upper-state spins. The signal is proportional to the population difference between the energy states and is thus quite small, resulting in a Curie-Law temperature dependence.

1.1.5 Macroscopic Aspects of Nuclear Magnetism

In all magnets there is some spatial inhomogeneity of the field, which is kept as small as possible. Here we consider a packet of spins experiencing the same magnetic field strength. At any instant in time, the magnetic moments of the N spins in each spin packet can be represented by a magnetization vector. The size of each magnetization vector is proportional to $(N^+ - N^-)$ with N^+ spins along the field and N^- spins against the field. The vector sum of the magnetization vectors from all of the spin packets is the net magnetization, always used in describing pulsed NMR. Adapting the conventional NMR coordinate system, the external magnetic field and the net magnetization vector at equilibrium are both along the Z axis.

1.1.5.1 T_1 Processes

At equilibrium, the Z component of magnetization M_Z of all the packets, referred to as the longitudinal magnetization, equals M_0. There is no transverse ($M_X + M_Y$) magnetization in this case. It is possible to change the net magnetization by exposing the nuclear spin system to radio frequency energy of a frequency equal to the energy difference between the spin states. If enough energy is put into the system, it is possible to saturate the spin system and make $M_Z = 0$. The time constant which describes how M_Z returns to its equilibrium value after saturation is called the spin lattice relaxation time (T_1). The equation governing this behavior as a function of time t after the application of a static B_1 magnetic field is:

$$M_Z = M_0 (1 - e^{-t/T1}) \qquad (1.7)$$

T_1 is therefore defined as the time required to change the Z component of magnetization by a factor of e. If the net magnetization were to be initially placed along the –Z axis, by application of an inverting r.f. pulse it will gradually recover its equilibrium position along the +Z axis at a rate governed by T_1. The equation governing this behavior as a function of the time t after its displacement is:

$$M_Z = M_0 (1 - 2e^{-t/T1}) \qquad (1.8)$$

1.1.5.2 T_2 Processes

If the net magnetization is placed in the XY plane however, the equations of motion for the transverse magnetization show that it will rotate about the Z axis at the Larmor frequency, in addition to decaying by processes described next. The rotation does not last indefinitely. In addition to precession, the observed net magnetization starts to decrease

as the spin packets, each of which rotates at its own Larmor frequency if the field is not perfectly homogeneous, begin to dephase. The longer the elapsed time, the greater the phase difference between the packets, resulting in a loss of signal from the *inhomogeneous broadening* of the NMR signal's precession frequency. This can sometimes be represented as an exponential decay, with a time constant $T_{inhomogeneous}$. There is also another important mechanism giving rise to signal loss, however, arising from the nuclear spins' random magnetic interactions with one another, which are largely magnetic dipolar in nature. These interactions result in a loss of magnetization of each of the individual spin packets themselves. The loss, generally exponential with time, occurs with a characteristic decay time T_2. This decay time also leads to a broadening of the precession frequency line, by the uncertainty principle, which is known as *homogeneous broadening*.

The total decay of the magnetization may be written conceptually as:

$$M_{XY} = M_{XYo}\, e^{-t/T2^*} \qquad (1.9)$$

with:

$$1/T_2^* = 1/T_2 + 1/T_{2inhomogeneous} \qquad (1.10)$$

There are thus two factors that govern the decay of transverse magnetization: (1) molecular-level spin-spin interactions (T_2 processes) and inhomogeneities in the magnetic field (acting on the spins).

T_1 and T_2 processes are usually thought of as processes occurring separately. However they may also occur simultaneously, the only restriction being that T_2 is less than or equal to T_1.

1.1.6. Pulsed. Oscillating Magnetic Fields

A coil of wire placed around the X axis in the laboratory frame will provide a magnetic field along the X axis when a direct current is passed through the coil. An alternating current will produce a magnetic field that alternates in direction. In a frame of reference rotating about the Z axis at a frequency ω equal to that of the alternating current, known as the rotating frame (in all of NMR), having axes X', Y' and $Z'=Z$, the radio frequency is often chosen along the X' axis and will be constant. In magnetic resonance, the oscillating magnetic field created by the coil passing an alternating current near the Larmor frequency is called the B_1 magnetic field. When the alternating current through the coil is turned on and off, it therefore creates in the rotating frame a pulsed static magnetic field B_1 along the X' axis. If the radio frequency ω is set independently equal to the Larmor frequency ω_0, the spins respond to this pulse in the rotating frame in such a way as to cause the net magnetization vector to rotate about the direction of the applied B_1 field, which is static in this frame. The rotation of M thus occurs at a frequency $\omega_1=\gamma B_1(=\gamma H_1)$ in the rotating frame. The rotation angle depends on the length of time the field is on, τ, and its magnitude B_1.

$$\theta = 2\pi \gamma \tau B_1 \qquad (1.11)$$

In NMR experiments, τ is much smaller than T_1 and T_2, of the order of microseconds.

A 90° pulse is one which rotates the magnetization vector clockwise by 90 degrees about the X' axis. It is most directly produced when ω is set $=\omega_0$, called setting the radio frequency "on resonance". A 90° pulse then rotates the equilibrium magnetization down to the Y' axis (according to equation 1.11 above). In the laboratory

frame the equilibrium magnetization spirals down around the Z axis to the XY plane. Thus the rotating frame of reference is very helpful in describing the behavior of magnetization in response to a pulsed oscillating magnetic field.

Now, however a 180° pulse can be applied if desired. It rotates the magnetization vector by 180 degrees and is affected by a pulse duration τ twice as long as that at eq. n. In general, the net magnetization at any orientation will behave according to the rotation equation. For example, a net magnetization vector along the Y' axis will end up along the $-Y'$ axis when acted upon by a 180° pulse of B_1 along the X' axis. A net magnetization vector between X' and Y' will end up between X' and $-Y'$ after application of a 180° pulse of B_1 applied along the X' axis.

A rotation matrix can be used to predict the result of a rotation. Here, θ is the rotation angle about the X' axis, $[X' \quad Y' \quad Z]$ is the initial location of the vector, and $[X'' \quad Y'' \quad Z'']$ the location of the vector after the rotation. Here $\theta=\omega_1 t$ in the rotating frame (on resonance).

$$\begin{bmatrix} X'' \\ Y'' \\ Z'' \end{bmatrix} = \begin{bmatrix} 1 & 0 & 0 \\ 0 & \cos\theta & \sin\theta \\ 0 & -\sin\theta & \cos\theta \end{bmatrix} \begin{bmatrix} X' \\ Y' \\ Z \end{bmatrix} \qquad (1.12)$$

1.1.6.1. Free Induction Decay (FID)

After we apply an r.f. pulse, there is a component of magnetization M in x-y plane that precesses around the ambient field. The Larmor precession leads to an induced emf in a detection coil (in the x-y plane). The spin polarization dissipates because of both spin-spin relaxation and inhomogeneity of the magnetic field. The decreasing signal is called free induction decay (FID) (Figure 1.1 (a)). The NMR spectrum is the Fourier transform

of the FID (Figure 1.1 (b)), and it provides information about nuclei, such as their Larmor precession frequency and relative numbers of nuclear spins in a sample.

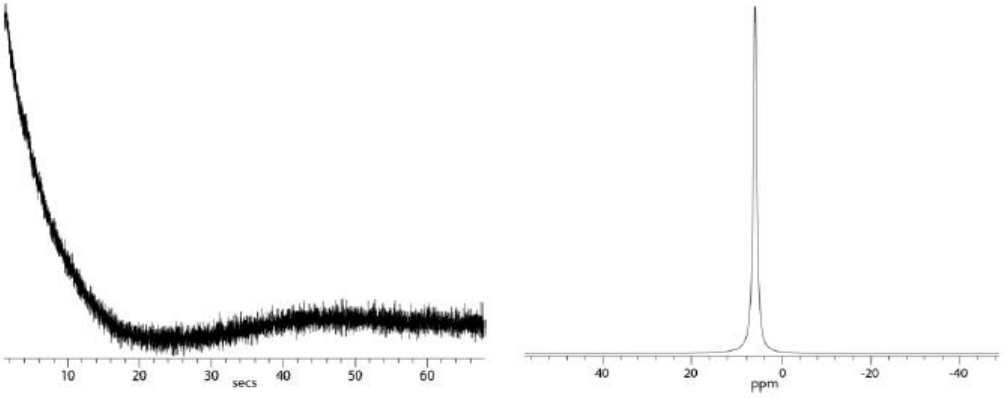

(a) **(b)**

Figure 1.1 (a) On-resonance Free Induction Decay (FID) (b) NMR spectrum (Fourier Transform of FID)

1.1.6.2 Bloch Equations

The Bloch equations are a set of macroscopic coupled differential equations that are used to describe the behavior of a magnetization vector under any conditions. When integrated, the Bloch equations will yield the X', Y', and Z components of magnetization as a function of time (when relaxation times T_1 and T_2 are present). The Bloch equations in rotating frame of reference with an applied radio frequency B_1 along the X' axis are as follows:

$$\frac{dM_{x'}}{dt} = (\omega_0 - \omega)M_{y'} - \frac{M_{x'}}{T_2} \qquad (1.13)$$

$$\frac{dM_{y'}}{dt} = -(\omega_0 - \omega)M_{x'} + 2\gamma B_1 M_z - \frac{M_{y'}}{T_2} \quad (1.14)$$

$$\frac{dM_z}{dt} = -2\gamma B_1 M_{y'} - \frac{(M_z - M_{z0})}{T_1} \quad (1.15)$$

1.1.7 Chemical Shift

When an atom is placed in a magnetic field, B_0, its electrons circulate about the direction of the applied magnetic field. This circulation causes a small magnetic field at the nucleus which opposes the externally applied field by Lenz's law. The effective magnetic field at the nucleus, $B_{eff.}$, is therefore generally less than the applied field by a small fraction σ, of order 10^{-6}.

$$B_{eff.} = B_0 (1-\sigma) \quad (1.16)$$

This is called shielding. In some cases, such as the benzene molecule, the circulation of the electrons in the aromatic π orbitals creates a magnetic field at the hydrogen nuclei which enhances the B_0 field. This is called deshielding. The electron density around each nucleus in a molecule varies according to the type of the nuclei and bonds in a molecule or solid. The opposing field and therefore the field acting on each nucleus will vary, with each compound. This is called the chemical shift. For example, with a molecule having two types of nuclei, the resonance frequencies of the two nuclei will differ. This difference will moreover depend linearly on the strength of the magnetic field B_0. The greater the value of B_0, the greater the frequency difference. This relationship makes it difficult to compare NMR spectra taken on spectrometers operating at different field strengths. Also, the very high accuracy of NMR frequency measurement leads to a range of chemical shift values for the same element, for example about 20 ppm for hydrogen

(^{1}H) and as much as 400 ppm for ^{13}C. To avoid these problems, the chemical shift of a nucleus is taken as the difference between the observed resonance frequency of a nucleus and the frequency observed for the same nucleus in a standard substance, relative to the standard's frequency. This quantity is expressed in ppm, owing to the small size of chemical shifts, and given the symbol δ. Thus:

$$\delta = (\nu - \nu_{Ref}) \times 10^6 / \nu_{Ref} \quad (1.17)$$

In NMR spectroscopy of liquids, standard frequencies for ^{1}H, ^{13}C, and ^{29}Si are those of the highly stable compound tetramethylsilane, $Si(CH_3)_4$ or TMS. For solids such as phosphates, silicates and aluminosilicates, solution standards contanining ^{31}P, ^{29}Si, or ^{27}Al are employed.

1.1.8.1 T_1 Measurement

The method of inversion recovery (IR) is used to measure longitudinal relaxation time.The IR sequence is usually composed of a 180° pulse followed by a 90° pulse, with a variable time interval τ between the two pulses (Figure 1.2(a)). First, the 180° inverts the magnetization. During the subsequent time interval the magnetization experiences longitudinal relaxation recovering towards its value prior to the 180° pulse, but in this recovery no signal can be detected because there is no magnetization component in the x-y plane. The 90° pulse then rotates magnetization into the x-y plane, which produces an NMR signal. The intensity of signal depends on the time interval between 180° pulse and 90° pulse (Figure 1.2 (b)), according to the equation:

$$M(\tau) = M_0(1 - 2e^{\frac{-\tau}{T_1}}) \quad (1.18)$$

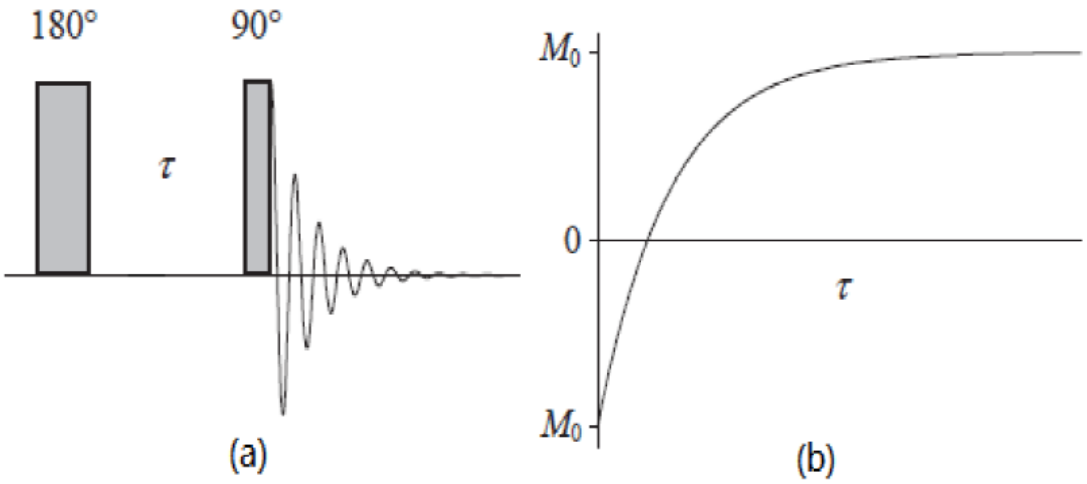

Figure 1.2 (a) Pulse sequence for inversion recovery; (b) the evolution of magnetization with variable time interval τ

T_1 may also be determined from a 90-FID or spin-echo sequence which is repeated at various repetition times (T_R). For instance, if the 90-FID sequence is repeated many times at T_{R1} and then many times at T_{R2}, T_{R3}, and so on, the plot of signal amplitude or integrated Fourier transform area as a function of T_R will be an exponential growth of the form:

$$S=k(1-e^{\frac{T_R}{T_1}}) \qquad (1.19)$$

The data may be fit to obtain T_1.

1.1.8.2 T_2 Measurement

Measurement of the spin-spin relaxation time requires the use of a spin-echo sequence (Hahn 1950). The spin echo sequence is composed of a 90° pulse and a 180° pulse, the time interval τ between 90° pulse and 180° pulse determining how long to wait after the 180° pulse for the spins to rephase, when the NMR signal can be observed (Figure 1.3

(a)). The operation of the spin echo sequence is as follows. First, the 90° pulse rotates the magnetization into the x-y plane (Figure 1.4). Because of inhomogeneity of the field, spins with different precession speeds will fan out. This is called dephasing. Applying a 180° pulse after a time interval τ causes all the spins to suddenly reverse phase, so the fast spins are then behind the slow spins. After the same time interval τ, the fast spins catch up with the slow spins and a spin "echo" can be detected. The intensity of the spin echo is clearly related to time interval between two pulses (Figure 1.3 (b)) according to the equation:

$$M(\tau)=M_0 e^{\frac{-2\tau}{T_2}} \qquad (1.20)$$

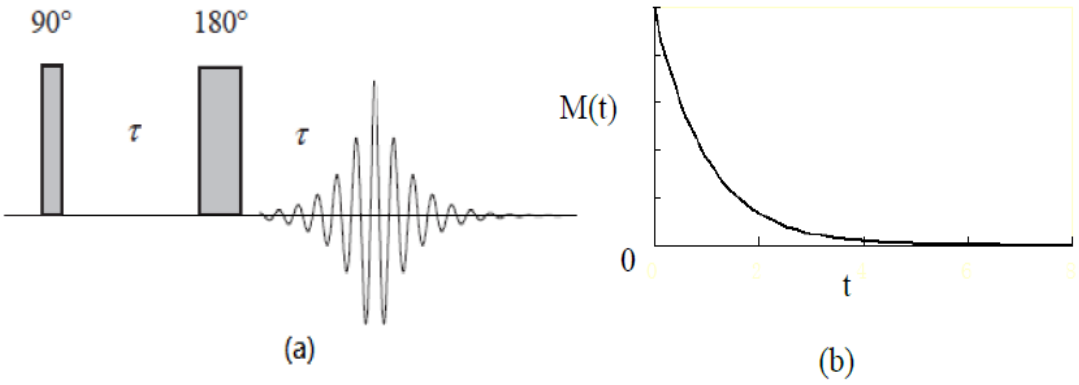

Figure 1.3 (a) Pulse sequence for spin echo; (b) the evolution of magnetization of spin echo

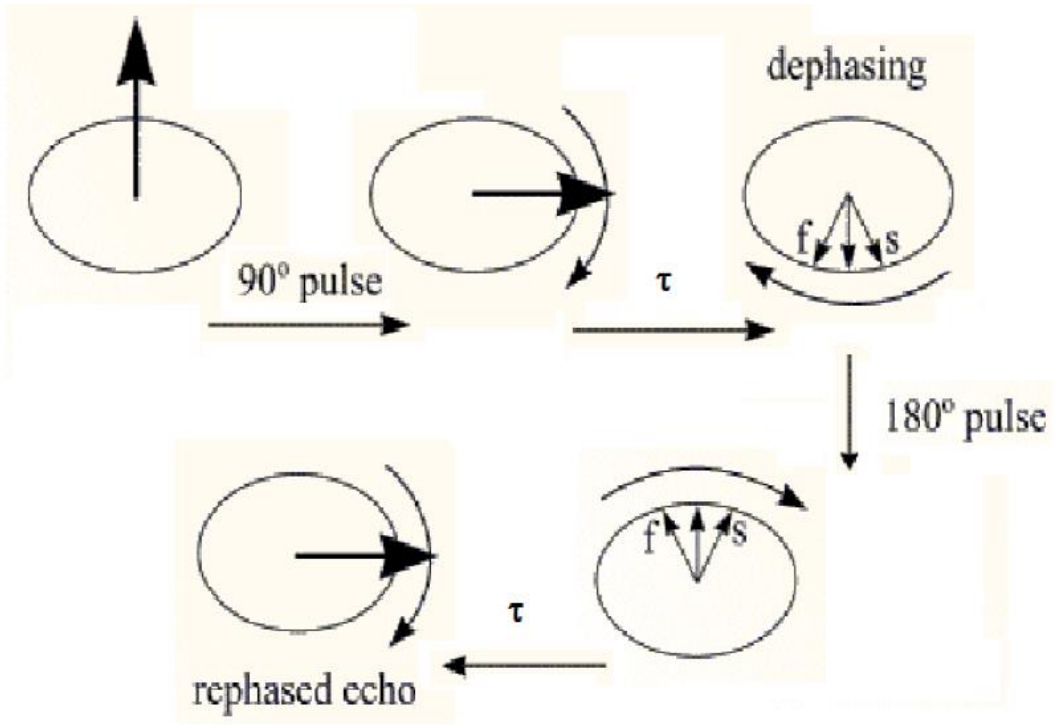

Figure 1.4 Buildup of a spin echo

Where M_0 is equilibrium initial magnetization along the large static magnetic field H_0. By varying the 90°-180° delay time τ and observing the intensity of the spin echo signal, the spin-spin relaxation time T_2 can be measured.

1.1.9 Solid State NMR

NMR spectra provide information about chemical shifts and the relative intensities of different species. The magnitude of the chemical shift is related to the extent to which the electron can shield the nucleus from the applied magnetic field. In a spherically symmetric molecule, the chemical shift is independent of molecular orientation. In an asymmetric molecule, the chemical shift is dependent on orientation and the magnetic field experienced by the nucleus varies as a function of the orientation of the molecule in the magnetic field. The NMR spectrum from a random distribution of fixed orientations

such as in a solid is broadened due to different resonance frequencies of the same species. The NMR spectrum from a non-viscous liquid has a narrow width limited only by the spin-lattice relaxation time and the magnetic field inhomogeneity since the fields at the various orientations of the nucleus average out due to the extremely rapid tumbling of the molecule.

In addition to anisotropic chemical shift, there is another reason for broad NMR lines in solids: dipolar coupling. Nuclear spins exhibit a dipole moment, which interacts with the dipole moments of other nuclei. The magnitude of the interaction is dependent on the spin species, the internuclear distance, and the orientation of the vector connecting the two nuclear spins with respect to the external magnetic field B. The maximum dipolar coupling is given by the dipolar coupling constant d:

$$\mathrm{d} = \frac{\hbar \mu_0 \gamma_1 \gamma_2}{4\pi r^3} \qquad (1.21)$$

where r is the distance between the nuclei, and γ_1 and γ_2 are the gyromagnetic ratios of the nuclei. In a strong magnetic field, the dipolar coupling depends on the orientation of the internuclear vector with the external magnetic field by:

$$D \propto 3\cos^2\theta - 1 \qquad (1.22)$$

Consequently, two nuclei with a dipolar coupling vector at an angle of θ_m=54.7° to a strong external magnetic field, which is the angle where D becomes zero, have zero dipolar coupling. θ_m is called the magic angle. One technique for removing dipolar couplings, to a considerable extent, is magic angle spinning (MAS) (Andrew 1981) (Figure 1.5). The MAS can reduce the broadening of line that comes from dipole-dipole

interaction, chemical shift anisotropy (CSA) and first order observed in the NMR spectrum (Figure 1.6 asterisk marked line). The spinning sidebands come from the time dependent term in those interactions listed above (Maricq and Waugh 1979). Peaks of the central resonance and each spinning sideband are separated in frequency by the spin rate, but the central line will stay stationary when the spin rate changes. So the central line can be distinguished from a sideband by varying the sample spin rate.

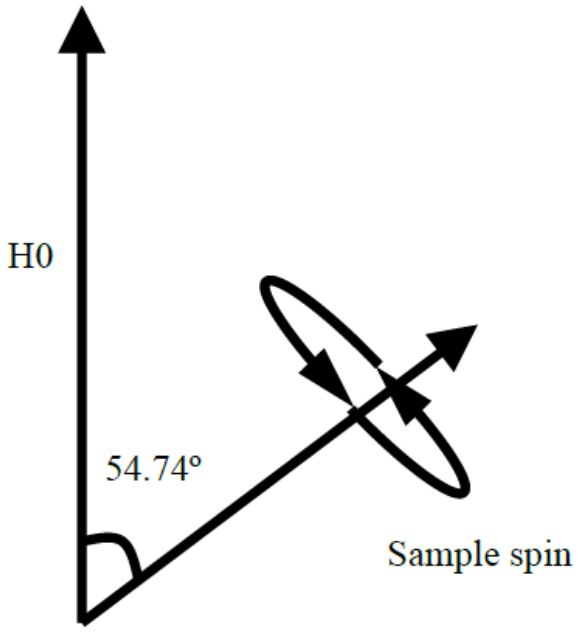

Figure 1.5 Magic Angle Spinning (MAS)

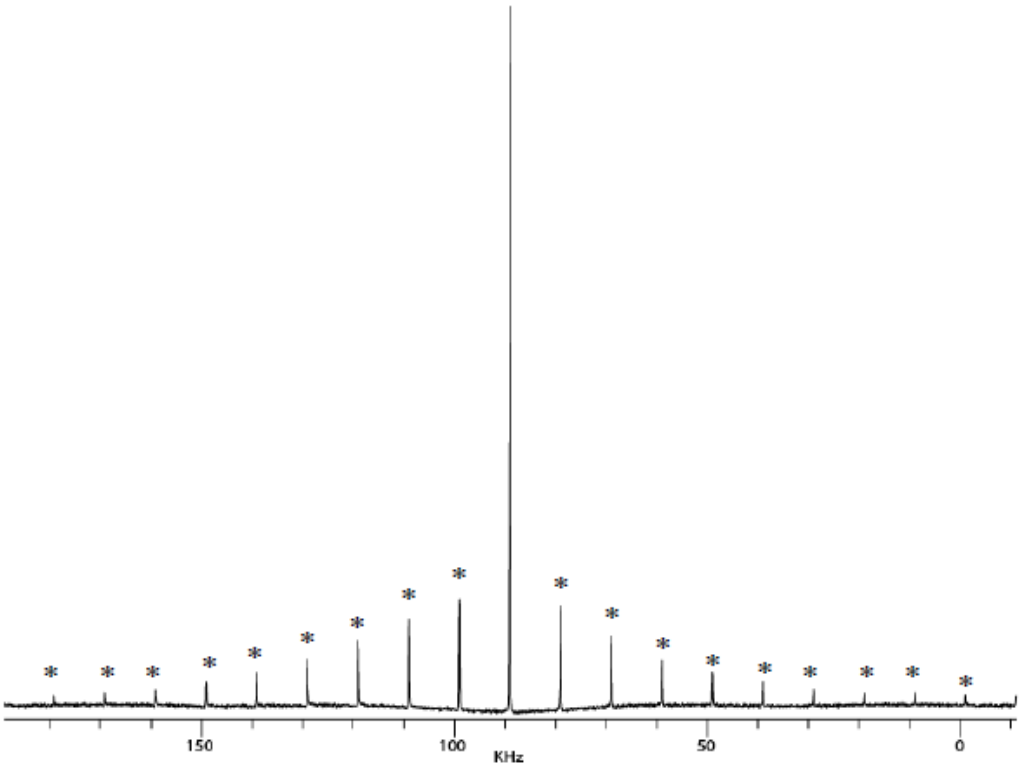

Figure 1.6 MAS NMR spectrum with spin sideband (with asterisk mark); spin rate 10KHz

1.1.10 Instruments

Most of the experiments in this thesis were conducted with a Varian CMX300 NMR spectrometer. The spectrometer is made of mainly four parts: magnet, probe, console and computer.

1.1.10.1 Magnet

The magnet is constructed with a superconducting coil composed of niobium alloy. The superconducting coil must be kept at a temperature under 10K to maintain the superconducting state. So liquid He is used to maintain the low temperature. To conserve the liquid He as long as possible, the container or liquid He is surrounded by liquid N_2.

From Stefan-Boltzmann Law, the radiation power into liquid He is proportional to T^4 where T is about 300K if there is no liquid N_2 surrounding the liquid He. With liquid N_2, the surrounding temperature will be lowered to about 75K, so the radiation power into liquid He is decreased hugely. With this setup, 60L liquid He will last 4-6 months. As shown in Figure 1.7, the NMR probe is lifted up into the magnet from the bottom. The heating gas flows in from the top via the tube inserted into the magnet's room-temperature bore (89mm diameter). A thermocouple placed in the bottom of stack that is used to monitor the temperature of sample. The Figure 1.8 is a photo of the magnet in our laboratory. The magnetic field is ~7 tesla. The NMR magnetic field strength is proportional to the proton NMR frequency, and thus the spectrometer is called a 300MHz NMR spectrometer.

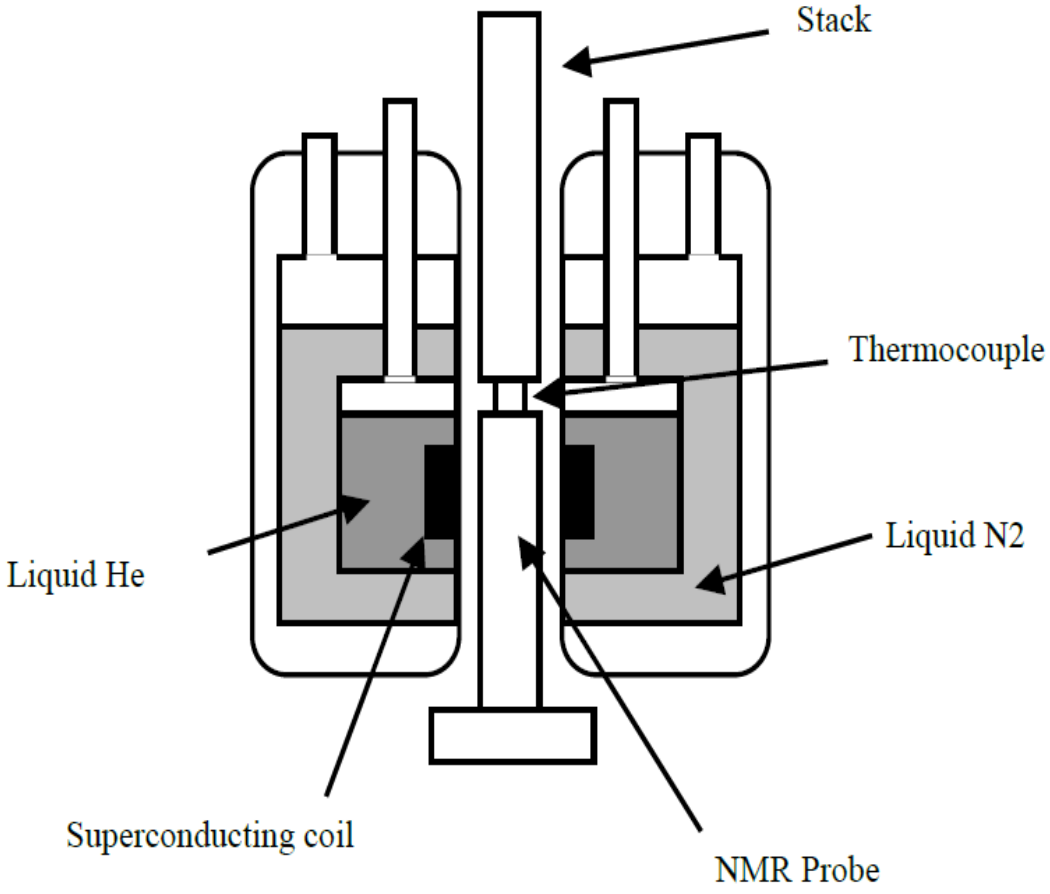

Figure 1.7 Sketch of magnet

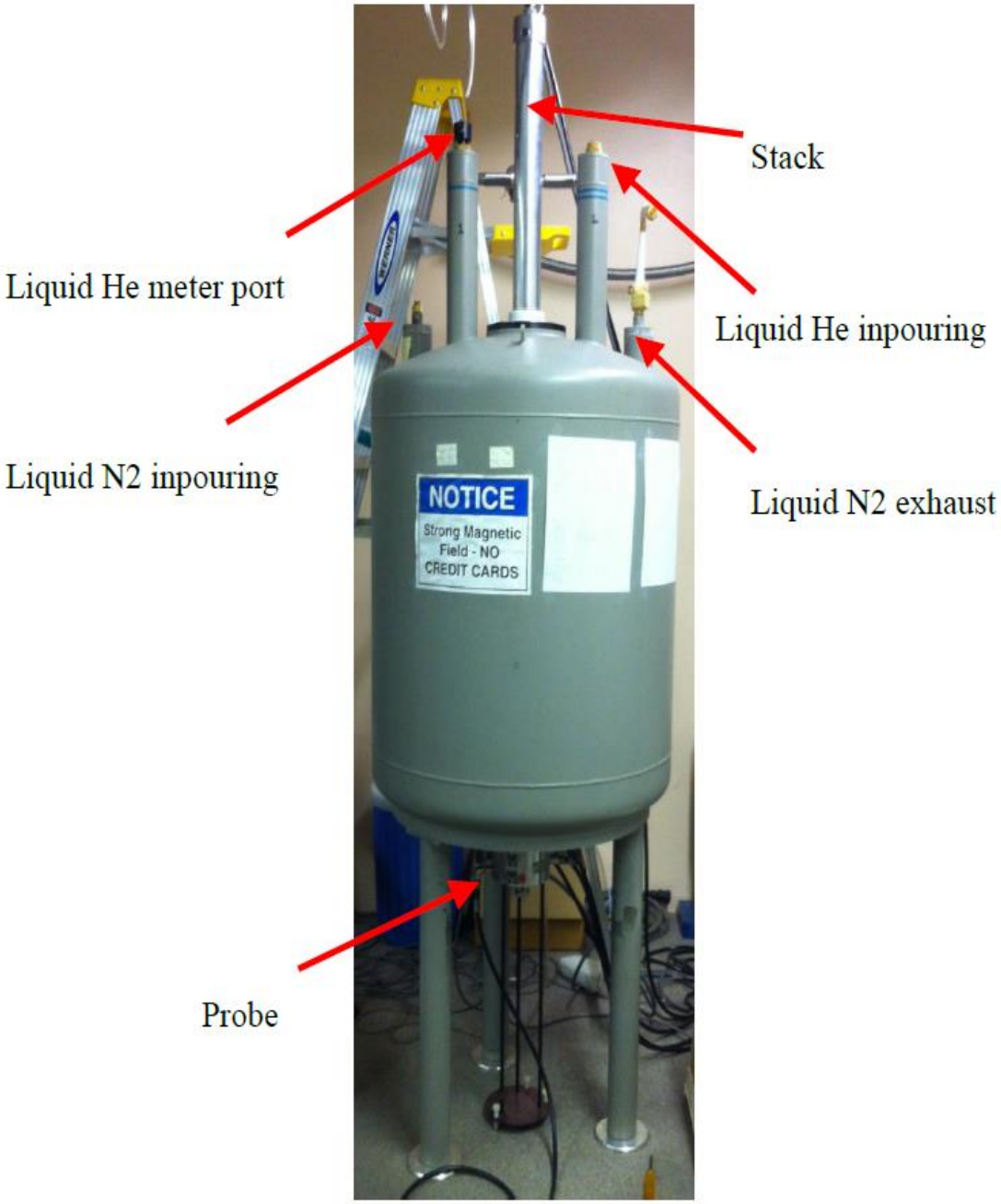

Figure 1.8 Photo of 7T magnet

1.1.10.2. NMR Probe

The element for basic signal acquisition of an NMR probe is an LC circuit (Figure 1.9), which is composed of two variable capacitors, one inductor and an r.f. coil. The r.f. coil (Figure 1.10 (left)) is used to apply radio frequency pulses. The coil alone would have a huge impedance at high frequency, so we use an LC circuit tuned to the resonance frequency of the observed nuclei and matched to the impedance of the whole circuit. The resonance frequency of the LC circuit can be adjusted using the total of the two variable capacitors, while the impedance match is achieved by careful adjustment of their ratio. The resonance frequency of the LC circuit must be adjusted to a value close to the NMR frequency at the beginning of measurement, every time.

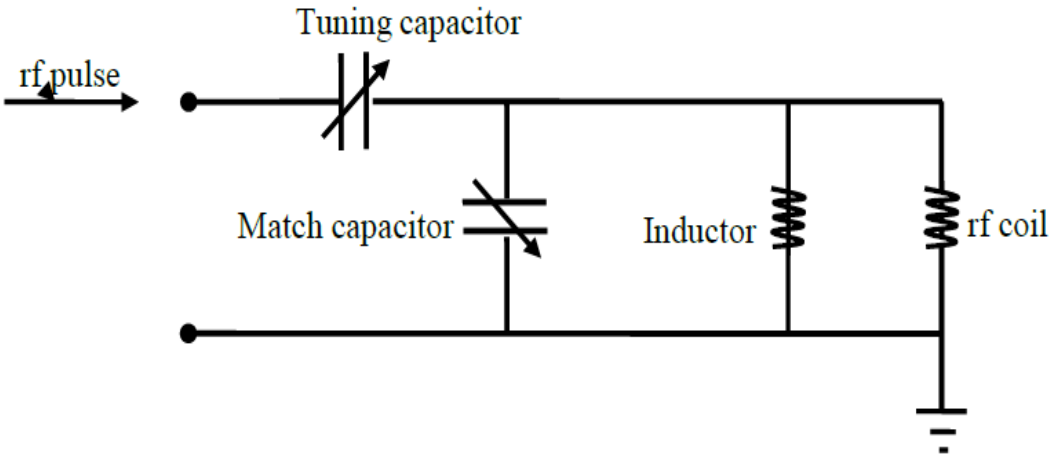

Figure 1.9 LC circuit of NMR probe

Two commonly used probes are a diffusion probe equalized with gradient coil and MAS probe. The former is mainly used for liquid samples and the latter for solid samples. The diffusion probe has a gradient coil (Figure 1.10 (right)) that can apply substantial magnetic field gradients, allowing diffusivity measurements. Two gradient coils (top and

down) have opposite directions of current, when magnetic field gradient is applied. So the magnetic field due to the coils is zero,

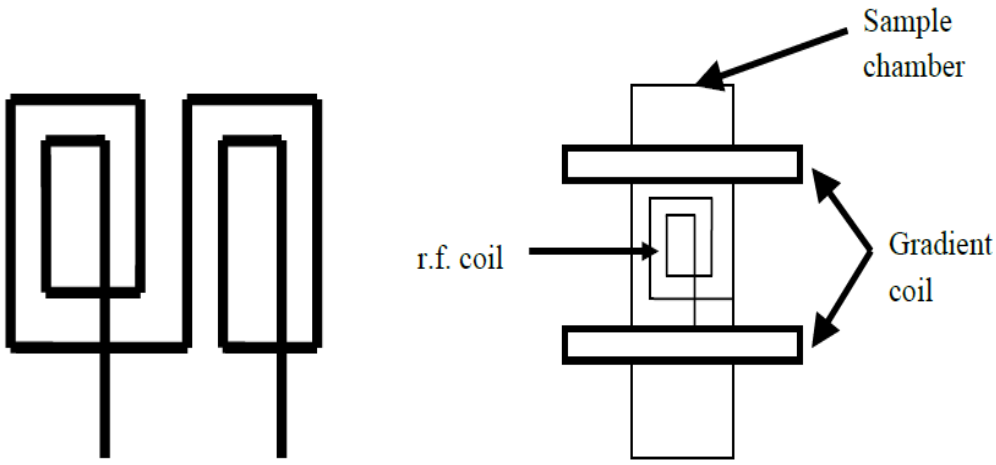

Figure 1.10 r.f. coil (left) and gradient coil (right) of diffusion probe

but the gradient can be varied by control of the driving current. An MAS probe has a stator (Figure 1.11), which is used for magic angle spinning of a sample in tubular-shaped rotor. The main axis of stator is adjusted to an angle of 54.74° with the ambient magnetic

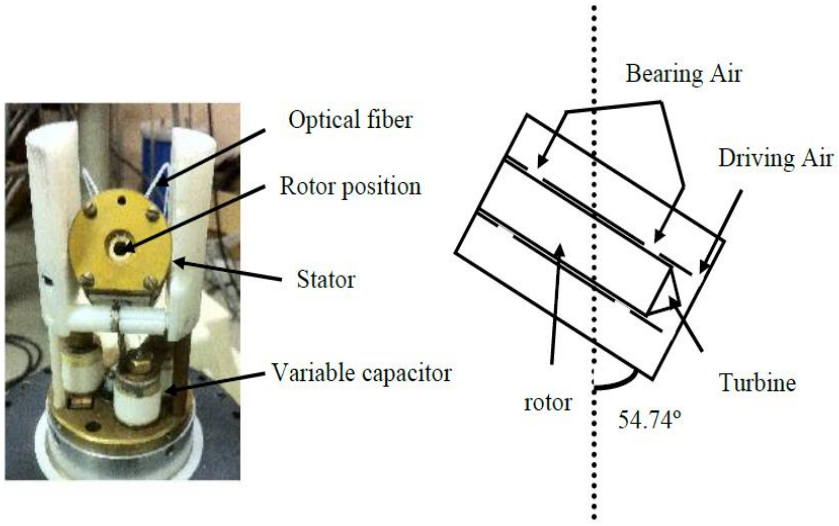

Figure 1.11 Stator of MAS NMR probe

field. A solid sample is packed in the rotor and set inside of the stator. Two air flows are applied: bearing and driving at pressure to 40psi. The former flows around the rotor, therefore stabilizing the rotor and eliminating the friction between rotor and stator; the latter flows in a specific direction and drive the rotor's turbine, producing the spin. The optical fibers and diode laser are used to monitor the spin rate, via optical detection of the light reflected from alternating light and dark sections of the illuminated rotor as it spins. The spin rate can reach as high as 12 KHz.

1.1.10.3. Console

The console is composed of several electronic modules (Figure 1.12). Part A is used to apply gradient magnetic fields. Part B is used to generate radio frequencies. Part C is a single board computer (SBC) that is controlled by the spectrometer's Sun Blade work station, and thereby controls all other electronic devices. Part D is the receiver, used to receive induction signal of FID from preamplifier and deliver signals to the SBC. Part E is the transmitter, used to produce low power r.f. pulses. Part F is a two stage high frequency (H-power) amplifier, used to amplify r.f. power output at frequencies higher than 180MHz (for proton and fluorine nuclei). Part G is a low frequency power amplifier, used to amplify r.f. output at frequencies lower than 180MHz. Part H is the shim control, which is used to shim the ambient magnetic field, making it homogeneous to +/-0.1ppm. The computer is used to set all the parameters for NMR measurement and process the signal to get the NMR spectrum.

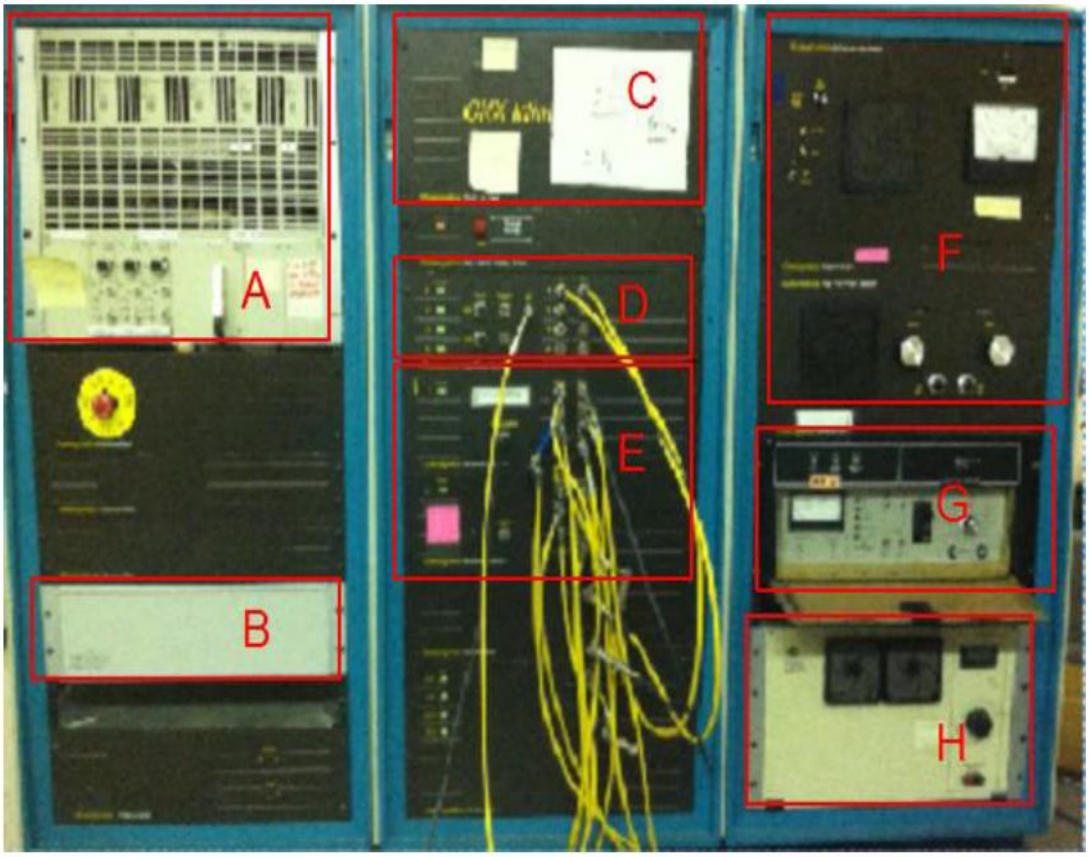

Figure 1.12 Console of NMR spectrometer

1.2 Diffusion

Diffusion is the net movement of a substance composed of atoms, ions or molecules from a region of high concentration to a region of low concentration, without bulk motion. Diffusion is also referred to as the movement of a substance down a concentration gradient – the change in the value of a quantity (e.g. concentration) with the change in another variable (e.g. distance). There are two ways to describe the notion of diffusion: either a phenomenological approach starting with Fick's laws of diffusion and their

mathematical consequences, or a physical and atomistic one, by considering the random walk of the diffusing particles.

1.2.1 Fick's laws of diffusion

Fick's first law relates the diffusive flux to the concentration under the assumption of steady state. It postulates that the diffusive flux goes from regions of high concentration to regions of low concentration, with a magnitude that is proportional to the concentration gradient. In one (spatial) dimension, the law is:

$$J = -D\frac{\partial \phi}{\partial x} \tag{1.23}$$

Here J is the diffusion flux – amount of substance diffusing past unit area per unit time, D is the diffusion coefficient or diffusivity, ϕ is the concentration of substance, and x is the position in length. In two or more dimensions, Fick's first law becomes,

$$\boldsymbol{J} = -D\boldsymbol{\nabla}\phi \tag{1.24}$$

where $\boldsymbol{\nabla}$ is the del or gradient operator and **J** is the diffusion flux vector. Fick's second law (the diffusion equation) predicts how diffusion causes the concentration to change with time. We get this by substituting the first law (equation 1.23) into the equation of continuity,

$$\frac{\partial J}{\partial x} + \frac{\boldsymbol{\partial \phi}}{\boldsymbol{\partial t}} = 0 \tag{1.25}$$

It leads directly to a partial differential equation which in one dimension reads:

$$\frac{\partial \phi}{\partial t} = D\frac{\partial^2 \phi}{\partial x^2} \tag{1.26}$$

Here ϕ is the concentration that depends on location x and time t and D is the diffusion coefficient. In two or more dimensions, Fick's second law becomes,

$$\frac{\partial \phi}{\partial t} = D\Delta\phi \qquad (1.27)$$

where $\Delta = \nabla^2$ is the Laplacian.

1.2.2 Random Walk

A random walk is a random process consisting of a succession of discrete steps of fixed average length. Random walks can be on a graph, on a line, in a plane, in higher dimensions, or even on a curved surface (Wikipedia, 2015). The collisions of molecules in a gas are a random walk responsible for diffusion, which obeys eq. 1.27 above. For N number of random steps in one dimension, the mean square distance covered is $\sqrt{N}$. In a random walk of a large number of independent steps, also known as the Wiener process, the distance covered in time t in three dimensions is given by

$$\sigma^2 = 6Dt \qquad (1.28)$$

where σ is the standard deviation of the distance covered, D is the diffusion constant, and t is the time. Random walk has applications in physics, chemistry and many other fields.

References

Andrew, E. R. 1981. MAGIC ANGLE SPINNING IN SOLID-STATE NMR-SPECTROSCOPY. *Philosophical Transactions of the Royal Society a- Mathematical Physical and Engineering Sciences* 299 (1452):505-520.

Hahn, E. L. 1950. SPIN ECHOES. *Physical Review* 77 (5):746-746.

Maricq, M. M., and J. S. Waugh. 1979. NMR IN ROTATING SOLIDS. *Journal of Chemical Physics* 70 (7):3300-3316.

Random walk. (2015, November 18). In *Wikipedia, The Free Encyclopedia*. Retrieved 23:30, November 18, 2015, from https://en.wikipedia.org/w/index.php?title=Random_walk&oldid=691248156

CHAPTER 2

IONIC LIQUIDS AND FUEL CELLS

2.1 Ionic Liquids

2.1.1 Definition, History, and Properties

Ionic liquids, formerly known as molten salts, are salts that usually exist in liquid phase well below room temperature up to a temperature as high as 200°C. In these media a variety of organic and inorganic solutes dissolve partially or completely into separated anions and cations. In addition to being outstandingly good solvents, their extremely low vapor pressure makes them desirable "green" substitutes for traditional industrial solvents, in particular volatile organic compounds, a major source of industrial pollutants (Wasserscheid & Welton, 2003).

The first room temperature ionic liquid, ethylammonium nitrate (m.p. 12°C) was synthesized by Paul Walden who published his work in 1914 (Walden, 1914). In 1951, Hurley first demonstrated aluminum deposition deposition using low melting salt (Hurley 1951). In the 1970's and 1980's ionic liquids based on alkyl-substituted imidazolium and pyridinium cations, with halide or tetrahalogenoaluminate anions, were initially developed for use as electrolytes in battery applications (Chum. *et al*., 1975). Recently, ionic liquids have found applications in fields such as cellulose processing, electrodeposition, solar and thermal energy systems, batteries and waste recycling, etc. (Rogers and Seddon, 2002).

Ionic liquids have many advantageous properties over aqueous based systems. Some of these properties include large temperature extreme range (0°C - 200°C), excellent

solvating properties, high viscosity, low volatility, high ionic conductivities, designability, etc.

An attractive feature of ionic liquids is that they are “designable” (Ohno, 2005) meaning that they can be synthesized with many variations allowing them to be finely tuned for specific applications. There are mainly two classes of ionic liquids: aprotic and protic ionic liquids. There can be many subclasses among these two classes, such as organic vs. inorganic, high vs. low temperature, etc.

2.1.2 Protic Ionic Liquids

Protic ionic liquids are a class of ionic liquids with interesting properties and applications (Greaves & Drummond, 2008). They are produced through the combination of a Brønsted acid (proton donor) and a Brønsted base (proton acceptor) according to the following reaction:

$$HA+B \rightleftharpoons HB^{+}+A^{-} \qquad (2.1)$$

The relative strengths of acid to base in large parts determines the “iconicity” ot the extent to which the species exists in the ionic form vs the molecular form. Ionicity is the extent to which reaction 2.1 has gone to completion. The difference in energy levels of protons from acid to base is called the proton free energy gap. Typical values of the proton free energy gap in protic ionic liquids are on the order of 0.7 – 1.0 ev.

The key property that distinguishes protic ionic liquids from other ionic liquids is proton transfer from acid to base. This leads to the presence of proton-donor and proton-acceptor sites, which can be used to build up a hydrogen-bonded network. The proton-transfer process has been found to improve when the energy change after the proton transferred

from the acid to the base is around 0.8 eV (Belieres *et all*, 2006). Due to their protonic conductivity, protic ionic liquids are being investigated as proton conducting media used for proton exchange membrane (PEM) fuel cells (Belieres *et all*, 2006).

2.1.3 Walden Plot

In order to vaporize an ionic liquid it is necessary to do work against the electrical forces that hold and ion pair in liquid phase. If the ionic liquid consisted only of ion pairs, this work would be equivalent to vaporizing a strongly dipolar liquid. In practice it is found that the work required to vaporize an ionic liquid is much higher than for dipolar liquids. the energy for stabilization in an ionic liquid is gained through the formation of long range pairings between ions of different charges as in the formation of a crystal lattice. This additional energy for stabilization in ionic crystals over dipolar crystals is called the Madelung energy.

The relation between low vapor pressure and electrical conductivity is expressed by three of the classical equations of electrochemistry. These equations are derived for dilute aqueous solutions where it is assumed that all ions move independently. These equations are:

1. The Nernst-Einstein equation,

$$\lambda_i = \frac{RTz_iD_i}{F^2} \qquad (2.2)$$

where λ_i is the partial equivalent ionic conductivity, R the ideal gas constant, T the temperature, z_i is the ionic charge, D_i the diffusivity of ionic species i, and F the Faraday constant.

2. The Stokes-Einstein equation

$$D_i = \frac{k_B T}{6\pi\eta r_i} \quad (2.3)$$

where D_i is the diffusivity of ionic species i, η is the viscosity of the liquid, and r_i is the ionic radius. This equation is for the diffusion of spherical particles.

3. The Walden rule

$$\Lambda\eta = constant \quad (2.4)$$

where Λ is the equivalent molar conductivity of the liquid, and η is the viscosity.

Equation 2.4 allows us to devise a classification system for evaluating the ionic and conductive properties of ionic liquids and other electrolytes. The Stokes-Einstein equation applies well to nonviscous liquids and the Walden rule applies well to pure ionic liquids. The graphical representation of the Walden rule, or a Walden plot is shown in Figure 2.1 where the log of the inverse of the viscosity or the fluidity is plotted along the x-axis and the log of the equivalent conductivity is plotted along the y-axix.

On the Walden plot, an "ideal" line is constructed by using data for dilute aqueous KCl solutions in which the system is known to be fully dissociated and the ions to have equal mobility. Ionic liquids are classified into ideal or good ionic liquids, subionic or poor ionic liquids, and superionic liquids. Ionic liquids that fall on the upper side of the ideal line are desired because transport within them occurs faster than diffusion alone as predicted by the Stokes-Einstein equation. The transport of protons through a medium faster than diffusion alone by protons "hopping" from one vacancy to another is called

Grotthus mechanism. These superionic liquids include solutions of strong acids in water or other solvents with extensive hydrogen bonding. There is a strong desire to move away from water based electrolytes for proton transport as they create several challenges fuel cell design and operation. It is hoped that a super ionic protic ionic liquid or glass can be found so that an all-solid fuel cell can be realized (Ohno 2005).

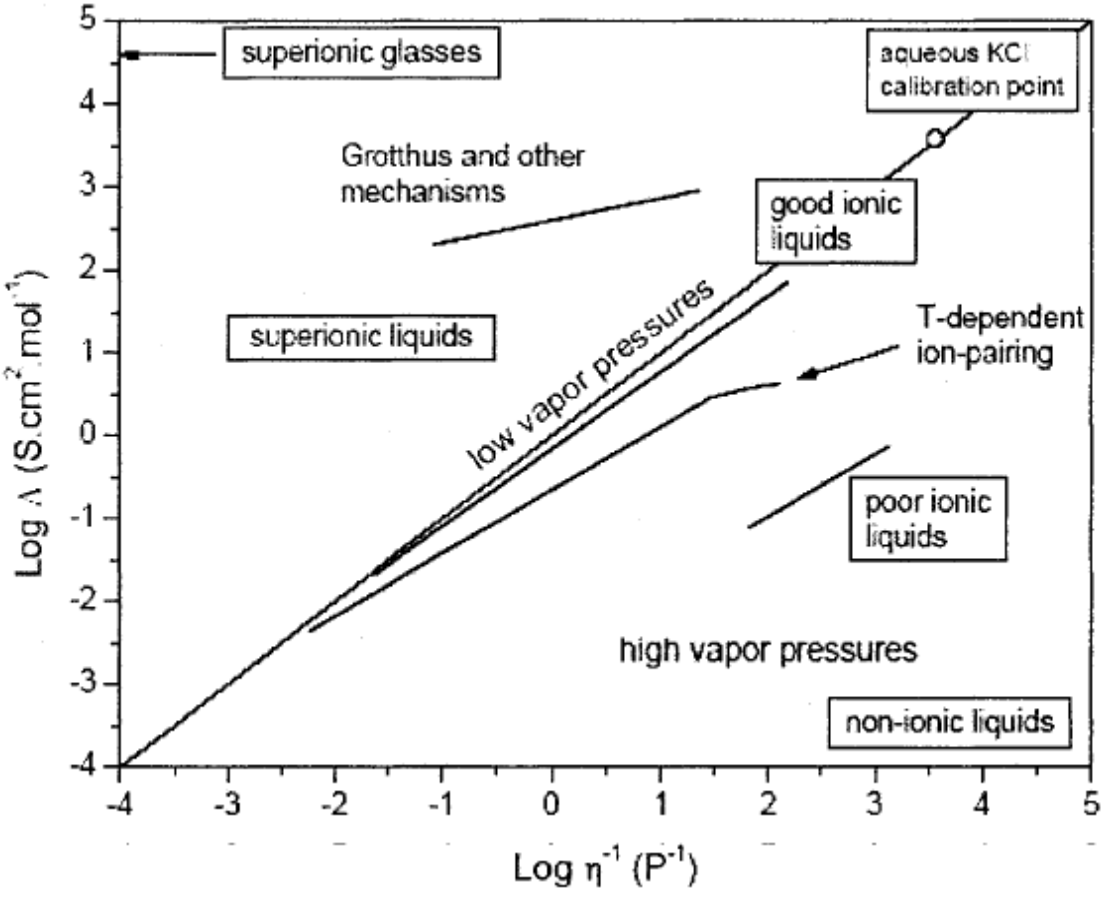

Figure 2.1 Walden plot showing relationship between the equivalent conductivity and the fluidity of ionic liquids (J.-P. Belieres 2005)

The high cohesive forces present in ionic liquids due to the electrostatic attractions between ions makes them more viscous than other liquids. The smaller the ions are, the higher the cohesive forces.. Since high cohesion means high viscosity, good ionic liquids need to achieve an optimum lowering cohesion if they are to serve as high-fluidity and high-conductivity media at low temperatures. It is tempting to reason that increasing the size of the ions would be the way to achieve high fluidities. However, the van der Waals interaction forces become stronger as the particle size increases. It is required to keep these forces at a minimum by maintaining an unpolarizable outer surface on the anions. For this reason, perfluorinated species are used in ionic liquid preparation.

2.2. Fuel Cells

2.2.1 History

The first demonstration of a hydrogen fuel cell was made in England over 160 years ago in 1838 by lawyer and scientist Sir William Grove (Grove, 1839). The basis for his experiment was if it was possible to split water into hydrogen and oxygen at separate electrodes, the reverse process, to generate electricity and water from the consumption of hydrogen and oxygen at separate electrodes, should also be possible. To test this theory, Grove arranged two platinum electrodes with the bottom of each immersed in sulfuric acid, with the top of one sealed in a tube of hydrogen and the top of the other in oxygen. He observed that a constant current flowed between the two electrodes, and that water was formed (Grove, 1842). To increase the voltage, Grove

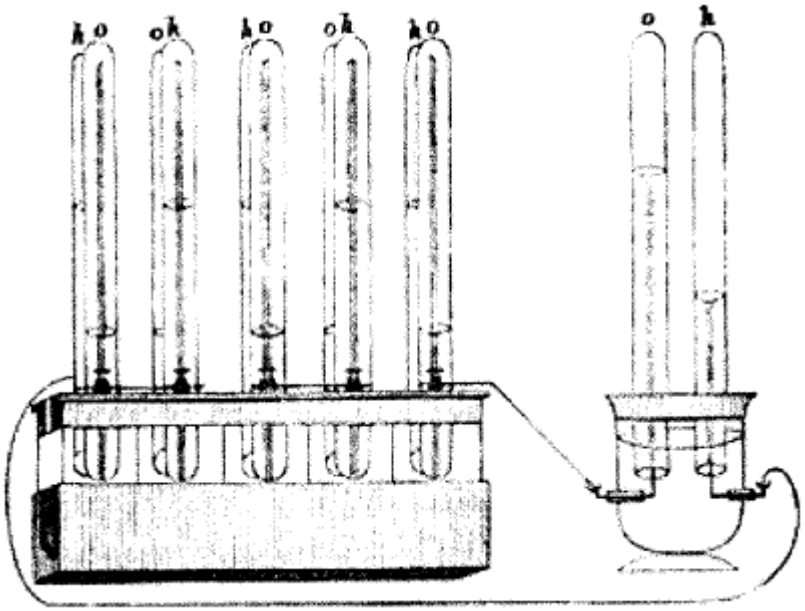

Figure 2.2 Sir Willam Grove's drawing of his experimental "gas battery" from an 1843 letter (Image from Proceedings of the Royal Society).

arranged several cells in series, as shown in Figure 2.2, and created what he referred to as a "gas battery" (Grove, 1843).

In June 1839, German physicist Christian Friedrich Schonbein discussed in a letter the first crude fuel cell that he had invented. His letter discussed current generated from hydrogen and oxygen dissolved in water. The term "fuel cell" was first used by the chemist Ludwig Mond and his assistant Carl Langer who attempted to use air and industrial coal gas to generate electricity (Mond & Langer, 1889). The next most important step in the fuel cell's development was made in 1932 by Dr. Francis Thomas Bacon, an engineer at Cambridge University. Bacon reconstructed the apparatus developed by Mond and Langer and made a number of modifications to the original design, which included replacing the sulphuric acid electrolyte by potassium hydroxide

(KOH). Named the "Bacon Cell", after the inventor, it was in essence the first alkaline fuel cell. In 1959, Bacon was able to produce a practical fuel cell, capable of generating 5 kW of power (Bacon, 1969).

In the late 1950's and early 1960's, there was renewed interest in fuel cells. NASA was looking for a way to power a series of upcoming manned space flights requiring a longer duration power source. Using batteries was ruled out due to weight considerations. NASA's search for an alternative led to the fuel cell as a possible solution. This led to the development of the first Proton Exchange Membrane Fuel Cell in 1955 by General Electric (GE). As the electrolyte GE used a sulphonated polystyrene ion-exchange membrane (Hoogers, 2003). In the early 1960's, the aircraft engine manufacturer Pratt & Whitney licensed the Bacon patents for the Alkaline Fuel Cell with the goal of reducing the weight and designing a longer-lasting fuel cell than the GE Proton Exchange Membrane design. Alkaline fuel cells have since been used on most subsequent manned U.S. space missions, including those of the Space Shuttles.

Over the past few years, concerns over depleting stocks of natural resources and a growing awareness of the environmental damage caused by widespread burning of fossil fuels helped to drive the interest in the commercial development of fuel cells. Utility companies have started testing and installing fuel cells in hospitals and schools. Most of the major automotive manufacturers, following the work of the Canadian company Ballard in 1993, have unveiled prototypes of fuel cell-powered cars (Cropper *et al*, 2004).

2.2.2 General Principles

A fuel cell is a device that converts the chemical energy from a fuel into electricity through a chemical reaction of positively charged hydrogen ions with oxygen or another oxidizing agent. Fuel cells are different from batteries in that they require a continuous source of fuel and oxygen or air to sustain the chemical reaction, whereas in a battery the chemicals present in the battery the chemicals present in the battery react with each other to generate an electromotive force (emf). Fuel cells can produce electricity continuously as long as there inputs are supplied.

Instead of combusting the fuel and oxidant directly to form the resultant products and provide heat to do mechanical work, as in a Carnot engine, a fuel cell produces electrical energy by another means, namely by the release of the free chemical energy of the reactants in oxidation and reduction reactions. Each separate reactant makes a product at its electrode and these products subsequently combine to form the resulting product which is equivalent to the product of direct combustion through the Carnot path. The anodic, cathodic and overall reactions in a hydrogen fuel cell are:

Anode: $2H_2 \rightarrow 4H^+ + 4e^-$

Cathode: $O_2 + H^+ + 4e^- \rightarrow 2H_2O$

Overall reaction: $O_2 + H_2 \rightarrow 2H_2O$

A shematic representation of a H_2/O_2 fuel cell is shown in Figure 2.3.

The relationship between the theoretical maximum energy from combustion and electrochemical reactions using identical reactants is:

$$\Delta G^\circ = -RT\ln K_{eq} = -nFE^\circ \quad (2.5)$$

Where,

ΔG°: standard Gibbs free energy available from combustion

R: ideal gas constant (8.314 J/mol·K)

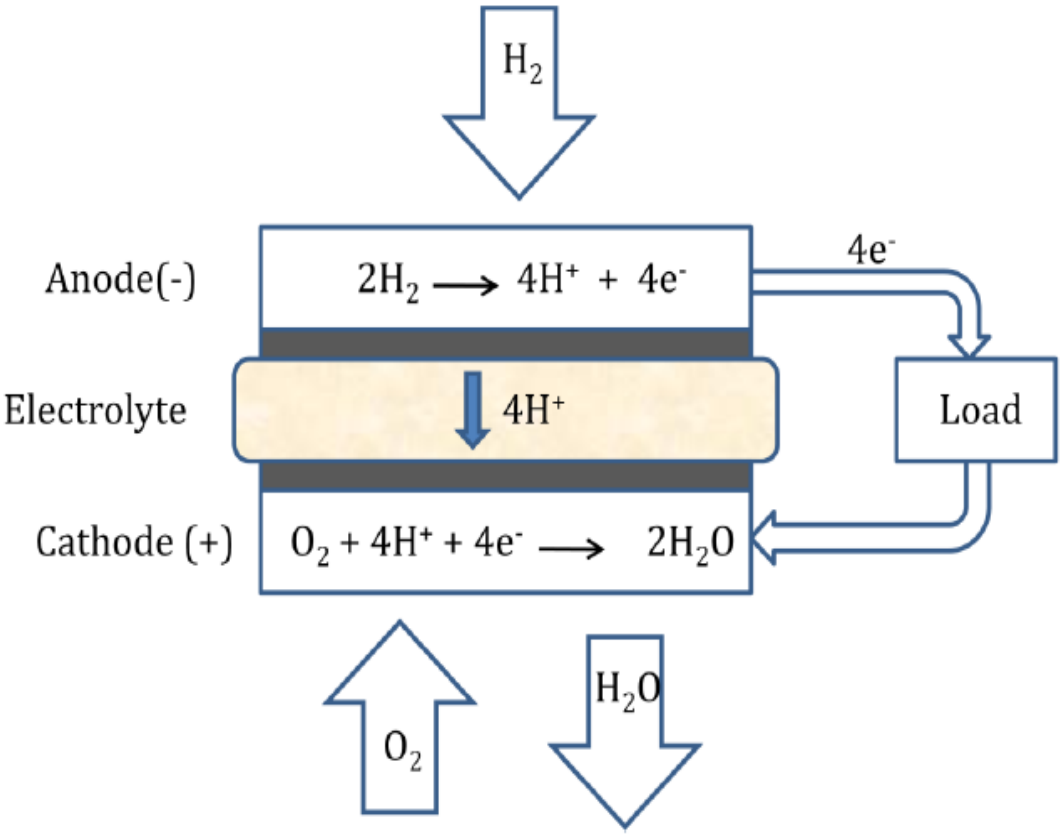

Figure 2.3 Schematic representation of an acid electrolyte hydrogen/oxygen fuel cell.

T: absolute temperature (K)

Keq: equilibrium constant

n: number of electrons transferred, here n=2

F: charge carried by a mole of electrons, Faraday's constant (96485 C/mol)

E°: reversible equilibrium potential (electromotive force or cell voltage)

In a heat engine operating under ideal conditions according to the theoretical thermodynamics of the Carnot Cycle it is impossible to convert all heat energy into mechanical energy. As a necessity some of the heat energy is rejected. For example, in an internal combustion engine, fuel is combusted producing heat energy at a high temperature T_h, part of which is converted into mechanical energy by doing work on a piston. Ultimately part of the heat energy is rejected into a heat sink at a lower temperature, T_c. The efficiency of the engine depends on the difference between T_h and T_c.

$$\text{Maximum efficiency, Carnot engine} = \frac{T_h - T_c}{T_h} \qquad (2.6)$$

Constrained by the limits placed on operating temperature extremes, combustion engines seldom exceed 30% operating efficiency. Fuel cells are not subject to the Carnot efficiency limit. They directly convert chemical energy into electrical energy as governed by the chemical kinetics of the system. The efficiency of electrochemical devices is defined as:

$$\text{efficiency} = \frac{\text{electrical energy produced}}{\text{Gibbs free energy change}} \qquad (2.7)$$

Another way to compare efficiencies of an electrochemical redox reaction and the corresponding combustion reaction is to compare the electrical energy produced to the heat produced by combusting the fuel. The efficiency of a fuel cell can be defined as the ratio of the electrical energy produced over the change in enthalpy ΔH of the reaction. The thermodynamic efficiency of a fuel cell is:

$$\eta_{\text{therm}} = \frac{-\Delta G}{-\Delta H} \qquad (2.8)$$

The efficiency gain from using fuels in redox reactions can be up to three times higher than by combusting them in a Carnot cycle. A fuel cell is therefore a much cleaner, more efficient way to convert chemical energy into a electrical energy. A fuel cell differs from a battery in that it can operate continuously as long as the reactant flows to the anode and the cathode are maintained.

If fuel cells are to become long-lived, lightweight alternatives to conventional batteries, a number of challenges need to be addressed. Among these challenges are lowering their high cost, increasing the slow electrode kinetics at the cathode, and avoiding the parasitic energy losses from running humidifiers for the electrolyte membrane and excessive air blowers. Current Proton Exchange Membrane (PEM) fuel cells require a substantial amount of platinum catalyst to function properly. In 1990, fuel cells required approximately 12 grams of platinum per kilowatt of power generated. By 2000 this number had dropped to less than 0.5 grams per kilowatt (Fitzgerald 2001). Currently, research is under way to decrease this amount further or eliminate the need for platinum altogether.

2.2.3 Different types of fuel cells

Fuel cells are classified by electrolyte, operating temperature, and the nature of fuels and oxidants used.

2.2.3.1 Alkaline Fuel Cell (AFC)

AFC, also known as the Bacon fuel cell, is one of the most developed technologies operating on pure H_2 and O_2. AFCs have been used since the mid-1960's by NASA in the Apollo and Space Shuttle programs. AFC's consume hydrogen and pure oxygen producing potable water, heat, and electricity. The electrolyte is an aqueous solution of potassium hydroxide (KOH). It operates between 60°C and 260°C. High temperature AFCs use a concentrated (85Wt.%) solution while low temperature AFCs use a more dilute solution (35-50Wt.%). The charge carrier in this type of fuel cell is the hydroxyl ion (OH-). The electrolyte is soaked into a porous matrix (usually asbestos). A characteristic of AFCs is that they are very sensitive to carbon dioxide (CO_2) that decomposes the alkaline electrolyte through the process:

$$2KOH + CO_2 \rightarrow K_2CO_3 + H_2O \qquad (2.9)$$

Even the small amount of CO_2 in air must be removed before being fed to an AFC. To limit effects of CO_2, the KOH solution is pumped around the fuel cell for regeneration of the electrolyte. This can also serve as a cooling system for the fuel cell (McLean *et al.*, 2002).

AFCs are one of the cheapest fuel cells to manufacture. This is partly because a wide range of electrocatalysts required for the electrodes can be used (Ni, Ag, metal oxides, noble metals), and some of these materials are relatively inexpensive compared to the catalysts required for other types of fuel cells. AFCs are not being considered for automobile applications since they are sensitive to poisoning, and require use of pure or cleansed hydrogen and oxygen, which is impractical. Conversely, AFCs operate at

relatively low temperatures which enable a quick starting power source, and are among the most efficient fuel cells.

2.2.3.2 Phosphoric Acid Fuel Cell (PAFC)

PAFCs were the first fuel cells to be commercialized (Penner *et al.,* 1995). Developed in the mid-1960's and field-tested since the 1970's, they have improved significantly in stability, performance, and cost. Such characteristics have made the PAFC a good candidate for early stationary applications. The electrolyte is highly concentrated or pure liquid phosphoric acid (H3PO4) saturated in a silicon carbide matrix (SiC). The ionic conductivity of phosphoric acid is low at low temperatures, so PAFCs are operated between 150°C and 210°C. The charge carrier in this type of fuel cell is the proton (H^+). In generating electricity, PAFC systems operate at efficiencies up to 70% with most loss at the cathode. Furthermore, at the operating temperature of PAFCs, the waste heat is capable of heating hot water or generating steam at atmospheric pressure. When operating in cogeneration applications, the overall efficiency is approximately 80 to 85% (Ishizawa *et al,* 2000). The high efficiency of the PAFC in cogeneration mode is one advantage of this fuel cell. In addition, CO does not affect the electrolyte or the cell performance at these temperatures and PAFCs can therefore be easily operated with reformed fossil fuel. Simple construction, low electrolyte volatility and long-term stability are additional advantages. Disadvantages include rather low power density and aggressive electrolyte.

2.2.3.3 Proton Exchange Membrane Fuel Cell (PEMFC)

PEMFCs, also known as polymer electrolyte membrane fuel cells, are being developed for transport applications as well as stationary fuel cell applications and portable fuel cell applications. PEM fuel cells were used in the NASA Gemini series of spacecraft, but they were replaced by Alkaline fuel cells in the Apollo program and the Space shuttle. The fuel for PEMFCs is hydrogen and the charge carrier is the proton (H^+). PEMFCs use a solid electrolyte polymer that allows protons to be transmitted from the anode to the cathode. The standard in PEMFC today is the hydrated perffuorsulfonic acid polymer membrane Nafion® made by DuPont. This polymer is a proton conductor when saturated with water, but does not conduct electrons. PEMFCs generate more power for a given volume or weight compared to other fuel cells. The high-power density makes PEMFCs a potential basis for compact and lightweight power source. The operating temperature is less than 100°C, which allows rapid start-up. These aspects, and the ability to rapidly change power output, are some of the characteristics that make the PEMFC the top candidate for automotive power applications (Vielstich *et al.*, 2003).

There are other advantages from the electrolyte being a solid material, compared to a liquid. The sealing of the anode and cathode gases is simpler, and therefore, less expensive to manufacture. The solid electrolyte is also more immune to ionic shorting of cells in a stack as well as to difficulties with orientation and problems with corrosion, compared to many of the other electrolytes, thus leading to a longer cell and stack life.

One of the disadvantages of the PEMFC for some applications is that the operating temperature is near 100°C which is not high enough to perform useful cogeneration.

Also, since the electrolyte is required to be saturated with water to operate optimally, careful control of the moisture of the anode and cathode streams is important.

Because the operating temperature is limited to usually less than 120°C (Appleby & Yeager, 1986), and because of problems with water balance, a H_2-rich gas with minimal or no CO must be used.

2.2.3.4 Direct Methanol Fuel Cell (DMFC)

DMFC's are a subcategory of PEMFC in which methanol is used as the fuel. The technology behind DMFCs is still in the early stages of development, but it has successfully demonstrated powering mobile phones and laptop computers (Arico *et al.*, 2001). Similar to PEMFC, the electrolyte in DMFC is a polymer and the charge carrier is the proton H^+. However, the liquid methanol (CH_3OH) is oxidized in the presence of water at the anode generating CO_2, protons (H^+) and electrons that travel through the external circuit as the electric output of the fuel cell.

$$CH_3OH + \frac{3}{2} O_2 \rightarrow 2H_2O + CO_2 \qquad (2.10)$$

DMFC's were initially developed in the early 1990's, but were not embraced because of their low efficiency and low power density, as well as other problems. Improvements in catalysts and other recent developments have increased power density 20 -fold and the efficiency may eventually reach 40% (Dillon *et al.*, 2004). The operating temperature ranges from about 50°C to 120°C. This low operating temperature and no requirement for a fuel reformer make the DMFC an excellent candidate for very small to mid-sized

applications, such as cellular phones and other consumer products, up to powering automobiles.

The low-temperature oxidation of methanol to protons and carbon dioxide in DMFC requires a more active catalyst (Schultz *et al.,* 2001), which typically means that a larger quantity of expensive platinum catalyst is required than in conventional PEMFCs. This increased cost is more than outweighed by the convenience of using a liquid fuel and the ability to function without a reforming unit. Another concern driving the development of alcohol-based fuel cells is the fact that methanol is very toxic (Barceloux *et al.,* 2002). Therefore, some companies have started developing a Direct Ethanol Fuel Cell (DEFC). The performance of the DEFC is currently about 50% that of the DMFC, but this gap is expected to narrow with further development (Vigier *et al.*, 2004; Zhou *et al,* 2004).

2.2.3.5 Molten Carbonate Fuel Cell (MCFC)

MCFCs are high-temperature fuel cells that operate at temperatures of 600°C and above. The higher operating temperature allows them to use crude reformate without the need for elaborate fuel processing. Developed in the mid-1960's, improvements have been made in fabrication methods, performance, and endurance (Williams *et al.,* 2004). MCFCs work differently than do other fuel cells. These cells use an electrolyte composed of a molten mixture of carbonate salts. Two mixtures of carbonate salts are used: lithium carbonate-potassium carbonate (Li_2CO_3 -K_2CO_3), or lithium carbonate-sodium carbonate (Li_2CO_3 -Na_2CO_3), and are retained in a ceramic matrix of $LiAlO_2$. MCFCs operate at high temperatures (~ 650°C) to melt the carbonate salts and achieve high ion mobility through the electrolyte, When melted, these salts become highly conductive to carbonate ions (CO_3^{2-}).

The higher operating temperature of MCFCs has both advantages and disadvantages compared to the lower operating temperature of PAFCs and PEMFCs. At the higher operating temperature, an external reformer to convert more energy-dense fuels to hydrogen is not required. Other advantages include the ability to use inexpensive materials for construction, such as stainless steel sheet, and the ability to use nickel-based catalysts on the electrodes. The by-product heat from a MCFC can be used to generate high-pressure steam that can be used in many industrial and commercial applications. The high temperatures and the electrolyte chemistry also have disadvantages. The high temperature requires more time to reach operating conditions and responds slowly to changing power demands. The carbonate electrolyte can also cause electrode corrosion problems (Yuh & Farooque, 2002), decreasing cell life. Furthermore, since CO_2 is consumed at the anode and transferred to the cathode, introduction of CO_2 and its control in air stream becomes an issue for achieving optimum performance that is not present in any other fuel cell (Hemmes *et al*, 1999).

2.2.3.6 Solid Oxide Fuel Cell (SOFC)

The SOFC produces electricity directly from oxidizing a fuel. The SOFC is the highest-temperature fuel cell in development and can be operated over a wide temperature range from 600°C to 1000°C. At these temperatures, SOFC's do not require expensive platinum catalyst material. A number of fuels can be used in the SOFC. To operate at such high temperatures, the electrolyte is a thin, ceramic material (usually Y_2O_3-stabilized ZrO_2) that is conductive to the charge carrier oxygen ion (O^{2-}). SOFCs have been developed since the late 1950's. The operating efficiency for generating electricity is about 60%. The high operating temperature allows cogeneration applications to create high-pressure

steam that can be used in many applications. SOFCs operate at extremely high temperatures resulting in a significant time required to reach operating temperature and responding slowly to changes in electricity demand. It is therefore considered to be a leading candidate for high-power applications including industrial and large-scale power stations (Minh, 2004).

The very high operating temperature of the SOFC has advantages and disadvantages. The high temperature enables them to use relatively impure fuels, such as those obtained from the gasification of coal or gasses from industrial process and other sources. The high temperatures, however, require more expensive materials of construction (Fergus, 2004).

References

Appleby, A. J. & Yeager, E. (1986). *Energy*, 1 1 (1 - 2), 137-152.

Arico, A. S., Srinivasan, S. & Antonucci, V. (2001). *Fuel Cells*, 1 (2), 133-161.

Bacon, F. (1969). *Electrochimica Acta*, 14, 569-585.

Barceloux, D. G., Bond, G. R., Krenzelok, E. P., Cooper, H. & Vale, J. A. (2002). *Journal of Toxicology, Clinical Toxicology*, 40(4), 415-446.

Belieres, J.P., Gervasio, D. , and Angell, C.A., *Chem. Commun.* 46**,** 4799-4801 (2006).
Chum, H.L., V.R. Koch, L.L. Miller, and R. A. Osteryoung. *J .Am .Chem. Soc.* 97 (1975): 3264.

Cropper, M. A. J., Geiger, S. & Jollie, D. M. (2004). *Journal of Power Sources*, 131(1-2), 57-61.

Dillon, R., Srinivasan, S., Arico, A. S. & Antonucci, V. (2004). *Journal of Power Sources*, 127(1-2), 112-126.

Fergus, J. W. (2004). *Solid State Ionics*, 171(1-2), 1-15

Fitzgerald, R. *Physics Today* 54 (2001): 22.

Greaves, T.L. and Drummond, C.J., *Chem. Rev.* 108, 206-237 (2008).

Grove, W. R. (1839). *Philosophical Magazine and Journal of Science*, 14, 127-130.

Grove, W. R. (1842). *Philosophical Magazine and Journal of Science*, 21, 417-420.

Hemmes, K., Peelen, W. H. A. & De Wit, J. H. W. (1999). *Electrochemical and Solid-State Letters*, 2(3), 103-106.

Hoogers, G. (2003). *Fuel Cell Technology Handbook*. CRC Press.

Hurley, F.H. *J. Electrochem.Society* 98 (1951): 207-212.

Ishizawa, M., Okada, S. & Yamashita, T. (2000). *Journal of Power Sources*, 8 6 (1 - 2), 294-297.

Kordesch, K., Gsellmann, J., Cifrain, M., Voss, S., Hacker, V., Aronson, R. R., Fabjan, C., Hejze, T. & Daniel-Ivad, J. (1999). *Journal of Power Sources*, 80(1- 2), 190-197.

Litster, S. & McLean, G. (2004). *Journal of Power Sources*, 130(1-2), 61-76.

McLean, G. F., Niet, T., Prince-Richard, S. & Djilali, N. (2002). *International Journal of Hydrogen Energy*, 27(5), 507-526.

Minh, N. Q. (2004). *Solid State Ionics*, 174(1-4), 271-277.

Mond, L. & Langer, C. (1889). *Proceedings of the Royal Society*, 46, 296-304.

Ohno, H. *Electrochemical Aspects of Ionic Liquids.* New Jersey: John Wiley & Sons, Inc., 2005.

Penner, S. S., Appleby, A. J., Baker, B. S., Bates, J. L., Buss, L. B., Dollard, W. J., Fan, P. J., Gillis, E. A., Gunsher, J. A., Khandkar, A., Krumpelt, M., O'Sullivan, J. B., Runte, G., Savinell, R. F., Selman, J. R., Shores, D. A. & Tarman, P. (1995). *Energy*, 20(5), 331-470.

Rogers, R.D., and K.R. Seddon. *Ionic Liquids Industrial Applications for Green Chemistry.* Washington D.C.: American Chemical Society, 2002.

Schultz, T., Zhou, S. & Sundmacher, K. (2001). *Chemical Engineering and Technology*, 24(12), 1223-1233.

Vielstich, W., Lamm, A. & Gasteiger, H. (2003). *Handbook of Fuel Cells: Fundamentals, Technology and Applications*, vol. 1-4. John Wiley & Sons.

Vigier, F., Coutanceau, C., Perrard, A., Belgsir, E. M. & Lamy, C. (2004). *Journal of Applied Electrochemistry*, 34, 439-446.

Walden, P. "Bull. Acad. Sci." 1914: 405-422.

Wasserscheid, P. and Welton, T. (eds.), *Ionic Liquids in Synthesis,* 2nd ed. (Wiley-VCH, Weinheim, 2003).

Williams, M. C., Strakey, J. P. & Singhal, S. C. (2004). *Journal of Power Sources,* 131(1-2), 79-85.

Yuh, C.-Y. & Farooque, M. (2002). *Advanced Materials and Processes*, 160(7), 31-34.

CHAPTER 3

TRANSPORT PROPERTIES OF 2-FLUOROPYRIDINIUM TRIFLATE

3.1 Introduction

Neat proton-containing salt electrolytes, or protic ionic liquids (PILs), were made and studied as alternatives for fuel cell operation over conventional water based acid electrolytes by Jeffrey Thomson in 2010 (Thomson 2010). Among the eight ionic liquids tested, 2-fluoropyridinium triflate (2- FPTf) showed the highest proton conductivity and the best fuel cell performance. The voltammograms of Pt in neat 2-FPTf salt electrolyte equilibrated with 1 atmosphere of argon and oxygen were stable for many hours at 80°C. The polarization curve for 2-FPTf at 80°C showed a 0.1 V voltage gain (15% more efficient) over all current densities compared to that with aqueous 85% phosphoric acid electrolyte. Although performance with 2-FPTf was not quite as good as TFMSA-monohydrate, the result with 2-FPTf is still quite remarkable, since triflic acid is considered one of the best acid electrolytes to use for Pt-catalyzed oxygen electroreduction and hydrogen electrooxidation (Adams & Foley, 1979).

We have studied proton and fluorine diffusivity and ionic conductivity of 2-FPTf over a wide range of temperatures. 2-FPTf was very stable under the conditions of this study. This is the first time, to our knowledge, that ionic diffusivities have been measured in 2-FPTf.

3.2 Experimental

3.2.1 Sample

The sample used was protic ionic liquid (PIL) 2-fluoropyridinium triflate (2-FPTf). Commercially available 99% trifluoromethanesulfonic acid (TFMSA or triflic acid) and 98% 2-fluoropyridine from Sigma-Aldrich were combined to synthesize the desired 2-FPTf. TFMSA was the Brønsted acid (proton donor) and 2-fluoropyridine was the Brønsted base (proton acceptor) during the reaction. Both TFMSA and 2-fluoropyridine were diluted in acetonitrile then 1 mole (slight excess) of 2-fluoropyridine was dropped into 1 mole of TFMSA while stirring and cooling the reaction vessel in an ice water bath. After mixing thoroughly the acid together with the base, the acetonitrile solvent was removed from the vessel by drying in a rotary evaporator heated at 80°C under vacuum. The resulting 2-FPTf was then dried in an oven at 85°C under dry nitrogen atmosphere for 48 hours. Being very hygroscopic, the 2-FPTf was stored tightly sealed in a glass container inside a dry-box. The PIL was synthesized according to the following reaction scheme:

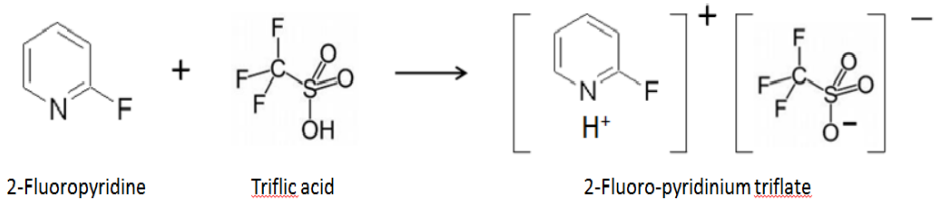

Figure 3.1 2-Fluoro-pyridinium triflate

3.2.2 Diffusivity Measurement

3.2.2.1 Equipment

Diffusivity measurements for ^{1}H was made using the pulsed-gradient spin-echo (PGSE) technique on a 300 MHz NMR spectrometer (a Varian Infinity 300). This spectrometer

has a superconducting magnet of field strength ~7 tesla in which ^{1}H has resonance frequency of approximately 300 MHz. The radio-frequency pulses were generated by a Varian/Chemagnetics broadband transmitter and the gradient pulses were generated by a Resonance Research, Inc. triple axis gradient amplifier (only the Z channel was used for this experiment). Temperature was controlled by heated gas flow around the sample, monitored and adjusted (to a precision of ± 0.1°C) by a Varian/Chemagnetics temperature controller. The probe used was a modified Varian/Chemagnetics 300MHz two channel (H and X) liquids NMR probe which has built in gradient and r.f. coils. The resolution of this probe is not high, of order 0.2 ppm, but it can resolve spectral lines of liquids whose ^{1}H chemical shifts show differences of 0.3 ppm or greater. Such is the case with the ^{1}H spectrum of 2FPTf, as discussed later. The spectrometer was controlled by Varian's Spinsight, an NMR data acquisition and processing software running on a Sun Microsystems workstation.

3.2.2.2 NMR Pulse Sequences

In the basic NMR experiment, the sample is placed in the homogeneous portion of an applied DC magnetic field H_0, while an oscillatory r.f. field H_1 is applied by a pulse of r.f. current in a coil whose axis is perpendicular to H_0. The H_1 field rotates the magnetization within the sample away from the thermal equilibrium position aligned with the H_0 field. The most common H_1 pulse lengths are adjusted to rotate the magnetization, which is initially along the +Z direction, either by 90° into the XY plane, or by 180° to the –Z direction -- see Fig. 3.2.

The first of these pulses generates what is known in NMR spectroscopy as the 90° free induction decay (FID). After the 90° pulse (and actually during it), the magnetization

precesses around the +Z axis at the Larmor frequency. This motion induces an emf in the coil used to apply the 90° r.f. pulse. The signal obtained from the precession decays as the magnetization returns to the equilibrium state. This decaying signal is called the FID, which in most liquids takes the form of a sine wave decaying exponentially over time at a rate $1/T_2$, called the spin-spin relaxation rate. Simultaneously, the magnetization returns to an orientation parallel to the DC magnetic field, growing exponentially at a rate $1/T_1$, where T_1 is called the spin-lattice relaxation time. The NMR spectrum generated from the Fourier Transform of the 90-FID consists usually of one or more absorption lines of various widths. The chemical compound containing the observed nuclear species can be identified by its characteristic line pattern in spectra, which arises from the different chemical shifts of inequivalent nuclei (e.g., protons) in the molecule.

Another commonly used pulse sequence in NMR is the spin-echo pulse sequence. This is a 90-τ-180-τ-signal acquisition sequence, where τ is a variable delay time (Fig. 3.3, (a) and (c)). After the initial 90° pulse, which rotates magnetization down into the XY plane, the transverse precession motion of the individual nuclear magnetic moment of atoms begins to decay, due in part to small variations in Larmor frequency over the entire sample of spins. After a given delay τ following the 90° pulse, a 180° pulse is applied. This pulse rotates the magnetization by 180° about the X axis, placing the faster moving magnetic moments behind the slower. After a second time delay τ, identical to the first, the magnetic moments rephase, at least partially, to produce a signal referred to as a spin-echo. The amplitude of this echo signal decreases exponentially with increasing delay τ due to spin-spin relaxation, with time constant T_2, also called the transverse relaxation time.

3.2.2.3 The PGSE Technique

The diffusion coefficient can be measured using the PGSE sequence. This technique, developed by Stejskal and Tanner in the mid 1960's (Stejskal & Tanner, 1965), is primarily used for studying translational diffusion, although it is also capable of measuring both rotational and translational diffusion coefficients.

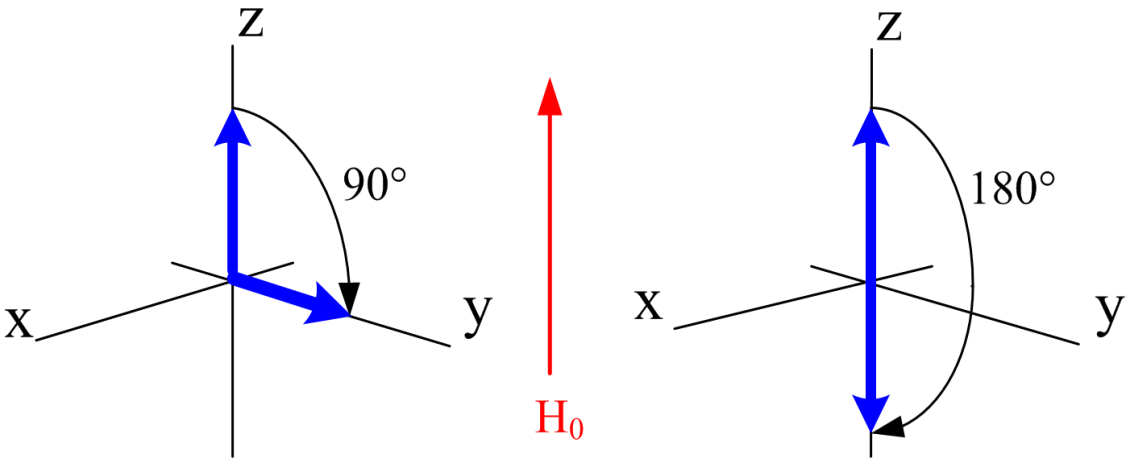

Figure 3.2 90° and 180° pulses rotating the magnetization into the XY plane and towards –Z respectively.

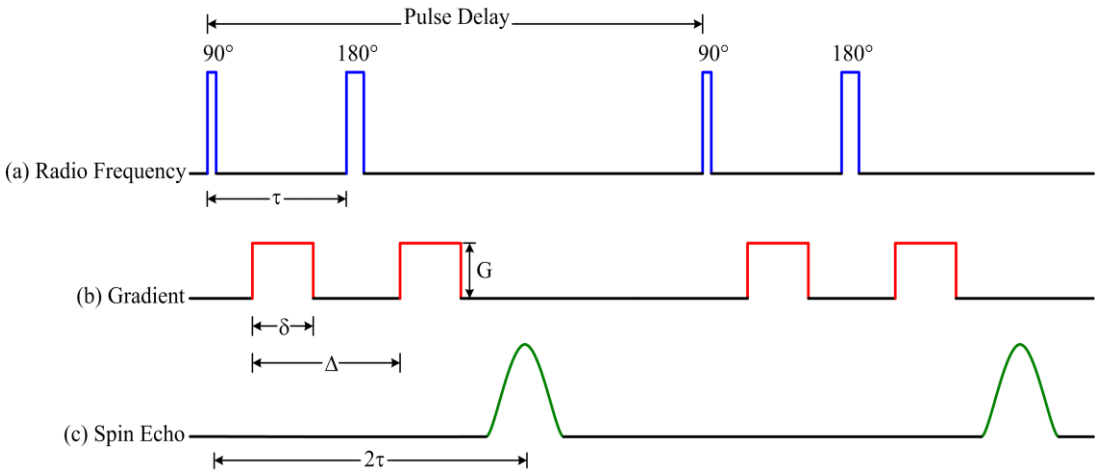

Figure 3.3 The PGSE pulse sequence timing diagram. (a) The 90° and 180° r.f. pulses. (b) The gradient pulses. (c) The spin-echo signal.

The timing diagram for this sequence is shown in Figure 3.3. This sequence uses the spin-echo sequence with two gradient pulses applied, each one following an r.f. pulse. The two gradient pulses have identical amplitudes, G, and widths, δ. They are separated by a time Δ which is effectively the same as the r.f. pulse spacing τ, and δ is always less than τ. The gradient pulses subject the magnetization to rapid diffusive decay, during each pulse (Abragam, 1978). The gradients have no effect on stationary spins, since the phase difference from spin to spin induced by the first gradient pulse gets cancelled by the second one, because they are on opposite sides of the 180° pulse. The net effect of the phase shift on the diffusing spins is that their spin-echo signal is attenuated strongly, the decay following an exponential ($-\delta^2$) dependence on gradient pulse width δ, for fixed gradient pulse spacing Δ.

In the PGSE NMR experiment, the observed spin-echo attenuation also depends strongly upon the gradient strength G. In a sufficiently homogeneous main static field H_0 the gradient-induced decay is given by

$$S(\delta)/S_0 = \exp\{-(\gamma G\delta)^2(\Delta - \delta/3)D, \tag{3.1}$$

Here $S(\delta)$ is the observed spin-echo signal intensity with the pair of gradient pulses applied, S_0 the spin-echo signal intensity in the absence of an applied gradient, γ the nuclear gyromagnetic ratio, D the self-diffusion coefficient along the direction of the applied gradient, and $G = kx \ (0 \le x \le 1)$ where k is the gradient constant of the probe and x the fraction of maximum gradient amplitude. From Eq. (1) we get

$$\ln S(\delta) = \ln S_0 - (\gamma kx\delta)^2(\Delta - \delta/3)D, \tag{3.2}$$

or,

$$\ln S(\delta) = \{-(\gamma k\delta)^2(\Delta - \delta/3)D\}x^2 + \ln S_0, \tag{3.3}$$

A plot of $\ln S(\delta)$ versus x^2, referred to as a Stejskal-Tanner plot, yields a linear relationship with slope $\{-(\gamma k\delta)^2(\Delta - \delta/3)D\}$. Since γ, k, δ, and Δ are known for a particular PGSE experiment, D for the observed nuclei can be calculated.

There are several advantages to this method. Because the gradient is off at the time of the r.f. pulses, only a moderate power r.f. pulse transmitter is required. The gradient is off at the time of the spin-echo as well, so a narrow band detection system may be used. Furthermore, changing the gradient does not change the shape of the echo signal; diffusion changes its amplitude only. With modern spectrometers, diffusivities can be

measured under a wide range of conditions with a precision approaching ± 1% (Holz & Weingartner, 1991).

3.2.2.4 Procedure

a. The solid 2-FPTf was broken into small pieces and then inserted into a fresh 5.0 mm outer diameter NMR tube and then sealed tightly with Teflon tape. The sample filled the tube to a height of approximately 10 mm placing it in the middle of the gradient and the r.f. coils when the tube was inserted into the liquid NMR probe. The probe containing the sample was then raised into the bore of the spectrometer magnet. The temperature controller was set to place the temperature of the sample at 55°C. At least 30 minutes were allowed for the sample to stabilize to the set temperature.

b. In order to obtain NMR signals, the narrow-band NMR probe must first be tuned to the Larmor frequency of the nucleus being observed. For ^{1}H it is 300 MHz and for ^{19}F it is approximately 282 MHz. For tuning, an r.f. signal at the selected frequency is sent to the probe from a transmitter in the spectrometer at 1 second intervals, and the signal reflected from the probe is monitored on a digital oscilloscope. The matching and tuning capacitors of the probe were adjusted so the amplitude of the reflected signal was minimized. This ensured the matching of the probe to the 50Ω transmission line, yielding maximum signal to noise ratio at the NMR frequency.

c. The 90° and 180° r.f. pulse widths were determined by recording a series of spectra with incrementally longer pulse widths, then plotting the Fourier transformed FID's at each pulse width. The 7.5 ppm peak height varied sinusoidally with increasing r.f pulse width. The first maximum of the sinusoid was the 90° pulse width and the first zero crossing was the 180° pulse width.

d. The optimum pulse interval between spin-echo sequences was determined by recording a series of 90-FID's with incrementally longer intervals between acquisitions, then plotting the Fourier transformed FID's as a function of pulse delay. The peak height increased with increasing acquisition interval and reached a maximum at around $5T_1$, which was then used as the interval between applications of the PGSE sequence.

e. The PGSE signal acquisition sequence was begun, applying incrementally larger gradient pulses starting with zero gradient amplitude. Since the intensity of the signal was attenuated with larger gradients, incrementally higher numbers of acquisitions were made to maintain good signal-to-noise ratios. The numbers of acquisitions were set to multiples of eight due to the four-phase cycling employed to eliminate quadrature artifacts. PGSE signals corresponding to at least eight increments of gradient amplitude were recorded.

f. The averaged PGSE signal at each gradient amplitude setting was Fourier transformed. The area under each curve (in arbitrary units) represents the intensity of the signal. The log of the averaged intensity was plotted against the square of the gradient amplitude. The diffusivity of ^{1}H was calculated from the slope of a linear fit using Equation (3.1).

g. **.** Diffusivity of ^{19}F at 70°C was measured using the same procedure. The probe was tuned to 282.26 MHz, the resonance frequency of ^{19}F in our magnet. Diffusivity of ^{1}H and ^{19}F was measured at 10°C increments up to 115°C.

3.2.3 Conductivity Measurement

3.2.3.1 Equipment

Conductivity measurements were made by electrochemical impedance spectroscopy (EIS) using a PARStat 2273 Potentiostat, which was operated by a PC running the

Powersine software package. The sample was held in a two-electrode cell, connected to two wires for applying voltage and two separate wires for passing current using the electrochemical interface. Temperature of the sample was controlled by placing the cell inside an electric oven containing a mineral oil bath. The temperature of the cell was assumed to be the same as the temperature measured in the oil bath. Two thermocouples and a glass thermometer were used for accurate temperature measurement. Complex impedance measurements were made about every 5°C starting from 25°C up to 110°C.

3.2.3.2 EIS Technique

In EIS an AC potential is applied to the electrochemical cell and the current through the cell is measured. The impedance of the cell is calculated from the magnitudes and the phase difference between the potential and the current, and is plotted as a function of the frequency. In EIS, impedance is normally measured using excitation signals of very low amplitude (1 to 10 mV) (Bard & Faulkner, 2001). This is done so that the cell's response is pseudo-linear. In a linear (or pseudo-linear) system, the current response to a sinusoidal potential at a certain frequency will be a sinusoid at (and only at) that same frequency but shifted in phase. If the excitation signal, expressed as a function of time, has the form

$$E_t = E_0 \sin(\omega t), \tag{3.4}$$

where E_t is the potential at time t, E_0 is the amplitude of the signal, and ω is the radial frequency, then in a linear system, the response signal at time t, I_t has the form

$$I_t = I_0 \sin(\omega t + \phi), \tag{3.5}$$

where I_0 is the amplitude of the current response and ϕ is its phase shift. The impedance of the system is given by an expression analogous to Ohm's law:

$$Z = \frac{E_t}{I_t} = \frac{E_0 \sin(\omega t)}{I_0 \sin(\omega t + \phi)} = Z_0 \frac{\sin(\omega t)}{\sin(\omega t + \phi)}, \tag{3.6}$$

The impedance is therefore expressed in terms of a magnitude, Z_0, and a phase shift, ϕ. The impedance can also be expressed as a complex function:

$$Z(\omega) = \frac{E_t}{I_t} = \frac{E_0 e^{i\omega t}}{I_0 e^{i(\omega t - \phi)}} = Z_0 e^{i\phi} = Z_0(\cos\phi + i\sin\phi), \tag{3.7}$$

If the real part of $Z(\omega)$ is plotted on the X axis (resistance) and the imaginary part is plotted on the Y axis (reactance) of a chart, we get a "Nyquist Plot". In this plot the Y axis is negative (capacitive reactance) and each point on the Nyquist Plot is the impedance at one frequency with low frequency data on the right side of the plot and higher frequency data on the left. On the Nyquist plot the impedance can be represented as a vector of length $|Z|$ which makes an angle ϕ $(= \arg Z)$, the "phase angle" with the X axis. Figure 3.4 shows a Nyquist plot for a resistance in series with a paralleled capacitance and resistance as shown in Figure 3.5. The conductivity cell is modeled by an equivalent electrical circuit in which the series resistance, R_S is the resistance of the 2-FPTf, and the two components in parallel, C_P and R_P, are the double layer capacitance between the electrode and sample and the charge transfer resistance for the reversible electrode reaction ($H^+ + e^- \rightarrow \frac{1}{2}H_2$), respectively. The Nyquist plot in Figure 3.4 assumes that the reaction resistance is higher than the rate of mass transfer of hydrogen and proton to the electrode (mass transfer resistance). When the mass transfer resistance is higher

than the charge transfer resistance due to slower diffusion, the Nyquist plot is not a semicircle ascending at R_S and descending at $R_S + R_P$. Instead, with high mass transport resistance, the Nyquist plot is a line starting at R_S with a 45° slope. In this case, C_P and R_P are replaced by a new term called the Warburg impedance (W_P) (Bard & Faulkner, 2001). Since the measurements were made in air (not under a hydrogen atmosphere), a Warburg impedance developed in the cell used to measure sample resistance. Regardless, the highest frequency (leftmost) X axis intercept in the Nyquist Plot can still be used to reliably evaluate the quantity of interest, R_S, the resistance of the ionic solution.

3.2.3.3 The Cell

The cell was constructed from a soft glass tube having an outer diameter of 5.2 mm and an inner diameter of 2.8 mm. The tube was cut to a length of 60 mm and then bent to 90 degree angles at 10 mm from both edges (Figure 3.6). Keeping the two openings upright, two pieces of heated platinum wires (Alfa Aesar, 0.3 mm diameter, 99.9% metals basis) were inserted into the inner chamber of the tube from the top about 20 mm apart. Since platinum and soft glass have the same coefficient of thermal expansion (9.0×10^{-6}/K at 20°C) the possibility of sample leakage from the insertion point due to stress from unequal thermal expansions was minimized.

3.2.3.4 Cell constant

The cell constant of a conductivity cell relates the measured resistance of the electrolyte to its conductivity. Since cell geometry affects its resistance values, standardized measurements of conductivities are expressed in units of S/cm to compensate for variations in electrode dimensions. If R is the measured resistance of the cell in ohms, κ

is the conductivity of the electrolyte in S/cm, and κ_{cell} is the cell constant in 1/cm then

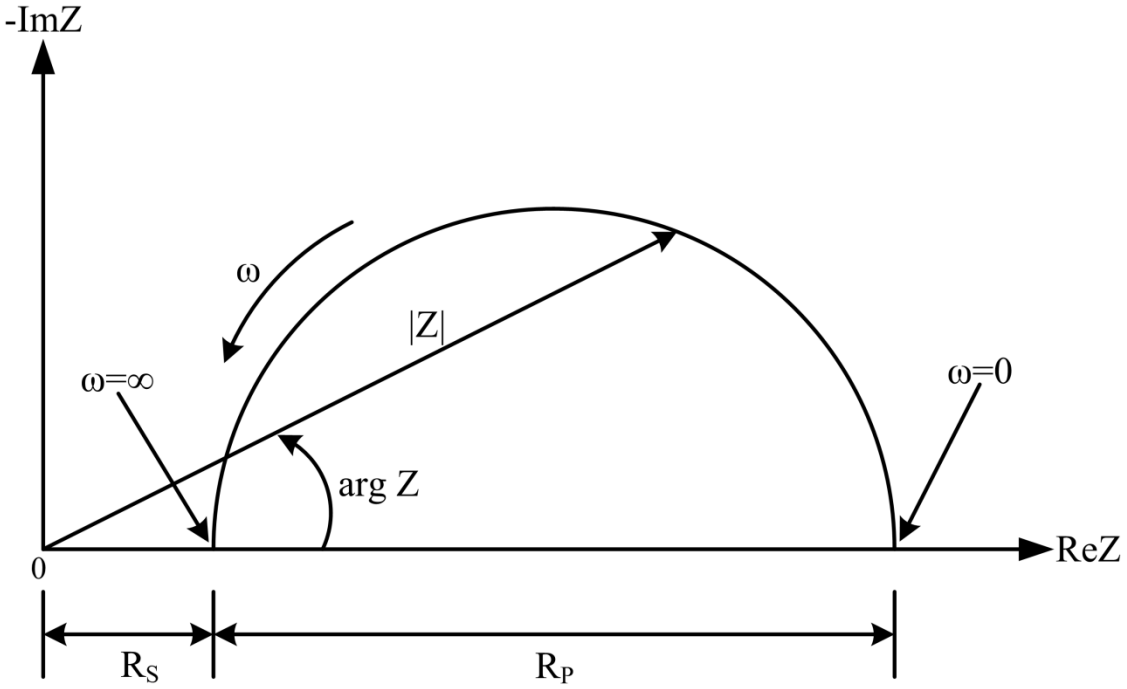

Figure 3.4 The single time constant Nyquist Plot with impedance vector for our conductivity cell. The high and low frequency intercepts of the plot with the real axis give the series resistance, R_S and the sum of the series and the parallel resistances, R_S+R_P respectively.

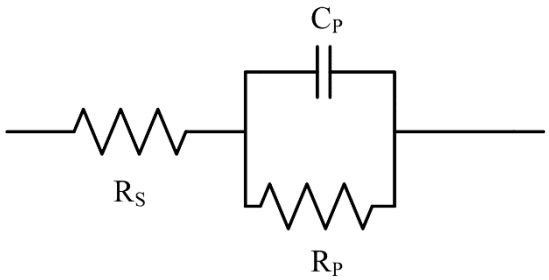

Figure 3.5 An equivalent electrical circuit for our electrochemical cell in the high frequency limit.

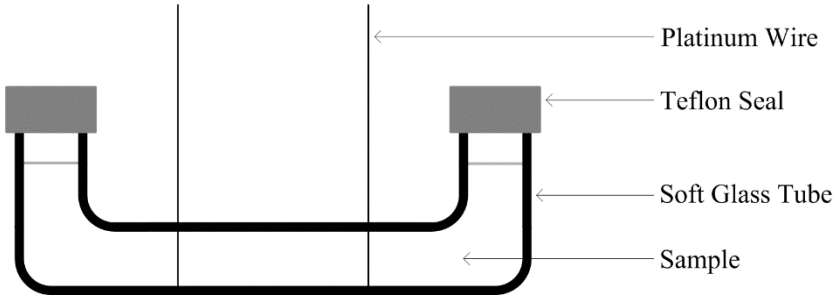

Figure 3.6 Schematic of the electrochemical cell used for conductivity measurements.

$$\kappa = \frac{\kappa_{cell}}{R}, \tag{3.8}$$

If a cell has two parallel plate electrodes each with an area A cm^2 and the column of liquid between the electrodes has a length L cm then κ_{cell} is defined as $\frac{L}{A}$ /cm. Since our cell did not have parallel plates as electrodes and it was not possible to find the electrode area perpendicular to the current, standard concentrations of NaCl aqueous solutions with known conductivities (Cole-Parmer Technical Library) were used to find the cell constant.

3.2.3.4 Procedure

a. The cell was cleaned using acetone, methanol, 18 MΩ-cm deionized water, and by passing clean, dry, and filtered nitrogen through it to remove the final traces of solvents.

b. About 0.25 ml of 0.1% weight NaCl aqueous solution was inserted into the cell with a pipette. The solution was poured very slowly to prevent any air bubbles from forming inside the tube on or around the electrodes. The openings of the cell were then sealed with Teflon tape.

c. The first Reference Electrode (RE_1) and the Counter Electrode (CE) wires of the electrochemical interface were connected to one of the platinum electrodes and the second Reference Electrode (RE_2) and the Working Electrode (WE) wires were connected to the second platinum electrode using alligator clips.

d. The cell was placed near the center of the bottom rack an electric oven. One thermocouple was inserted inside a vial filled with mineral oil and placed close to the cell and a second thermocouple was placed near the middle of the oven chamber. To compare the readings from the thermocouples, a glass thermometer was also inserted from the opening on the top of the oven.

e. The temperature of the oven was slowly increased to 25°C. About 30 minutes were allowed for the cell and the solution to stabilize to the oven temperature. Both thermocouples and the glass thermometer had the same temperature reading at that time.

f. An impedance scan was initiated using PowerSine with a frequency sweep starting at 50 kHz and ending at 10 Hz. The AC amplitude was set to 10 mV. Data points were recorded at ten steps per decade on a logarithmic frequency scale. The resulting Nyquist plot was saved for later analysis. Three more sweeps were recorded under the same conditions.

g. Complex impedance measurements were taken for 0.3 and 1.0% weight NaCl aqueous solutions at 25°C following procedures a to f. These data were later used for calculating the cell constant.

h. The cell was thoroughly cleaned, dried, and then filled with 2-FPTf. It was filled as quickly as possible and then sealed tightly with Teflon tape to minimize absorption of moisture by the hygroscopic sample. Complex impedance measurements were made about every 10°C starting from room temperature, 23°C up to 139°C. Three measurements were made at each temperature. These data were used to determine the conductivity of the solution using the procedure described in the results section.

3.3 Results

3.3.1 Diffusivities

The Stejskal-Tanner plots from 7.5 ppm and 13.5 ppm ^{1}H and 78 ppm and 80 ppm ^{19}F diffusivity measurements are shown in Figures 3.7, 3.8, 3.9, and 3.10 respectively. From the slopes of the linear fits, the diffusivities of ^{1}H and ^{19}F were calculated using Eq. (3.3). The gradient constant, k for our diffusion probe was measured using known self-diffusion coefficient value of water (Holz & Weingartner, 1991) at 25°C and was found to be 13.9 T/m. The nuclear gyromagnetic ratio, γ for ^{1}H is 2.6752×10^{8} /T.s and that for ^{19}F is 2.5170×10^{8} /T.s. The width of the gradient pulse, δ was 2.0 ms for both ^{1}H and ^{19}F and the time between the gradient pulses, Δ was 3.0 ms for both ^{1}H and ^{19}F. Tables 3.1 and 3.2 list the slopes of the Stejskal-Tanner plots and the diffusivities for ^{1}H from 55 to 115°C and for ^{19}F from 70 to 115°C respectively. As we can see from Tables 3.1 and 3.2, the diffusivity of the mobile protons (13.5 ppm) increased from 1.84 ± 0.06 x 10(-11)

m2/s at 55° C to 1.64 ± 0.05 x 10(-10) m2/s at 115° C while the diffusivity of the 2-fluoropyridine fluorines (78 ppm) increased from 2.22 ± 0.07 x 10(-11) m2/s at 70° C to 9.40 ± 0.28 x 10(-11) m2/s at 115° C. Figure 3.1 shows the temperature-dependent behavior of the ^{1}H diffusivities and Figure 3.12 shows that of the ^{19}F diffusivities over the observed temperature range.

3.3.2 Conductivity

The cell constant of the electrochemical cell was determined using known conductivities (Cole-Parmer Technical Library) of 0.1, 0.3, and 1.0% weight NaCl aqueous solutions at 25°C. Nyquist plots in the high frequency region were recorded from EIS. The real axis intercepts of the plots gave the cell resistances for the three concentrations. The cell constants were calculated from the three cell resistances using Eq. (3.8). The average cell constant for our electrochemical cell was 46.7 /cm. The results from the cell constant measurement are listed in Table 3.3.

The cell constant and the cell resistances from the real axis intercepts of the Nyquist plots were used to find the conductivity of the solution over that temperature range. The conductivity of the solution increased from 0.85 ± 0.03 mS/cm at 25°C to 35.9 ± 1.08 mS/cm at 110°C. Conductivities were measured above 110°C but are unreliable due to formation of air bubbles on the electrodes and some sample leakage through the insertion points of the platinum wires. Table 3.4 lists the results from the conductivity measurement. Figure 3.13 shows the temperature-dependent behavior of the conductivity of 2-FPTf over the observed temperature range.

3.3.3 Density

Density of 2-FPTf was measured using a standard 6.0 mm inner diameter NMR tube. The mass of the empty tube was measured first then small pieces of solid 2-FPTf were inserted into the tube up to a height of about 2.0 cm. The total mass of the tube and the sample was measured. The sample was then heated inside an oven set at 93.5° C. After about an hour the tube was taken out and the height of the liquid 2-FPTf was quickly marked with a pen. From the height of the liquid and the dimensions of the tube the volume of the sample at 93.5° C and its density was measured. The density of 2-FPTf was found to be 1683.4 ± 8.4 kg/m^3 at 93.5° C.

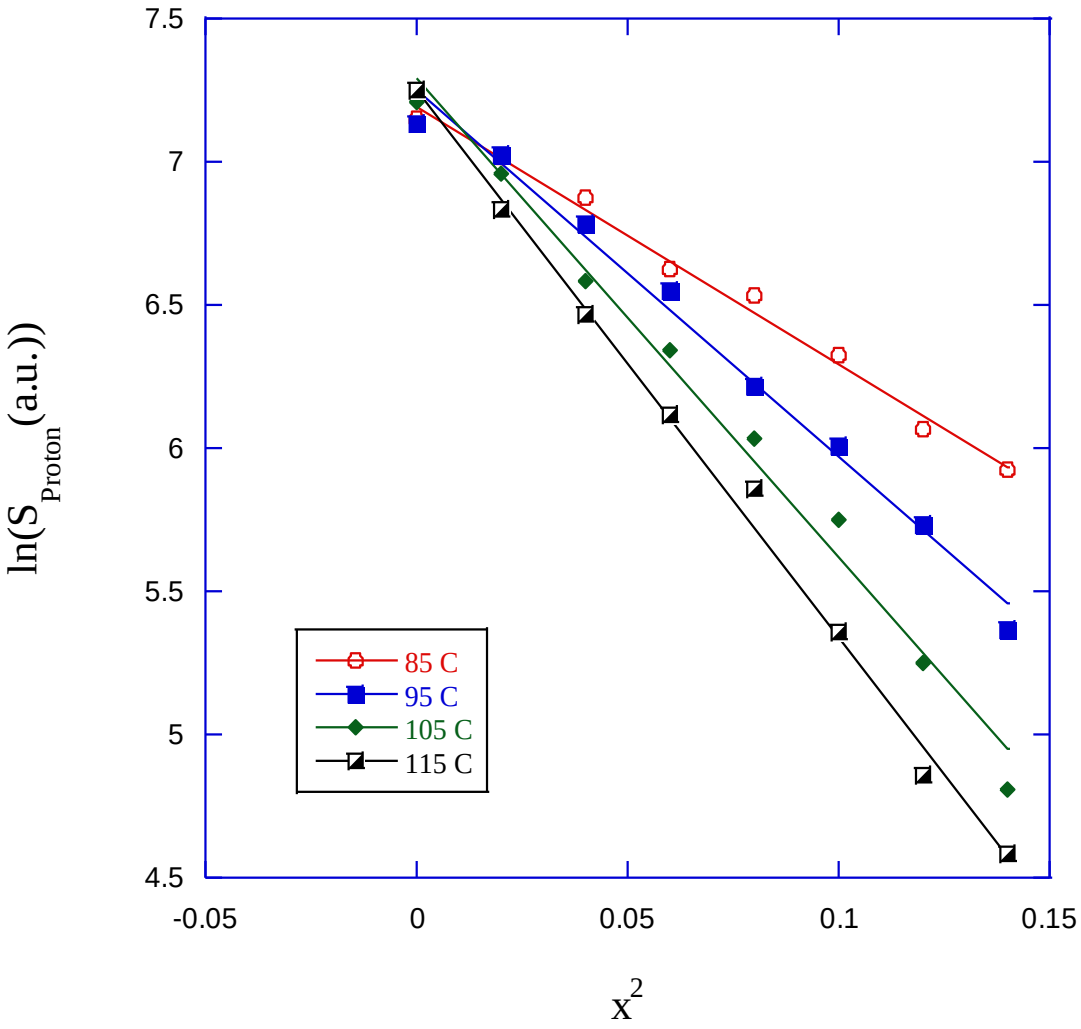

Figure 3.7 Stejskal-Tanner plots from the 7.5 ppm ^{1}H diffusivity measurements above the melting point. The square of the amplitude of the gradient pulse, x is plotted along the X axis and the natural log of the normalized intensity of the spin-echo signal, S_{Proton} is plotted along the Y axis.

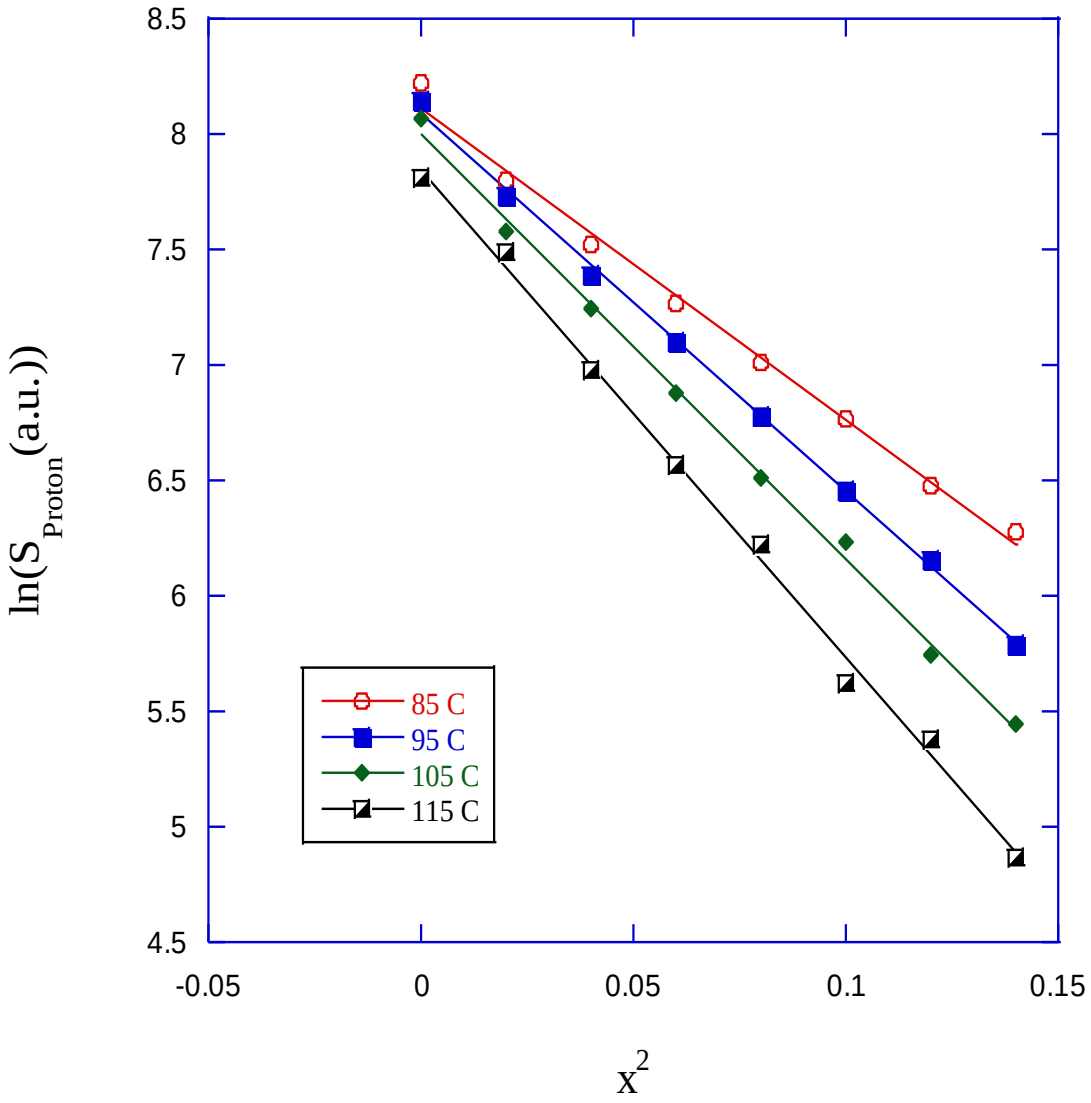

Figure 3.8 Stejskal-Tanner plots from the 13.5 ppm ^{1}H diffusivity measurements above the melting point. The square of the amplitude of the gradient pulse, x is plotted along the X axis and the natural log of the normalized intensity of the spin-echo signal, S_{Proton} is plotted along the Y axis.

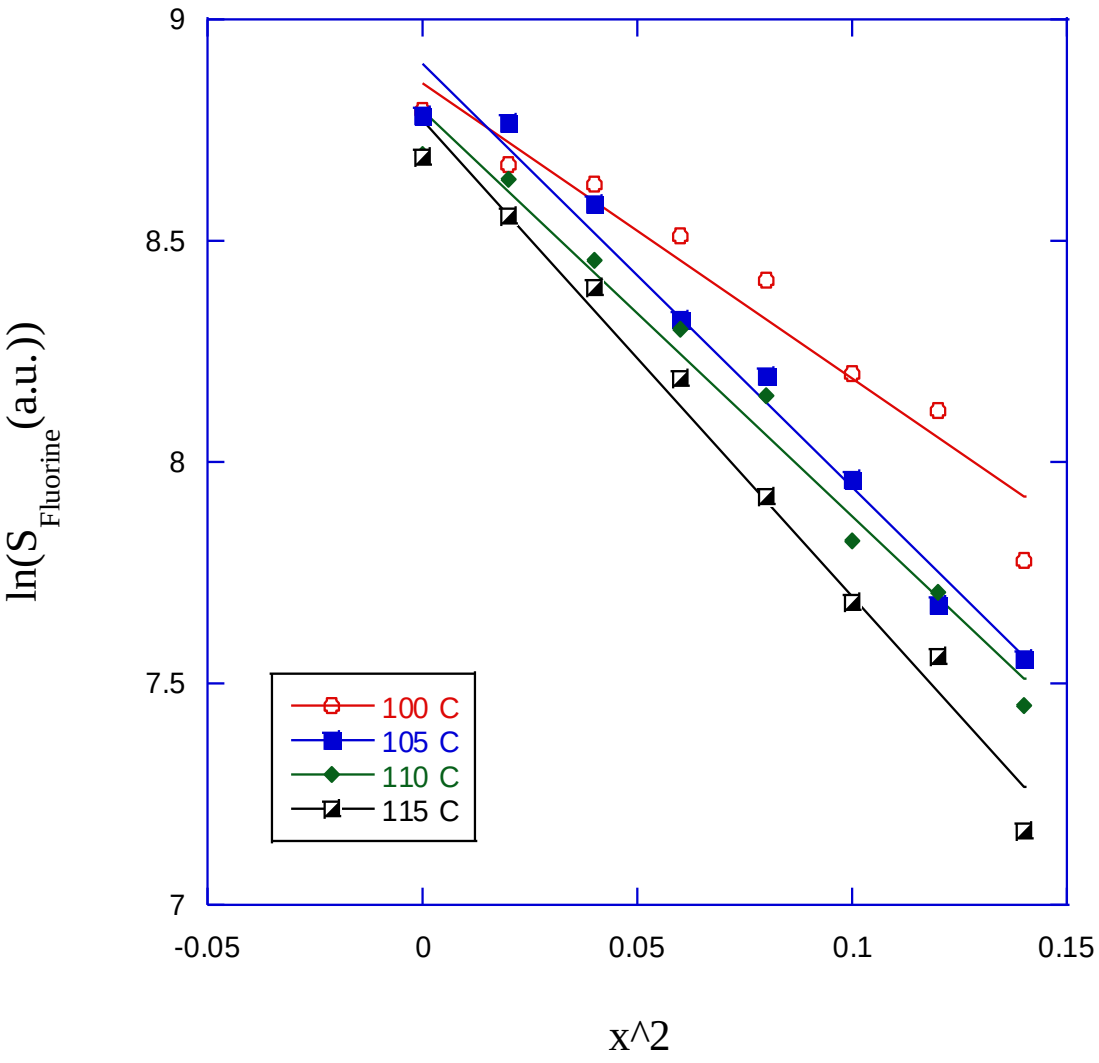

Figure 3.9 Stejskal-Tanner plots from the -78 ppm ^{19}F diffusivity measurements above the melting point. The square of the amplitude of the gradient pulse, x is plotted along the X axis and the natural log of the normalized intensity of the spin-echo signal, $S_{Fluorine}$ is plotted along the Y axis.

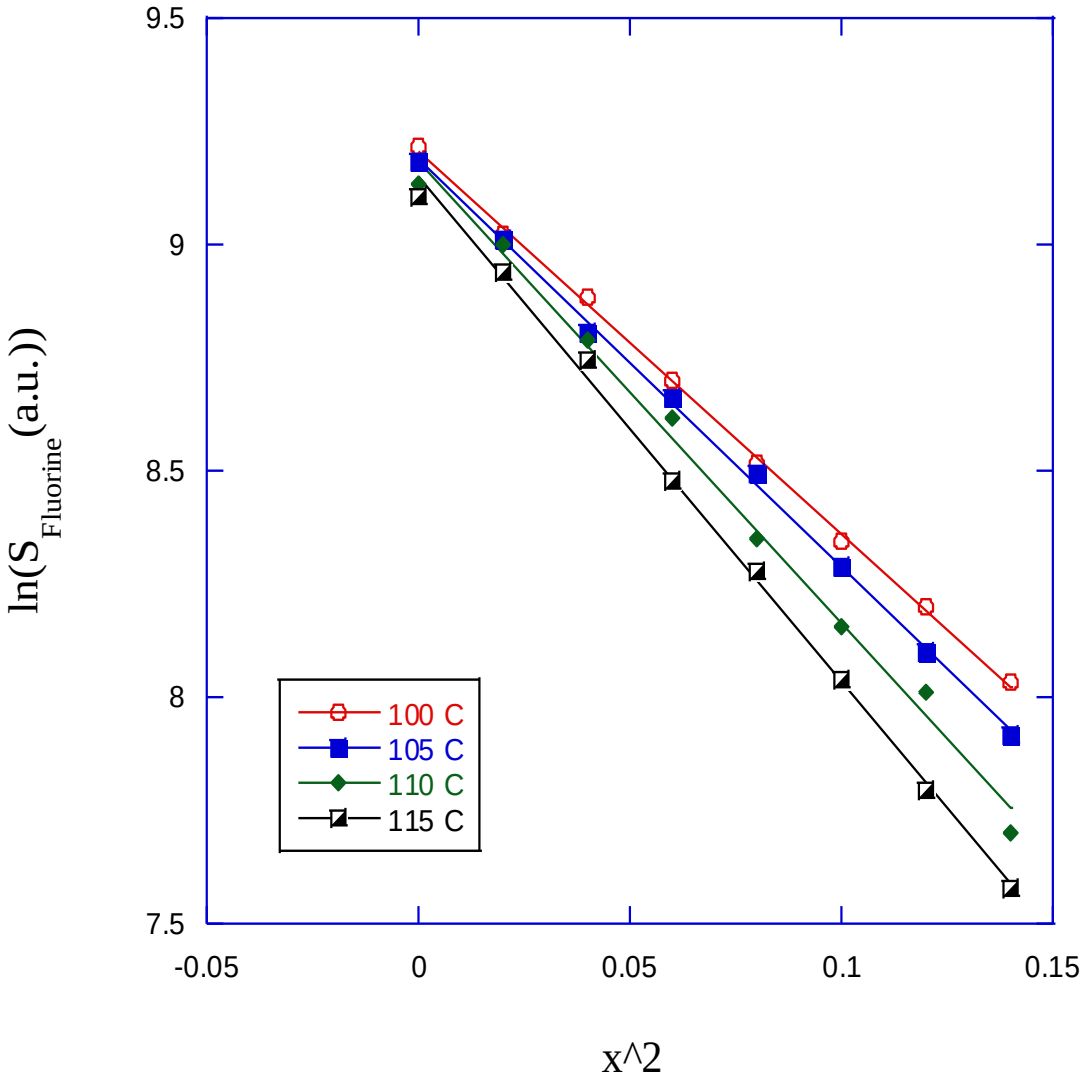

Figure 3.10 Stejskal-Tanner plots from the -80 ppm ^{19}F diffusivity measurements above the melting point. The square of the amplitude of the gradient pulse, x is plotted along the X axis and the natural log of the normalized intensity of the spin-echo signal, $S_{Fluorine}$ is plotted along the Y axis.

Table 3.1: ^{1}H diffusivity[a] of 2FPTf from 55 to 115°C.

Temperature (°C)	Slope for 7.5 ppm ^{1}H	7.5 ppm ^{1}H Diffusivity (m^2/s)	Slope for 13.5 ppm ^{1}H	13.5 ppm ^{1}H Diffusivity (m^2/s)
55	-1.1873	9.1999e-12	-2.3683	1.8351e-11
65	-2.5795	1.9987e-11	-4.0838	3.1644e-11
75	-3.0772	2.3844e-11	-4.9952	3.8706e-11
85	-9.0028	6.9759e-11	-13.529	1.0483e-10
95	-12.785	9.9065e-11	-16.340	1.2661e-10
105	-16.743	1.2973e-10	-18.387	1.4247e-10
115	-19.091	1.4793e-10	-21.161	1.6397e-10

[a] ± 3% error in all diffusivity measurements.

Table 3.2: ^{19}F diffusivity[a] of 2FPTf from 70 to 115°C.

Temperature (°C)	Slope for -78 ppm ^{19}F	78 ppm ^{19}F Diffusivity (m^2/s)	Slope for -80 ppm ^{19}F	80 ppm ^{19}F Diffusivity (m^2/s)
70	-2.5306	2.2151e-11	-3.2149	2.8141e-11
80	-1.4636	1.2811e-11	-3.5475	3.1052e-11
90	-3.7944	3.3213e-11	-5.2873	4.6281e-11
100	-6.6852	5.8517e-11	-8.4451	7.3922e-11
105	-9.5389	8.3496e-11	-9.0151	7.8911e-11
110	-9.1581	8.0163e-11	-10.223	8.9484e-11
115	-10.739	9.4001e-11	-11.149	9.7589e-11

[a] ± 3% error in all diffusivity measurements.

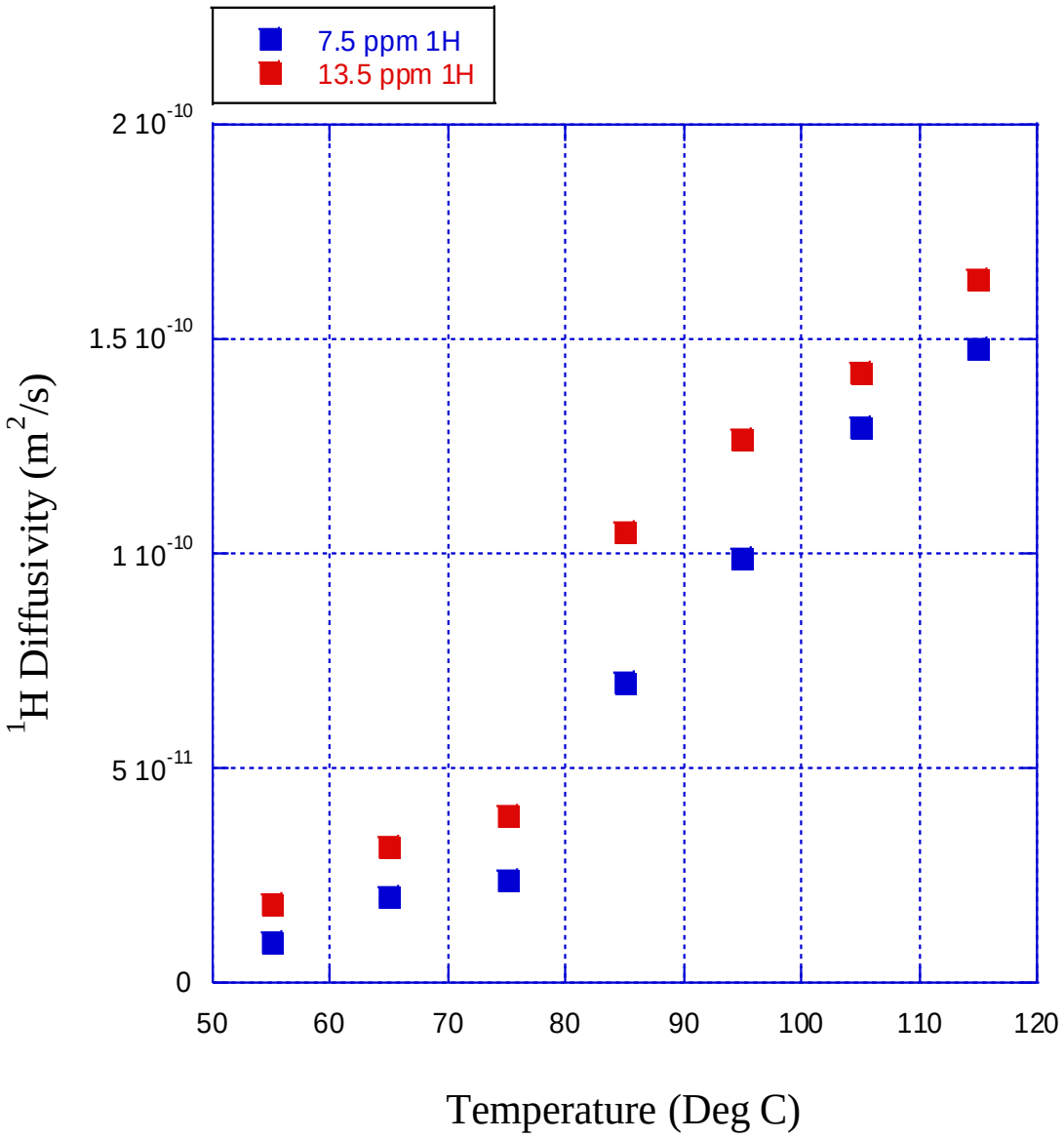

Figure 3.11 ^{1}H diffusivity of 2FPTf from 55 to 115°C.

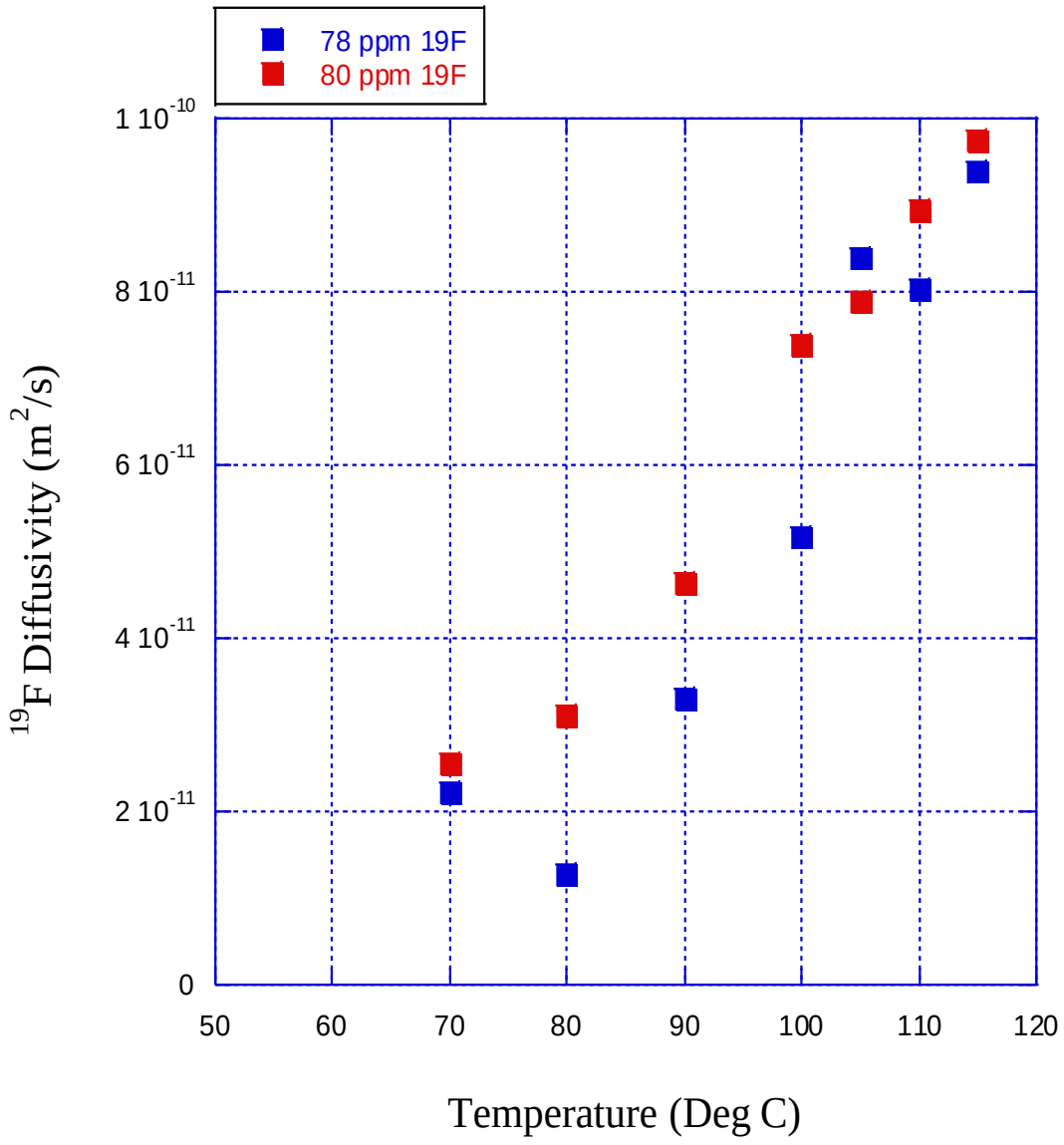

Figure 3.12 ^{19}F diffusivity of 2FPTf from 70 to 115°C.

Table 3.3: Cell constant from known conductivities of standard NaCl aqueous solutions.

NaCl Concentration (% Weight)	NaCl Conductivity[a] (mS/cm)	Cell Resistance (Ohms)	Cell Constant (1/cm)
0.1%	1.99	23500	46.765
0.3%	5.69	8200	46.658
1.0%	17.6	2650	46.640
			46.7 (average)

[a]Cole-Parmer Technical Library.

Table 3.4: Conductivity of 2-FPTf.

Temperature (°C)	Cell Resistance (Ohms)	Conductivity[a] (mS/cm)
25	55000	0.8500
30	40000	1.170
36	27000	1.730
40	21500	2.170
43	17500	2.670
49	12200	3.830
54	8800.0	5.310
57	7700.0	6.060
59	6650.0	7.020
67	3875.0	12.05
73	3375.0	13.83
79	2800.0	16.67
86	2350.0	19.87
89	2200.0	21.22
96	1850.0	25.24
105	1450.0	32.20
110	1300.0	35.91

[a] ± 3% error in all conductivity measurements.

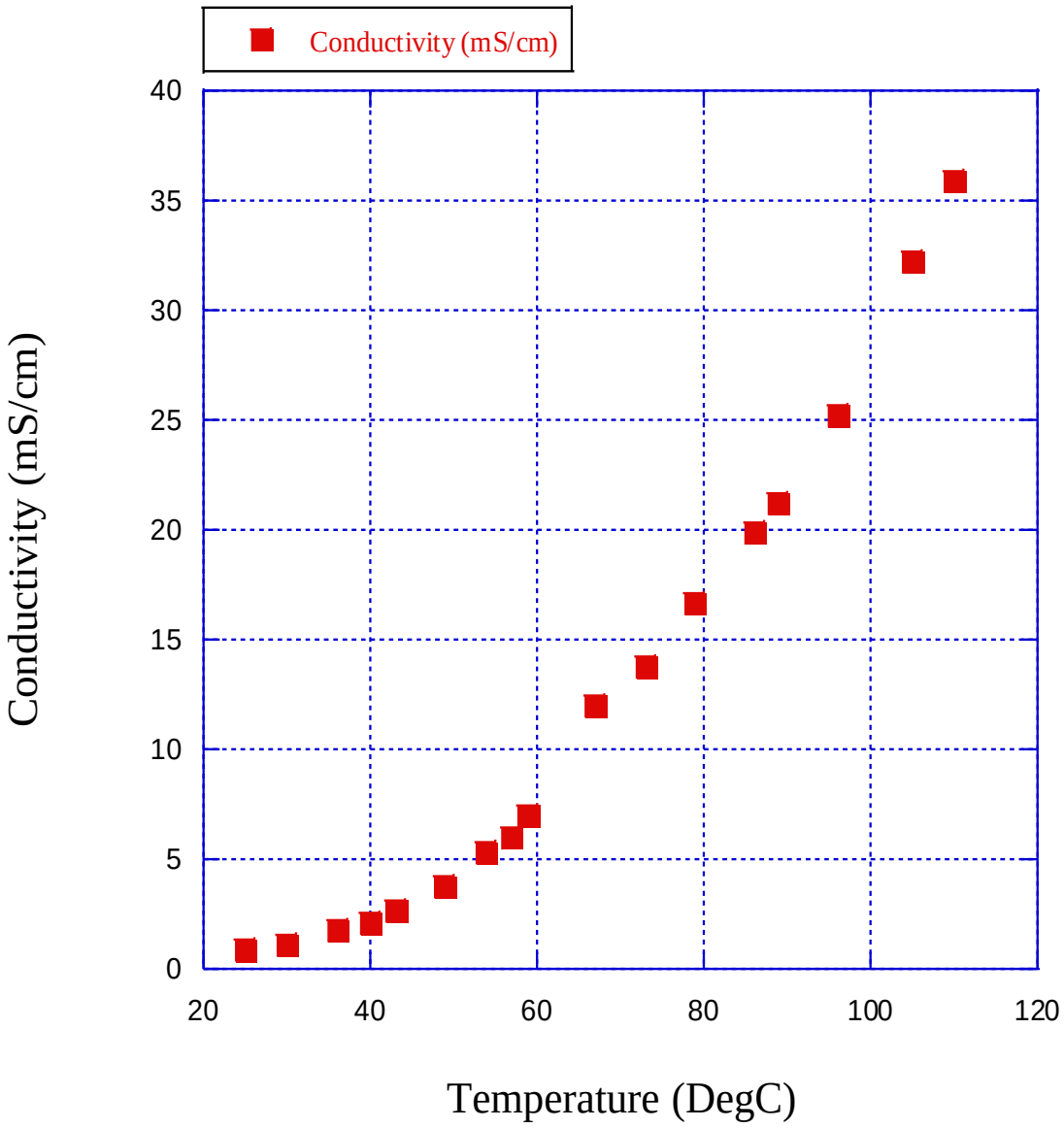

Figure 3.13 Temperature-dependent conductivity of 2-FPTf.

3.4 Discussion

3.4.1 Proton versus fluorine diffusivity

In ^{1}H NMR spectra for 2-FPTf we see two dominant lines: one at 7.5 ppm which is identified with the 2-fluoropyridine protons and another at 13.5 ppm, which is the mobile proton. We measured proton diffusivities on both these lines. The 13.5 ppm proton diffuses faster than the 7.5 ppm over the observed temperature range from 55 to 115°C (Figure 3.14). In the ^{19}F NMR spectra, we see three lines: 78 ppm, 80 ppm, and 82 ppm. The 78 ppm line are the 2-fluoropyridine fluorines and 80 ppm line are the triflate fluorines. The origin of the 82 ppm line is under investigation. We measured fluorine diffusivities on all three lines. In 2-FPTf, the mobile 13.5 ppm protons hop from one cation to another cation, resulting in faster diffusion while the triflate and the 2-fluoropyridine molecules diffuse at nearly equal but slower rate.

3.4.2 Activation energies

The diffusivity of an assembly of molecules at different temperatures is often found to be well predicted by the Arrhenius equation, over wide temperature ranges in liquids:

$$D = D_0 e^{-\frac{E_a}{RT}}, \tag{3.9}$$

Here D is the diffusion coefficient in m^2/s, D_0 is a rate related to an attempt frequency of vibration in an effective potential well for a diffusing molecule, E_a is the activation barrier energy for escape from this well, in J/mol, T is the absolute temperature, and R = 8.314472 J/mol.K is the gas constant. From:

$$\ln D = -\frac{E_a}{R}\left(\frac{1}{T}\right) + \ln D_0, \tag{3.10}$$

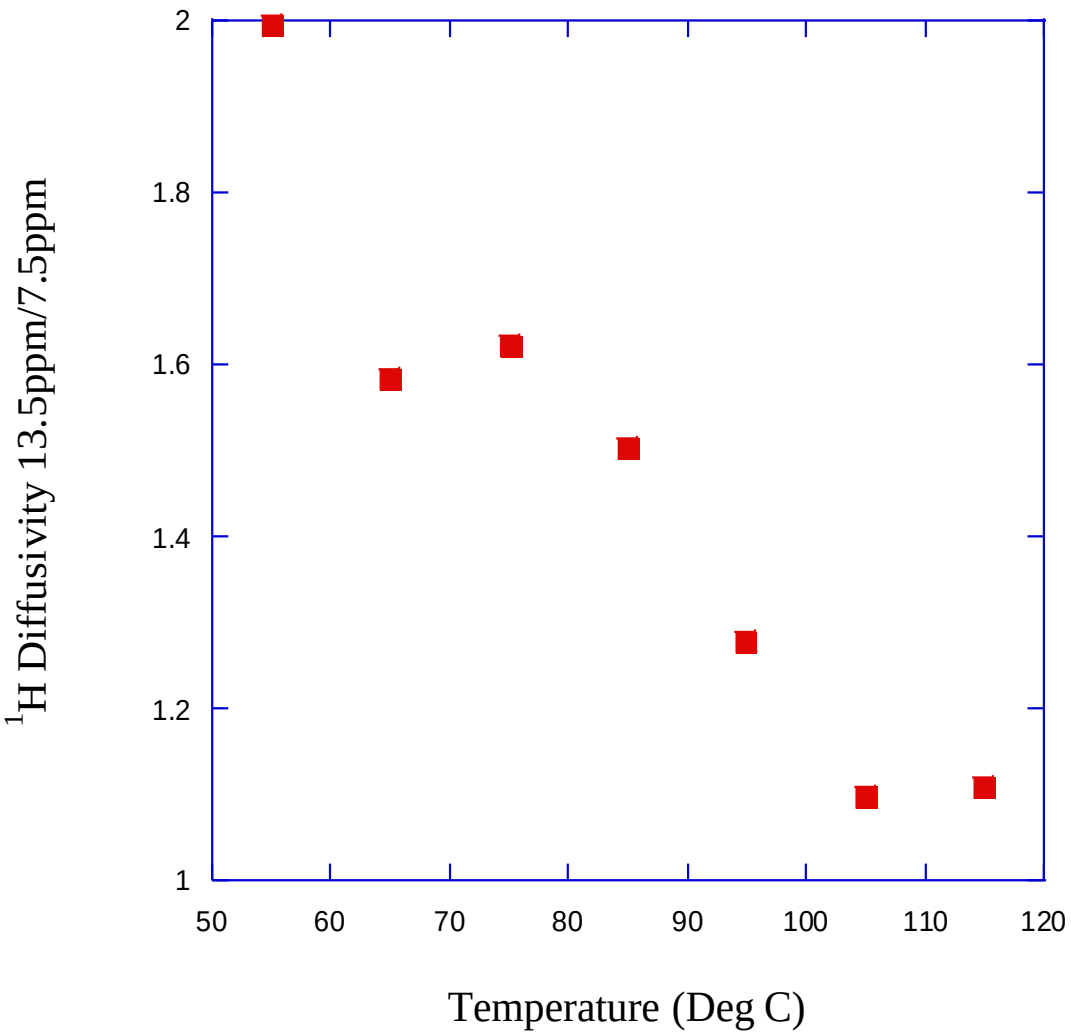

Figure 3.14 Ratio of 13.5 ppm ^{1}H diffusivity to 7.5 ppm ^{1}H diffusivity from 55 to 115°C. The 13.5 ppm ^{1}H is observed to diffuse faster than the 7.5 ppm ^{1}H over the entire temperature range.

a plot of $\ln D$ versus $1/T$ should give a straight line with a slope of $-\frac{E_a}{R}$. Figure 3.15 shows $\ln D$ versus $1/T$ plots for 7.5 ppm and 13.5 ppm protons from 55 to 115°C. As seen from the plots, diffusivities for proton demonstrate Arrhenius behavior above and

below the melting point of 2-FPTf, implying that the mechanisms of diffusion remain unchanged with temperature in those ranges. From the slopes of the lines we find the activation energies for 7.5 ppm and 13.5 ppm protons above the melting point to be 29.3 ± 1.5 kj/mol and 16.9 ± 0.8 kj/mol respectively.

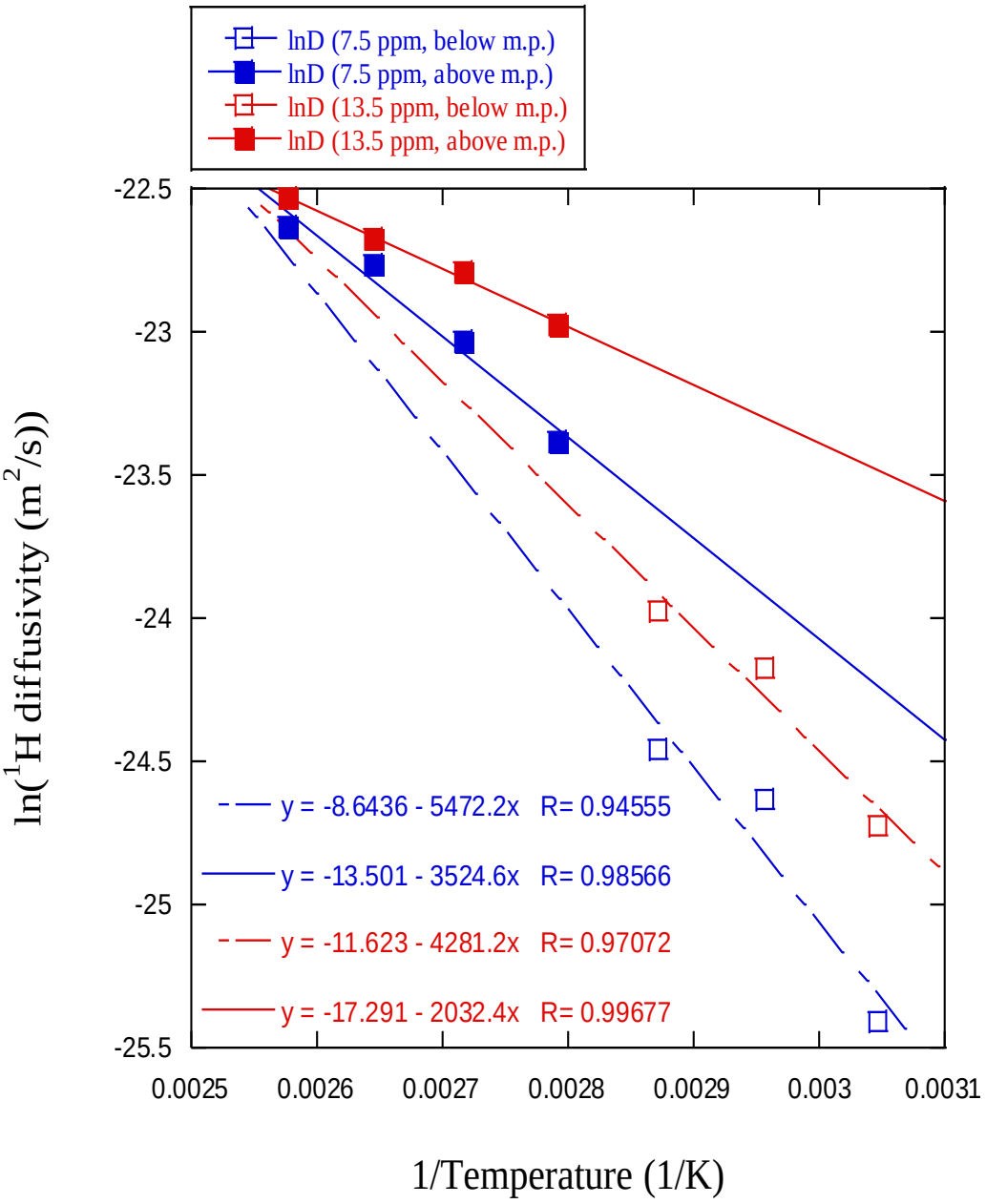

Figure 3.15 ln(Diffusivity) versus 1/Temperature for 7.5 ppm and 13.5 ppm ^{1}H showing Arrhenius behavior from 55 to 115°C.

Similar Arrhenius behavior is observed in the 78 ppm, 80 ppm, and 82 ppm ^{19}F diffusivities above the melting point (Figure 3.16). Activation energies for the 78 ppm, 80 ppm, and 82 ppm

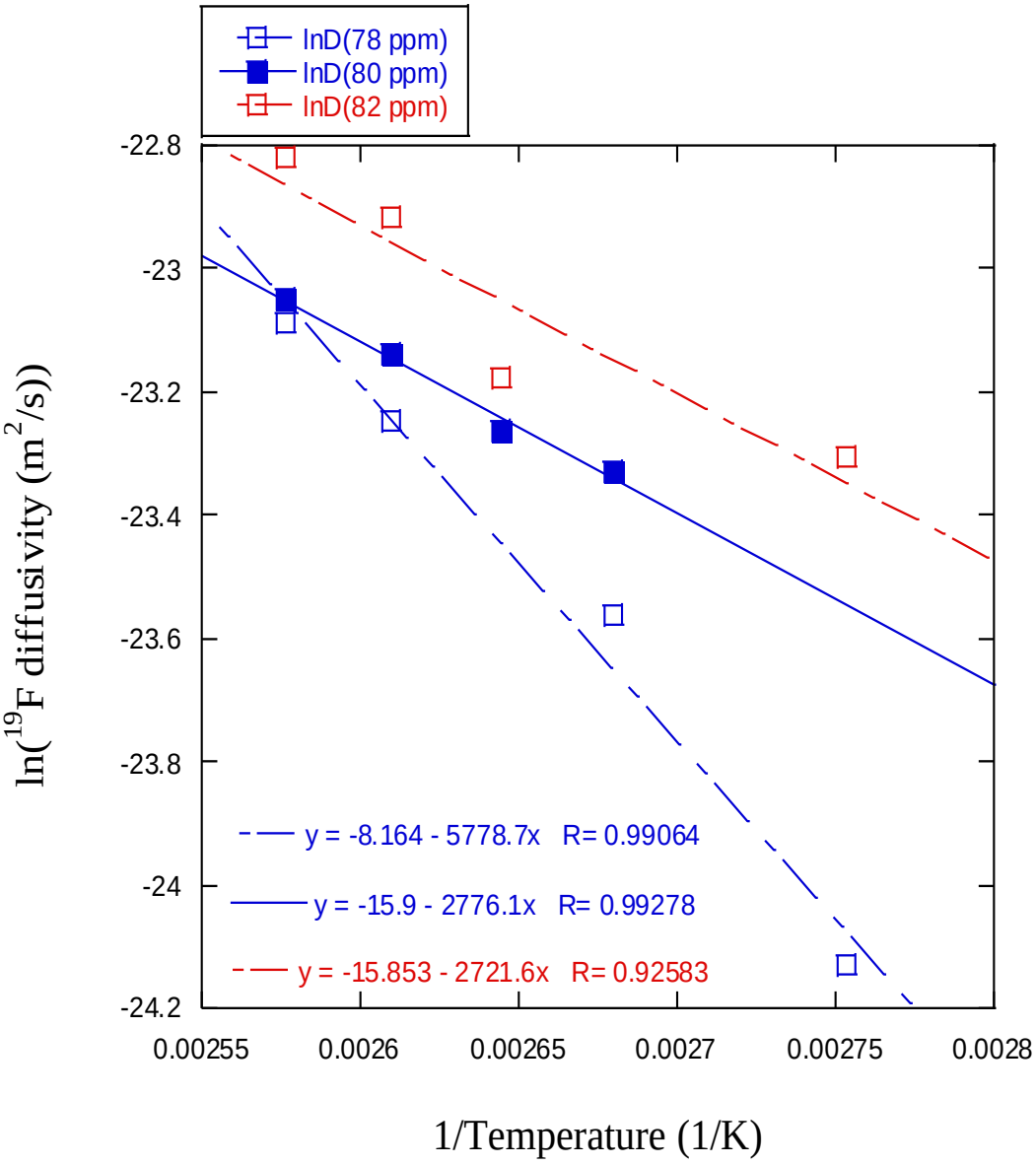

Figure 3.16 ln(Diffusivity) versus 1/Temperature for -78 ppm, -80 ppm and -82 ppm ^{19}F showing Arrhenius behavior from 90 to 115°C.

fluorines (Figure 3.16) are 48.0 ± 2.4 kj/mol, 23.1 ± 1.2 kj/mol and 22.6 ± 1.1 kj/mol respectively. Measured conductivity (Figure 3.17) shows Arrhenius behavior below and above the melting point with an activation energy for conduction above the melting point of 27.8 ± 1.4 kJ/mol.

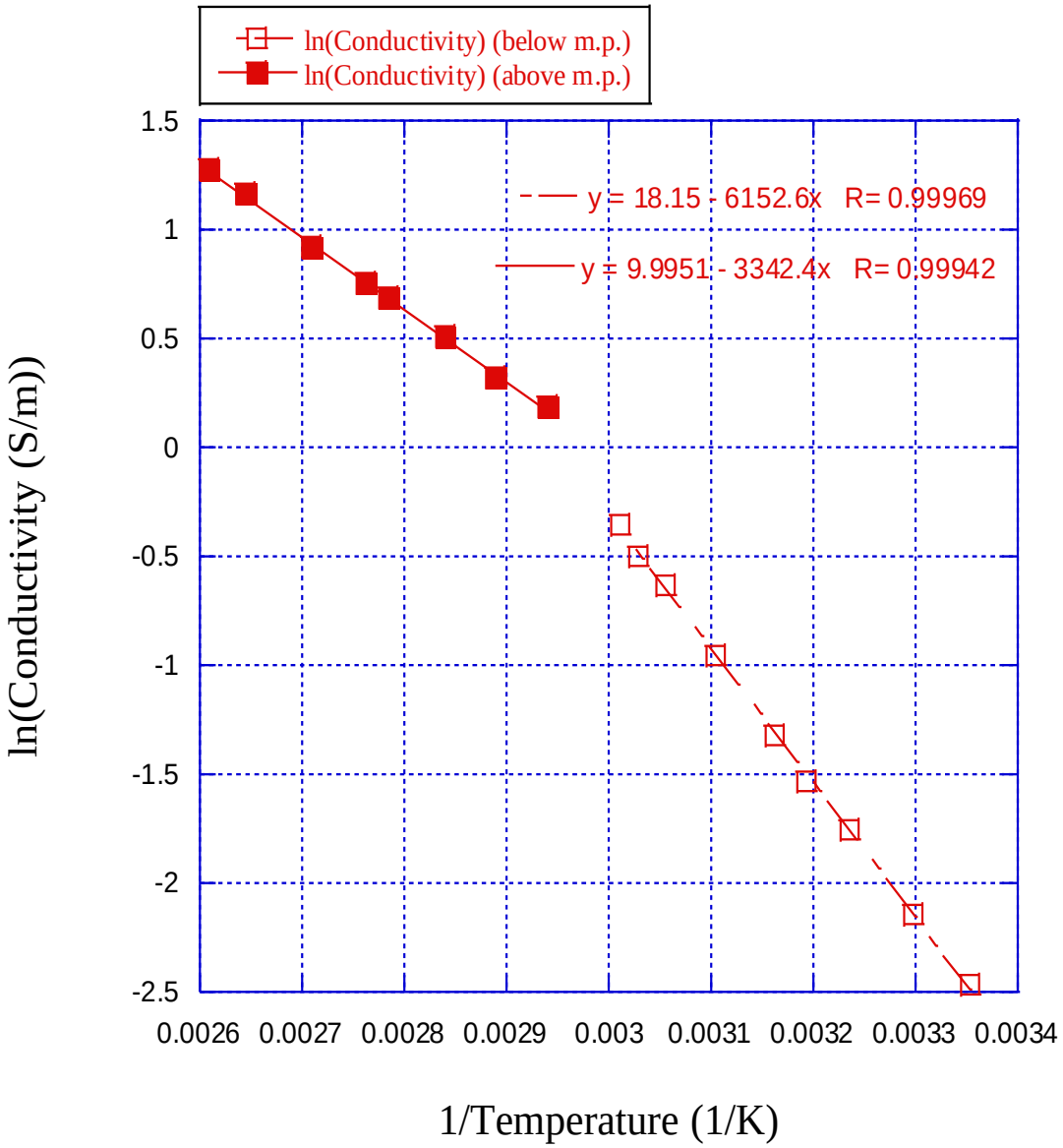

Figure 3.17 ln(Conductivity) versus 1/Temperature for 2-FPTf showing Arrhenius behavior from 25 to 110°C.

3.4.3 Degree of dissociation of the charged species

Use of the Nernst-Einstein equation, under conditions of zero concentration gradient and an applied electric field, leads to a relation between conductivity and diffusivity of a charged species in a solution, given by:

$$k_i = \frac{c_i D_i z_i^2 F^2}{RT}, \tag{3.11}$$

Where k_i is the conductivity of species *i* in S/m, c_i is the concentration of *i* in mol/m^3, D_i is the diffusion coefficient of *i* in m^2/s, z_i is the charge on ion *i*, F = 96485.3383 coulomb/mol is the Faraday constant, R is the gas constant, and T is the absolute temperature of the solution.

2-FPTf is highly ionic and has two primary charged species involved in proton motion, namely the (CF_3SO_3) and the protons. The molar concentrations of both species are nearly the same, and in the event of complete dissociation of the two, are equal to the density of the solution divided by its molar mass. The density, ρ of 2-FPTf was measured ain kg/m^3 and given its molar mass of 247.17x10^{-3} kg/mol, we have

$$c_{anion} = c_{proton} = \frac{\rho}{247.17 \times 10^{-3}} \text{ mol/m}^3, \tag{3.12}$$

Inserting the values of F and R in Eq. (3.11), and noting that $z_{anion} = -1$ and $z_{proton} = +1$, we get

$$k_{anion} = 4.5299 \times 10^9 \frac{D_{anion}\rho}{T} \text{ S/m}, \tag{3.13}$$

and

$$k_{proton} = 4.5299 \times 10^9 \frac{D_{proton}\rho}{T} \text{ S/m}, \tag{3.14}$$

therefore,

$$k_{net} = k_{anion} + k_{proton} = 4.5299 \times 10^9 \frac{\rho}{T}(D_{anion} + D_{proton}) \text{ S/m,} \quad (3.15)$$

When the two charged species are completely dissociated, the measured conductivity of the solution should equal to k_{net}. If there is some association, the associated pair's mobility is unaffected by the electric field, lowering the effective values of c_{anion} and c_{proton} in the solution and hence the net conductivity. The ratio of the measured conductivity of the solution, $k_{measured}$ to k_{net} calculated from the measured diffusion coefficients and the density gives the degree of dissociation of the two species at a particular temperature. Figure 3.18 shows the plots of k_{net} and $k_{measured}$ versus temperature from 85 to 115°C and Figure 3.19 shows the degree of dissociation (%) of the two ions over that temperature range. As seen in Figure 3.19, the degree of dissociation is around 13% at 85°C and increases with temperature to around 24% at 115°C.

3.4.4 Walden Plot

Figure 3.20 shows the position of 2-FPTf among other ionic liquids on the Walden plot (Thompson, 2010). As seen from the plot, 2-FPTf lies very near the ideal Walden line, and thus its good conductivity is not unexpected despite its relatively high viscosity.

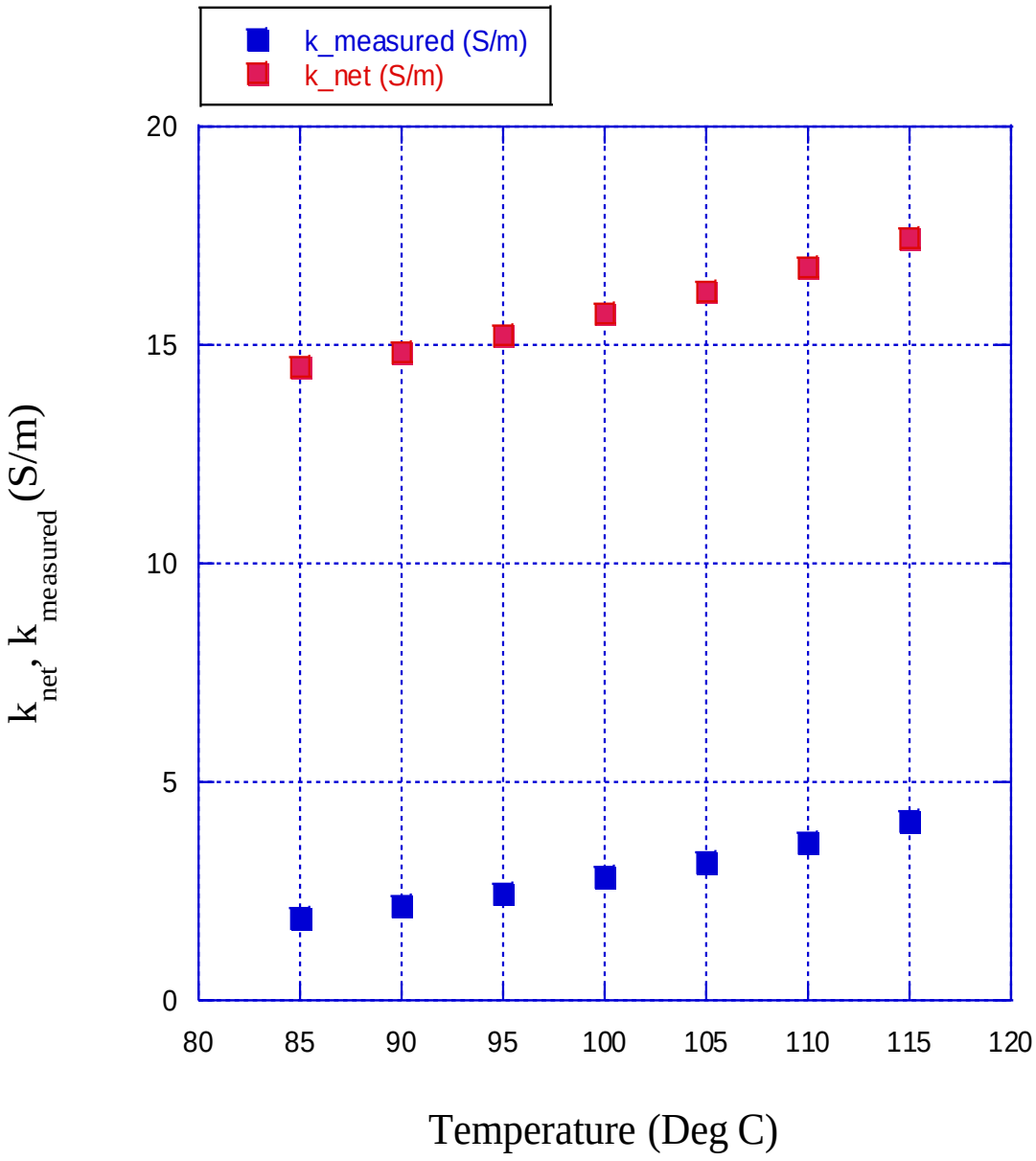

Figure 3.18 k_{net} and $k_{measured}$ for 2-FPTf from 85 to 115°C.

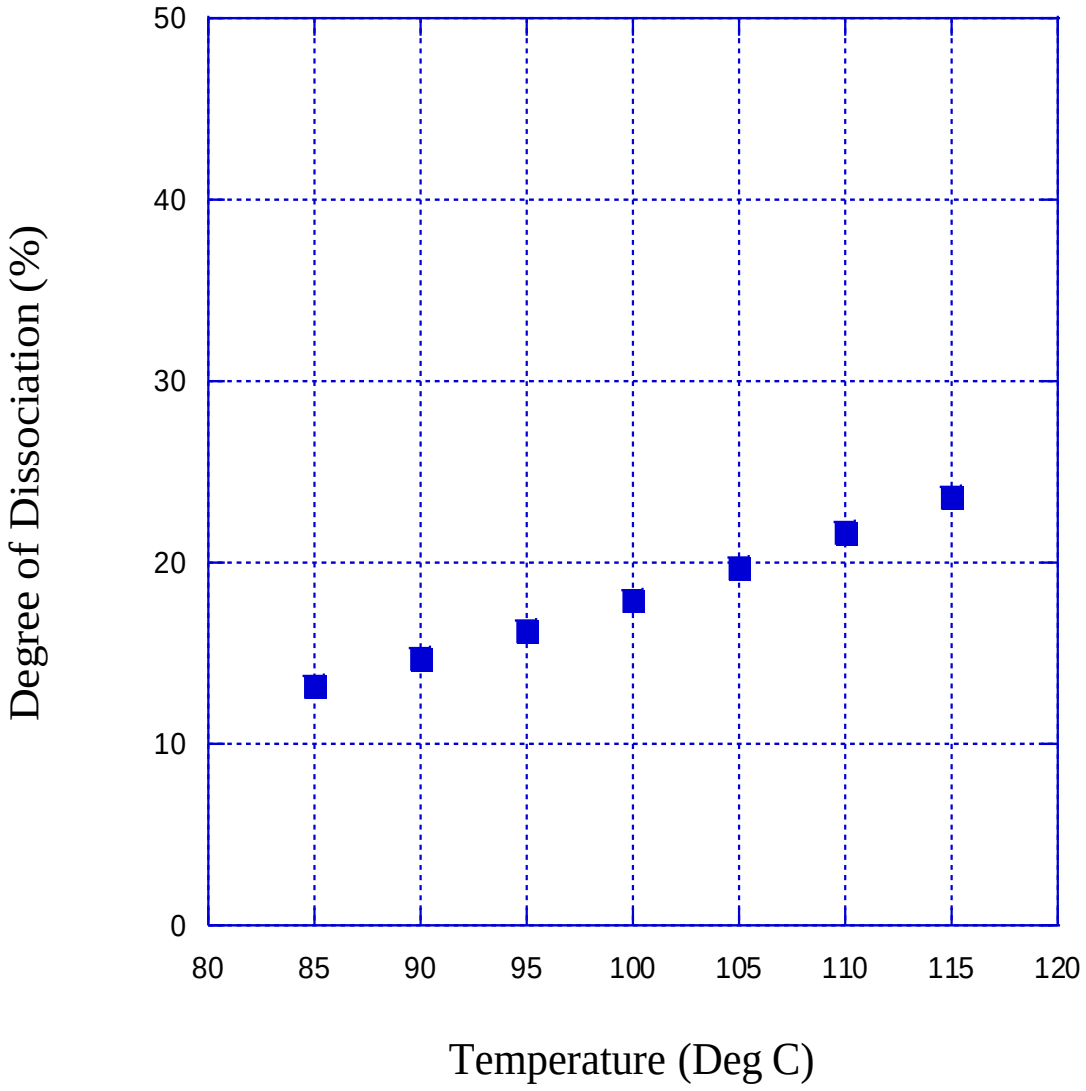

Figure 3.19 Degree of dissociation among charged species in 2-FPTf from 85 to 115°C.

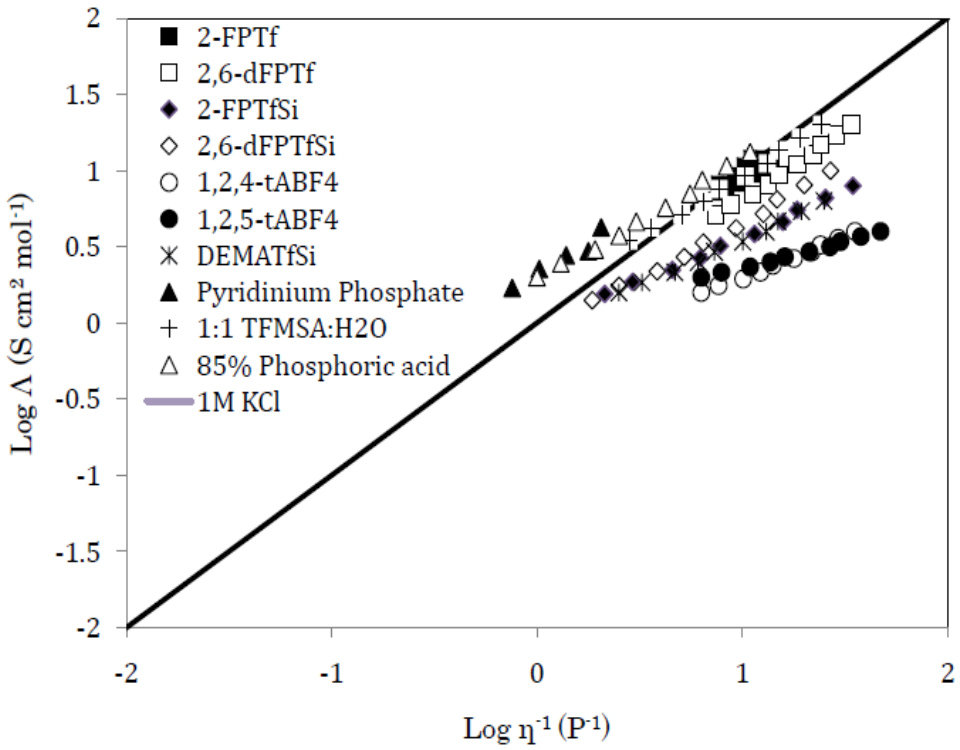

Figure 3.20 Walden plot for 2-FPTf and other ionic liquids

References

Abragam, A. *Principles of Nuclear Magnetism* (Oxford University Press, Oxford, 1978)

Adams, A., and Foley. R.T., *J. Electrochem. Soc.* 126, no. 5 (1979): 775-778.

Bard, A.J. and Faulkner, L. R., *Electrochemical Methods, Fundamentals and Applications*, 2nd ed. (John Wiley and Sons, New York, 2001), Chap. 10, pp. 368-416. Cole-Parmer Technical Library,

Holz, M. and Weingartner, H., *J. Magnetic Resonance* **92,** 115 -125 (1991). http://www.coleparmer.com/Techinfo/techinfo_home.asp.

Stejskal, E. O. and Tanner, J. E., *J. Chem. Phys.* **42**, 288 (1965).

Thomson, J.K., Dunn, P., Holmes, L., Belieres, J-P., Angell, C.A. and Gervasio,D. , *A Flourinated Ionic Liquid as a High-Performance Fuel Cell Electrolyte*, ECS Transactions, 13 (28), 21 (2008).

Thomson, Jeffery K. (2010). *Electrochemical Reduction in Ionic Liquids: Applications for Fuel Cells and Photovoltaics*

CHAPTER 4

TRANSPORT PROPERTIES OF TRIFLUOROMETHANESULFONIC ACID MONOHYDRATE

4.1 Introduction

We discussed in chapter 2, Ionic Liquid and Fuel Cells that protic ionic liquids are being investigated as proton conducting media for proton exchange membrane (PEM) fuel cells due to their protonic conductivity (Belieres *et all*, 2006). Currently, Nafion® (Figure 4.1, (a)) by DuPont is the most widely used proton conductor for PEM fuel cells. It is a perfluorinated synthetic polymer with ionic properties (an ionomer) and consists of a hydrophobic Teflon backbone with pendant side chains terminating with perfluoromethylsulfonic acid groups (-CF2SO3H) (Mauritz & Moore, 2004). These sulfonic acid functional groups are hydrophilic and preferentially hydrated. The Nafion membrane functions as both an electrode separator and an electrolyte in the fuel cell, because it is an electron insulator and, when properly hydrated, a proton conductor. The internal resistance and overall performance of the fuel cell are strongly influenced by the membrane's proton conductivity, which itself is a function of hydration (Springer *et al.*,1991). Extensive experimental measurement of the electro-osmotic drag coefficient (the number of water molecules carried across the membrane per proton transported) for various sulfonated membranes over a wide range of water content has suggested that the proton transport is dominated by sulfonic acid and water interactions (Zawodzinski *et al.*, 1995). A molecular level understanding of these complex processes in hydrated PEM's is a focus of highly active current fuel cell research.

We have studied the transport properties (diffusivity, conductivity, and viscosity) of trifluoromethanesulfonic acid monohydrate (abbreviated as TFMSA monohydrate or CF3SO3H:H2O, Figure 4.1, (b)). TFMSA monohydrate is very stable under the conditions of the study and is convenient for studying proton transport processes in hydrated sulfonic acid. TFMSA monohydrate can model many properties of hydrated Nafion, and our measurements can improve our understanding of the mechanism of proton conduction in Nafion. This is the first time, to our knowledge, that ionic diffusivities have been measured in the monohydrate.

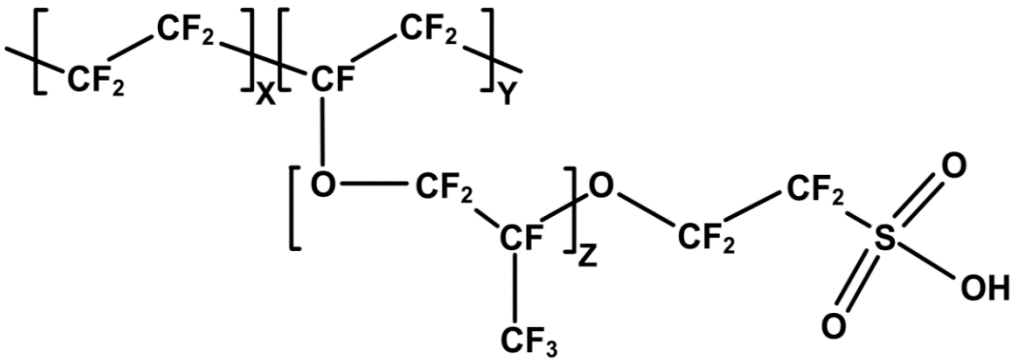

(a) Nafion

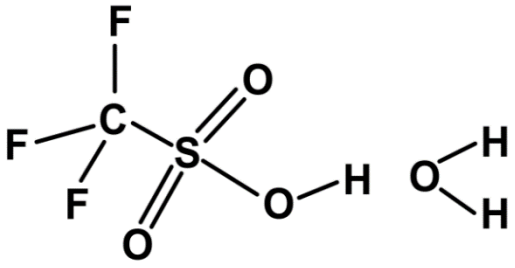

(b) Trifluoromethanesulfonic acid monohydrate

Figure 4.1 Schematic diagrams of Nafion and TFMSA monohydrate structures.

4.2 Experimental

4.2.1 Samples

The samples used were 0.5 molar fraction of trifluoromethanesulfonic acid (TFMSA) in water (CF_3SO_3H/H_2O). Commercially available 99% TFMSA from Alfa Aesar was distilled and then mixed with the necessary amount of deionized water (18 MΩ-cm) to produce the desired molar fraction. Being corrosive and very hygroscopic, the samples were stored tightly sealed in glass containers with Teflon caps.

4.2.2 Diffusivity Measurement

4.2.2.1 Proton NMR Spectra of TFMSA Monohydrate

A series of high resolution (500 MHz) ^{1}H and ^{19}F NMR spectra of TFMSA aqueous solutions was obtained in 2005 by C. Knobbe, working under the direction of D. Gervasio. The 1:1 TFMSA:H_2O (monohydrate) ^{1}H spectrum is shown in Figure 4.2. Two lines have been identified. By far the most intense is the ~11.6 ppm line, arising from the fully protonated TFMSA molecule. Another line is trace water at ~4.4 ppm. As discussed

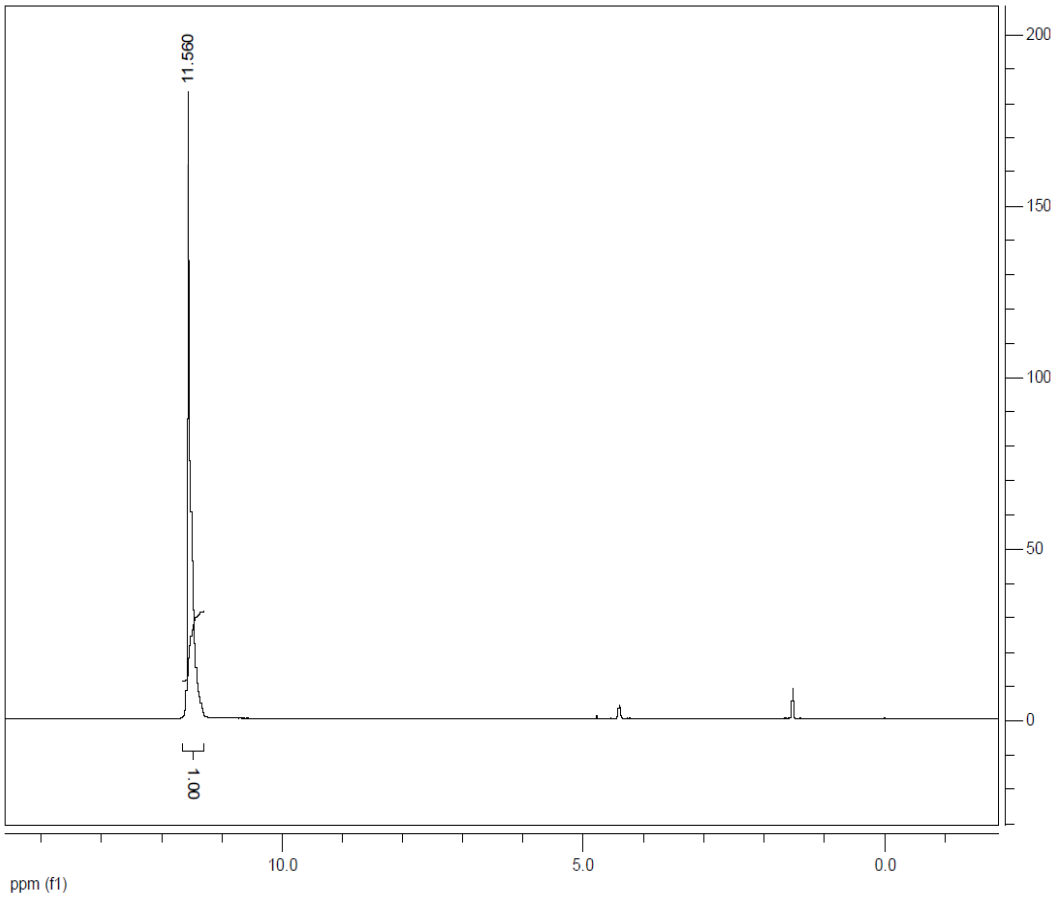

Figure 4.2 High resolution ^{1}H NMR spectra of TFMSA monohydrate[1]. The dominant line ~11.6 ppm is the TFMSA molecule. The ~4.4 ppm line is trace water, and the origin of the ~1.5 ppm line is under investigation. The origin of the third line is under investigation, but its small chemical shift at ~1.5 ppm indicates that the proton is well shielded, which is not expected to be the case for hydronium ion.

in more detail later, this spectrum strongly indicates that our measurements of diffusivity of protons in the monohydrate yield rates of proton movements from intact TFMSA molecule to intact molecule. These are thus rates for Grotthus-like proton "hopping", which can be compared with fluorine diffusivities. The latter measure the rates of "vehicle" diffusion, i.e., the Brownian motion of the monohydrate molecules.

[1] Obtained by C. Knobbe and kindly provided by D. Gervasio.

4.2.2.2 Procedure

Diffusivities for ^{1}H and ^{19}F were measured following the procedures described in chapter 3 Experimental section. Diffusivities were measured starting at 40°C up to 110°C at 10°C increments.

4.2.3 Conductivity Measurement

4.2.3.1 Equipment

Conductivity measurements were made by electrochemical impedance spectroscopy (EIS) using a Solartron 1250 Frequency Response Analyzer (FRA) and a Solartron 1286 Electrochemical Interface, which were operated by a PC running the ZPlot for Windows software package. The sample was held in a two-electrode cell, connected to two wires for applying voltage and two separate wires for passing current using the electrochemical interface. Temperature of the sample was controlled by placing the cell inside an electric oven containing a silicone oil bath. The temperature of the cell was assumed to be the same as the temperature measured in the oil bath. Two thermocouples and a glass thermometer were used for accurate temperature measurement. Complex impedance measurements were made about every 10°C starting from room temperature, 23°C up to 139°C. Three measurements were made at each temperature. These data were used to determine the conductivity of the solution using the procedure described in the results section.

4.2.3.2 Procedure

Electrical conductivities for TFMSA monohydrate were measured following the procedures described in chapter 3 Experimental section. Conductivities were measured starting at 40°C up to 110°C at 10°C increments.

4.2.4 Viscosity Measurement

4.2.4.1 Equipment

Viscosity measurements were made using a calibrated Cannon-Ubbelohde suspended level viscometer (Figure 4.3). It is a u-shaped piece of glassware with a reservoir on one side and a measuring bulb with a capillary on the other. Liquid is drawn into the bulb by suction, and then allowed to flow down through the capillary back into the reservoir. Two marks (one above and one below the bulb) indicate a known volume. The efflux time, the time taken for the liquid to pass between these marks is proportional its kinematic viscosity. This efflux time is measured for a sample and then multiplied by the viscometer constant (calibrated using liquids of known viscosity) to calculate the sample's kinematic viscosity. Capillary viscometers like the Cannon-Ubbelohde measure the kinematic viscosity directly because the head pressure is generated by the weight of the liquid. The dynamic/absolute viscosity of the sample at a certain temperature is determined by multiplying its kinematic viscosity with its density at that temperature. The Cannon-Ubbelohde viscometer is ideal for measuring kinematic viscosities of transparent Newtonian liquids. No kinetic energy corrections are required over the 0.5 to 10^5 mm^2/s range, and the viscometer constant remains the same at all temperatures. The particular viscometer (No. A606) used was a size 100 with viscometer constant 3.953×10^{-3} mm^2/s^2. For the range of kinematic viscosity measured and the range of temperature used in the experiment, the expanded uncertainty of the measurements at 95% confidence was 0.26%.

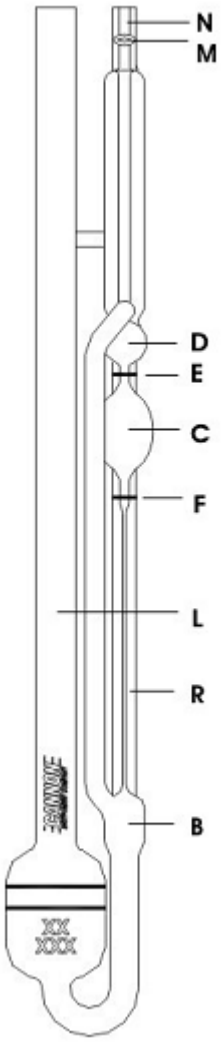

Figure 4.3 A Cannon-Ubbelohde viscometer. The efflux time, the time required for the meniscus of the sample to pass from mark E to mark F is multiplied by the viscometer constant to measure the sample's kinematic viscosity. The viscometer used in this study had the viscometer constant 3.953×10^{-3} mm^2/s^2.

Temperature was controlled by placing the viscometer with the sample inside an aluminum block holder heated by two 200 W heating cartridges symmetrically disposed. Current supply to the cartridges could be varied with a variable autotransformer. Two thermocouples were used to monitor the sample temperature.

4.2.4.2 Procedure

a. The viscometer was cleaned using acetone, methanol, and by passing clean, dry, and filtered nitrogen gas through it to remove the final traces of solvents.

b. The viscometer was charged by pouring about 25 ml of sample through tube L (see Figure 4.3), filling the lower reservoir so the liquid meniscus was halfway between the minimum and maximum fill lines marked on the reservoir. Plastic cartridges filled with Drierite (anhydrous calcium sulfate) were attached to tubes L, N, and M to remove any moisture from the air entering the instrument. A stopper was attached to tube M and a suction with a bypass valve was attached to tube N.

c. The viscometer was placed inside an aluminum heating block and was aligned vertically using a holder. One thermocouple was placed near the lower reservoir and another one close to bulb C. The temperature near the bulb was the temperature of the liquid when its viscosity was measured.

d. The heating block's temperature was increased by about 10°C starting from around 45°C. Approximately 60 minutes were allowed for the block and the sample to stabilize to the target temperature. A temperature difference of about 15°C was observed between the lower reservoir and the liquid in bulb C.

e. The branching vent tube M was sealed with a stopper and suction was applied to tube N until the liquid reached the center of bulb D. Suction was removed from tube N. The seal was removed from tube M, and immediately tube N was sealed until the sample dropped away from the lower end of the capillary R into bulb B. The seal was then removed and the efflux time was measured.

f. To measure the efflux time, the liquid sample was allowed to flow freely down past mark E. The time for the meniscus to pass from mark E to mark F was measured to the nearest 0.1 to 0.01 second.

g. The kinematic viscosity of the sample was calculated by multiplying the efflux time by the viscometer constant.

h. Finally, the dynamic/absolute viscosity was measured by multiplying the kinematic viscosity with the density of the solution. The method used to measure density is described in the following section.

4.2.5 Density Measurement

4.2.5.1 Equipment

Density measurements were made using a 2.0 ml Pyrex® precision volumetric flask with a Pyrex stopper. The class A flask had a tolerance of ± 0.015 ml. The sample of TFMSA monohydrate was the same as the one used for the viscosity measurement. The sample was heated using an aluminum heating block on a hot plate while the temperature was monitored with a glass thermometer. The experiment was done under a fume hood for safety.

4.2.5.2 Procedure

a. The volumetric flask was cleaned using acetone, methanol, and by passing clean, dry filtered nitrogen gas through it to remove the final traces of solvents. It was then placed vertically inside a beaker on a precision analytical balance. The balance was then zeroed.

b. The volumetric flask was carefully filled with the sample just above the 2.0 ml mark using a glass pipette. Care was taken so that the inside surface of the flask above the

meniscus was not wet with any excess liquid. The glass stopper was then replaced on the flask.

c. The volumetric flask was placed inside one of the holes of an aluminum heating block which was kept on a hot plate under a fume hood. A glass thermometer was placed right next to the flask.

d. The heating block's temperature was increased to around 45°C. About 30 minutes were allowed for the block and the sample to stabilize to the target temperature.

e. The glass stopper was removed and excess sample was taken out very carefully with a glass pipette until the lowest point on the meniscus of the liquid was tangent to the plane passing through the top edge of the mark. The bottom of the meniscus was taken to be the interface of the liquid and the air. The flask was resealed with the glass stopper.

f. The volumetric flask was weighed on the balance zeroed earlier giving the mass of 2.0 ml of the sample at the temperature to which it was heated. The density at that temperature was calculated by dividing the mass by the volume.

g. Densities at higher temperatures were measured by successively heating the sample and following the procedures described in steps e and f.

4.3 Results

4.3.1 Diffusivities

The Stejskal-Tanner plots from ^{1}H and ^{19}F diffusivity measurements are shown in Figure 4.4 and Figure 4.5 respectively. From the slopes of the linear fits, the diffusivities of ^{1}H and ^{19}F were calculated using Equation (3.3). The gradient constant, k for our diffusion probe was measured using known self-diffusion coefficient value of water (Holz &

Weingartner, 1991) at 25°C and was found to be 14.1 T/m. The nuclear gyromagnetic ratio, γ for ^{1}H is 2.67×10^{8} /T.s and that for ^{19}F is 2.51×10^{8} /T.s. The width of the gradient pulse, δ was 1.0 ms for both ^{1}H and ^{19}F and the time between the gradient pulses, Δ was 20.0 ms for ^{1}H and 40.0 ms for ^{19}F. Table 4.1 lists the slopes of the Stejskal-Tanner plots and the diffusivities for ^{1}H and ^{19}F from 40 to 110°C. As we can see from Table 4.1, the diffusivity of protons increased from $(7.67\pm0.23)\times10^{-11}$ m^2/s at 40°C to $(3.92\pm0.12)\times10^{-10}$ m^2/s at 110°C and the diffusivity of fluorines increased from $(4.63\pm0.14)\times10^{-11}$ m^2/s at 40°C to $(2.79\pm0.08)\times10^{-10}$ m^2/s at 110°C. Figure 4.6 shows the temperature-dependent behavior of the ^{1}H and ^{19}F diffusivities over the observed temperature range.

4.3.2 Conductivity

The cell constant of the electrochemical cell was determined using known conductivities (Cole-Parmer Technical Library) of 0.1, 0.3, and 1.0% weight NaCl aqueous solutions at 25°C. The Nyquist plots from EIS in the high frequency region are shown in Figure 4.7. The real axis intercepts of the plots gave the cell resistances for the three concentrations. The cell constants were calculated from the three cell resistances using Eq. (3.8). The average cell constant for our electrochemical cell was 24.1 /cm. The results from the cell constant measurement are listed in Table 4.2.

Figure 4.8 shows the Nyquist plots (in the high frequency region) and Figure 4.9 the Bode plots of TFMSA monohydrate from 23 to 139°C. The cell constant and the cell resistances from the real axis intercepts of the Nyquist plots were used to find the conductivity of the solution over that temperature range. The conductivity of the solution increased from 6.60 ± 0.2 mS/cm at 23°C to 84.6 ± 2.5 mS/cm at 139°C. Table 4.3 lists

the results from the conductivity measurement. Barthel *et al.* (Barthel *et al,.* 1999) have measured the temperature-dependent conductivity, viscosity, and density of TFMSA monohydrate from 36 to 135°C. Our temperature-dependent conductivity values agree very well with their findings (Figure 4.10).

4.3.3 Viscosity

Results from the viscosity measurement are listed in Table 4.4. The efflux time at an observed temperature was multiplied by the viscometer constant (3.953×10^{-3} mm^2/s^2) to get the kinematic viscosity at that temperature. Dynamic/absolute viscosity was found by multiplying the kinematic viscosity with the density of the solution at that temperature. Interpolated values from the density measurement, as discussed in the following section, were used to calculate the dynamic viscosity which decreased from 27.5 ± 1.4 mPa·s at 49°C to 4.38 ± 0.22 mPa·s at 121.5°C. Temperature-dependent kinematic and dynamic viscosities from this study agree well with those from Barthel *et al.* (Barthel *et al.* 1999), as shown in Figure 4.11 and Figure 4.12 respectively.

4.3.4 Density

Table 4.5 lists the mass of 2.0 ml TFMSA monohydrate at different temperatures from which its density at those temperatures were calculated. Density measurements were possible at only 5 temperature points since the sample had to be heated by around 20°C increments for enough volume expansion to occur beyond the 2.0 ml mark to be removed by a glass pipette with acceptable accuracy. Densities at intermediate temperatures were interpolated from a linear fit through those 5 points. A comparison with temperature-dependent density from Barthel *et al.* (Barthel *et al.* 1999) is shown in Figure 4.13.

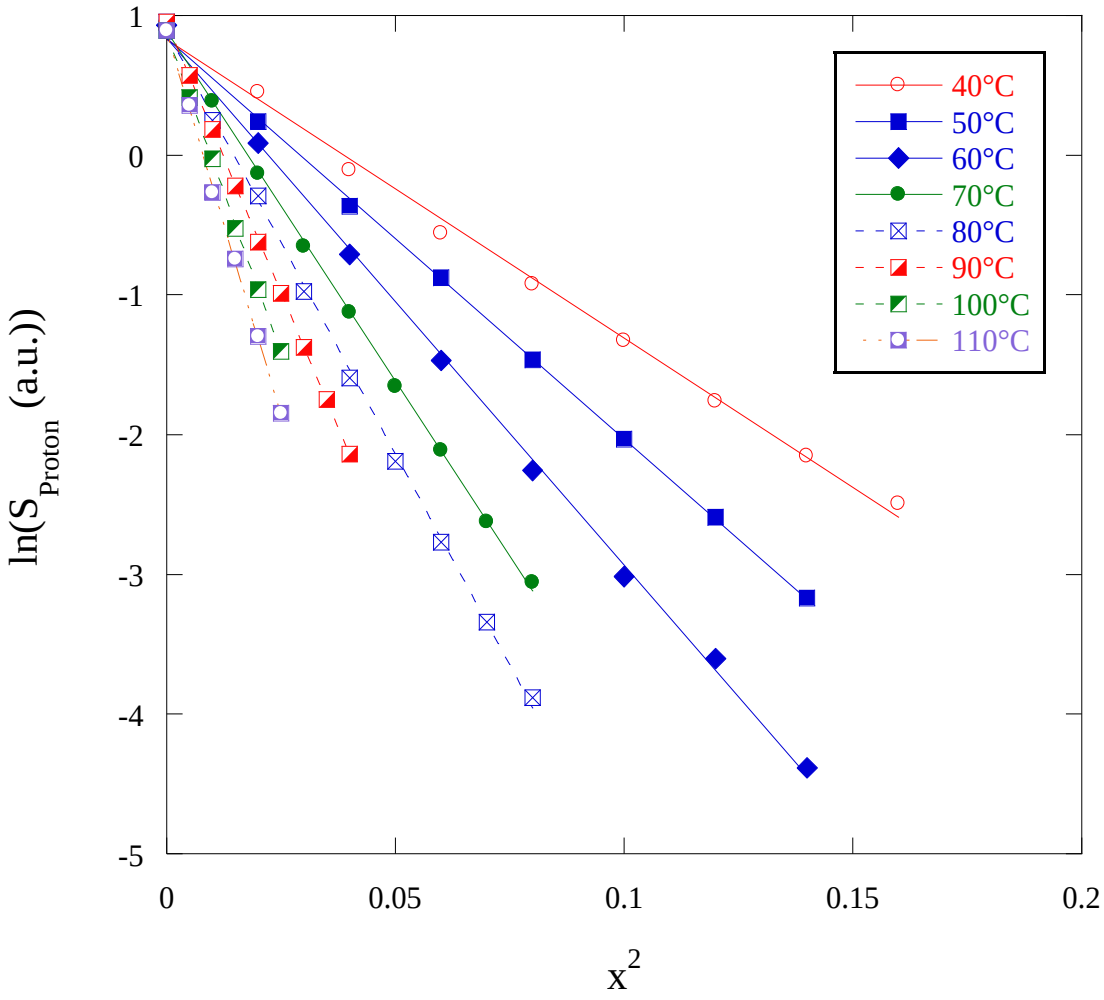

Figure 4.4 Stejskal-Tanner plots from ^{1}H diffusivity measurements. The square of the amplitude of the gradient pulse, x is plotted along the X axis and the natural log of the normalized intensity of the spin-echo signal, S_{Proton} is plotted along the Y axis.

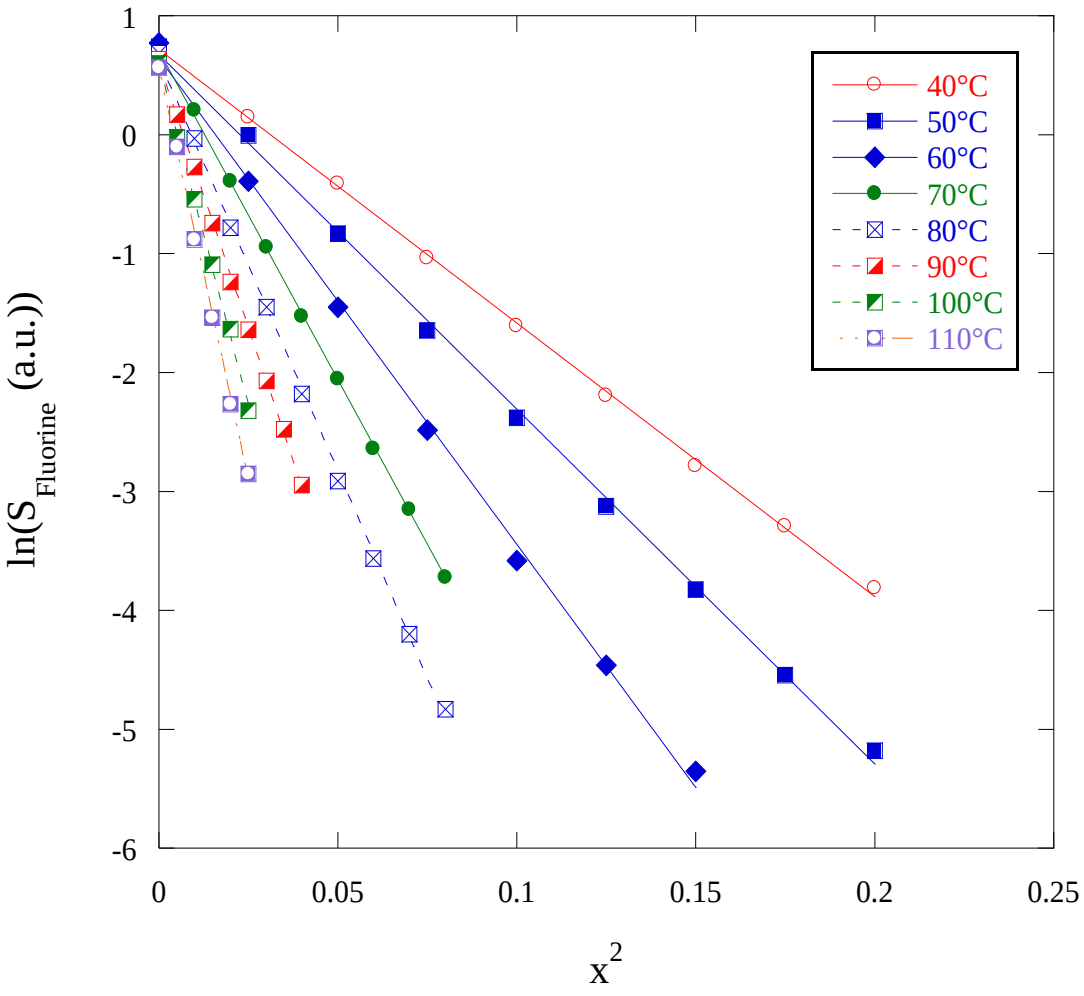

Figure 4.5 Stejskal-Tanner plots from ^{19}F diffusivity measurements. The square of the amplitude of the gradient pulse, x is plotted along the X axis and the natural log of the normalized intensity of the spin-echo signal, $S_{Fluorine}$ is plotted along the Y axis.

Table 4.1: ^{1}H and ^{19}F diffusivity of TFMSA monohydrate from 40 to 110°C.

Temperature (°C)	Slope for ^{1}H	^{1}H Diffusivity (m^2/s)	Slope for ^{19}F	^{19}F Diffusivity (m^2/s)	$^{1}H/^{19}F$
40	-21.367	7.67×10^{-11}	-22.993	4.63×10^{-11}	1.65
50	-28.687	1.03×10^{-10}	-29.824	6.00×10^{-11}	1.71
60	-37.720	1.35×10^{-10}	-40.906	8.23×10^{-11}	1.64
70	-50.040	1.80×10^{-10}	-55.341	1.11×10^{-10}	1.61
80	-60.492	2.17×10^{-10}	-69.353	1.40×10^{-10}	1.55
90	-77.367	2.78×10^{-10}	-89.215	1.80×10^{-10}	1.55
100	-92.049	3.30×10^{-10}	-114.19	2.30×10^{-10}	1.44
110	-109.34	3.92×10^{-10}	-138.59	2.79×10^{-10}	1.41

[a] ± 3% error in all diffusivity measurements.

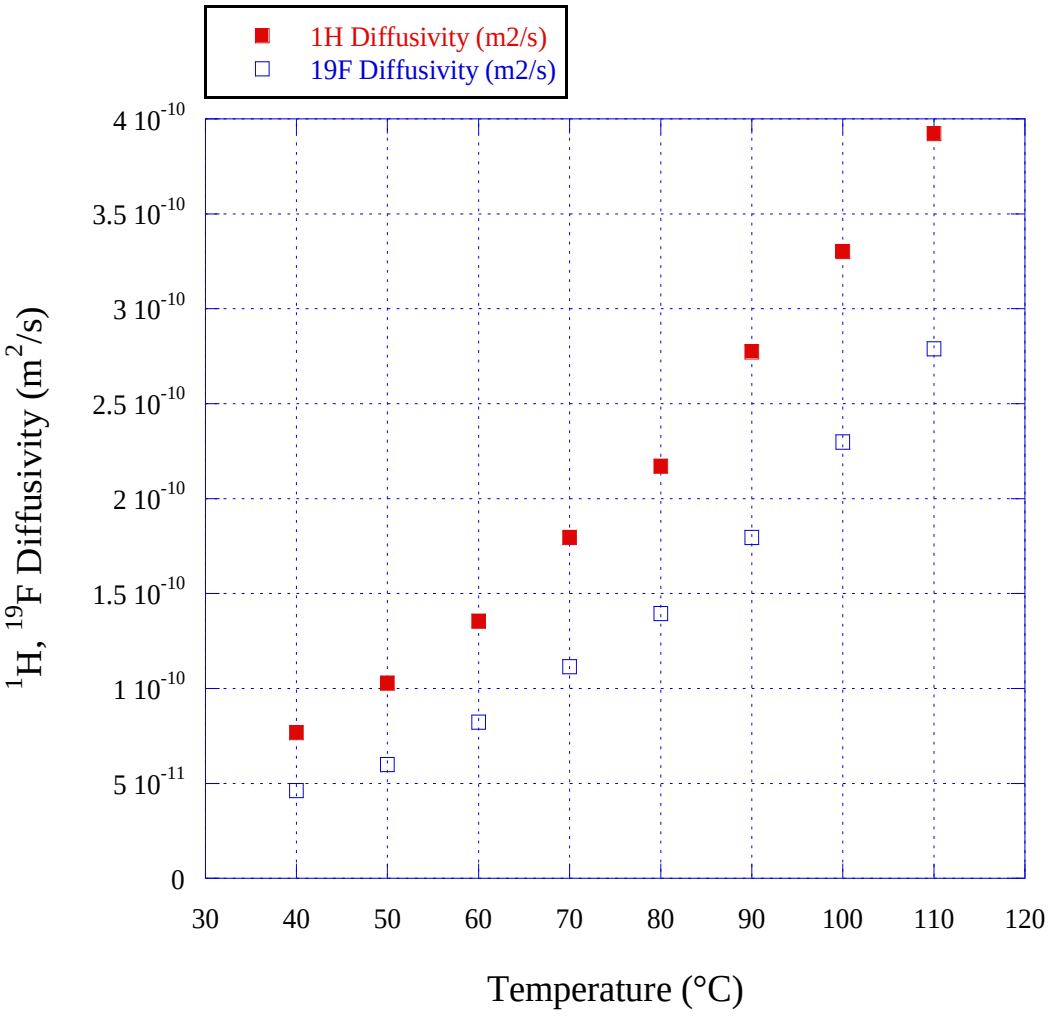

Figure 4.6 ^{1}H and ^{19}F diffusivity of TFMSA monohydrate from 40 to 110°C.

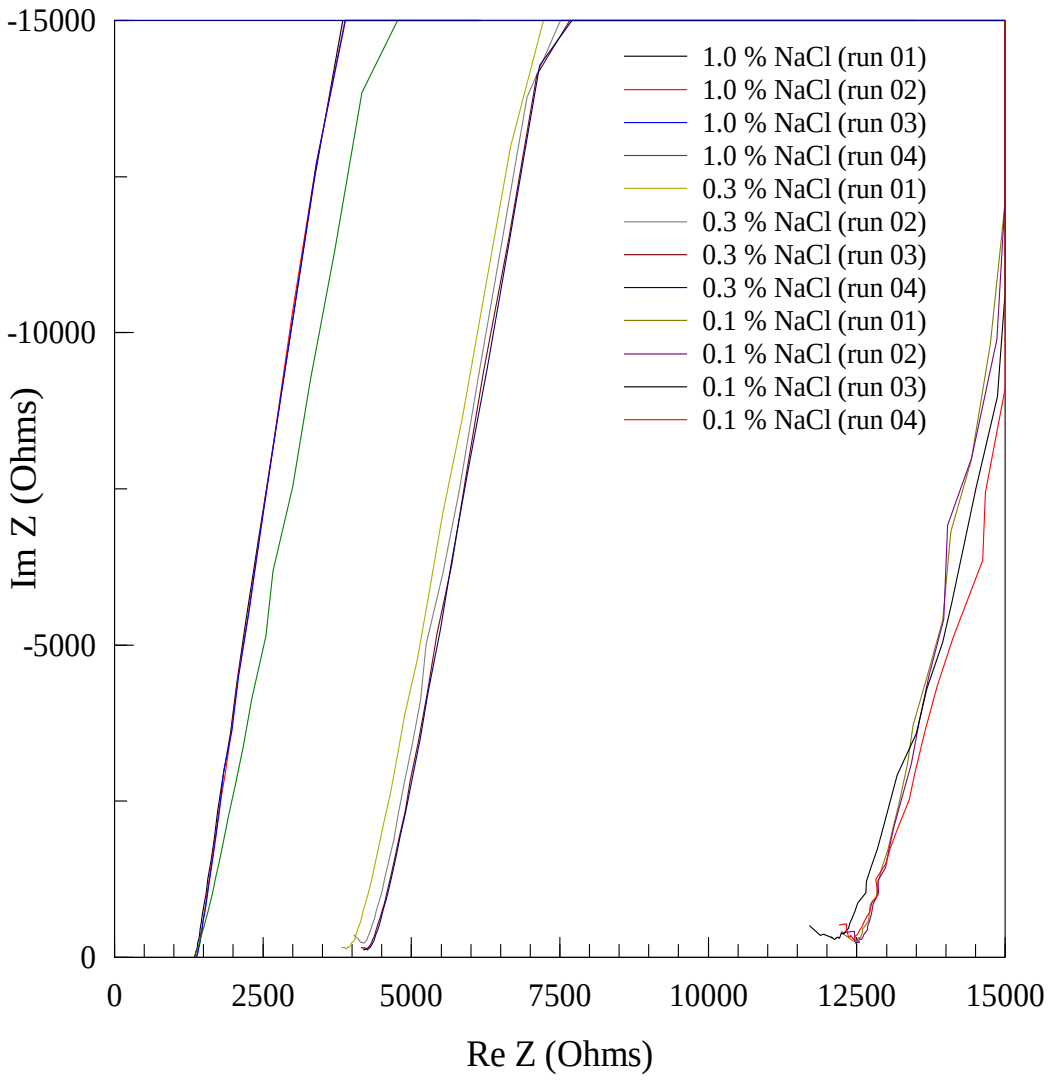

Figure 4.7 Nyquist plots of 0.1, 0.3, and 1.0% weight NaCl aqueous solutions at 25°C in the high frequency region. The real axis intercept of the plot gives the cell resistance.

Table 4.2: Cell constant from known conductivities of standard NaCl aqueous solutions.

NaCl Concentration (% Weight)	NaCl Conductivity[a] (mS/cm)	Cell Resistance (Ohms)	Cell Constant (1/cm)
0.1%	1.99	12250	24.378
0.3%	5.69	4200	23.898
1.0%	17.6	1365	24.024
			24.1 (average)

[a]Cole-Parmer Technical Library.

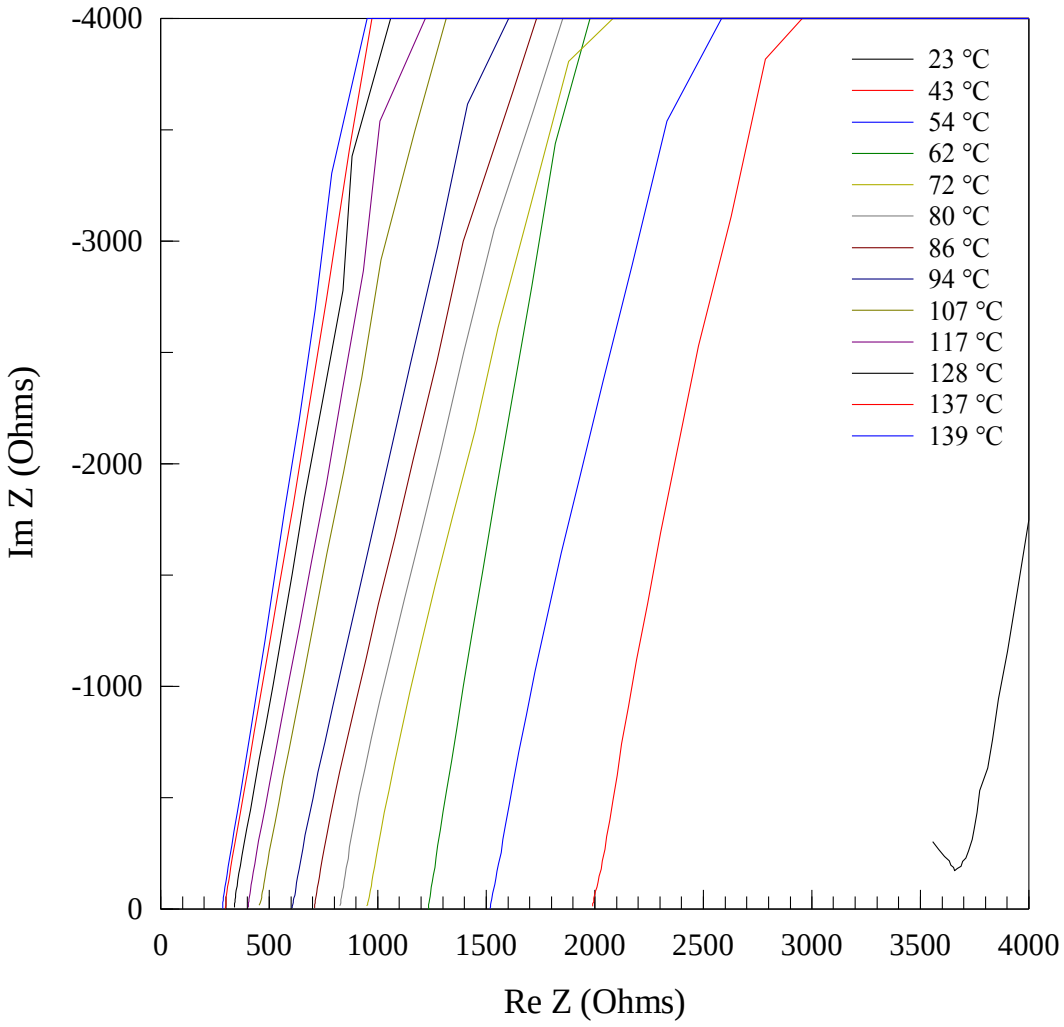

Figure 4.8 Nyquist plots of TFMSA monohydrate from 23 to 139°C in the high frequency region. The real axis intercept of the plot gives the cell resistance.

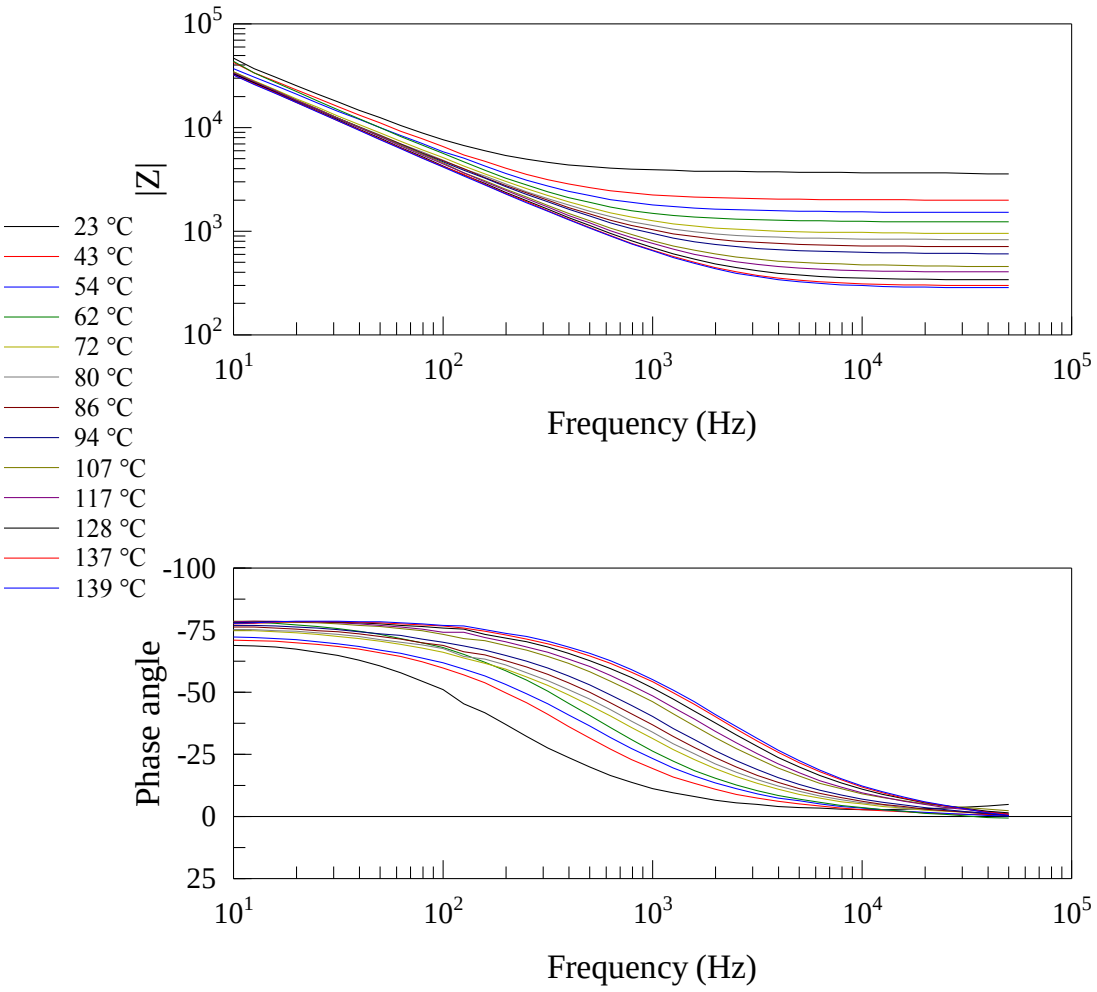

Figure 4.9 Bode plots of TFMSA monohydrate from 23 to 139°C.

Table 4.3: Conductivity of TFMSA monohydrate.

Temperature (°C)	Cell Resistance (Ohms)	Conductivity[a] (mS/cm)
23	3650	6.60
43	1975	12.2
54	1510	16.0
62	1175	20.5
72	950	25.4
80	800	30.1
86	705	34.2
94	610	39.5
107	455	53.0
117	400	60.3
128	340	70.9
137	295	81.7
139	285	84.6

[a] ± 3% error in all conductivity measurements.

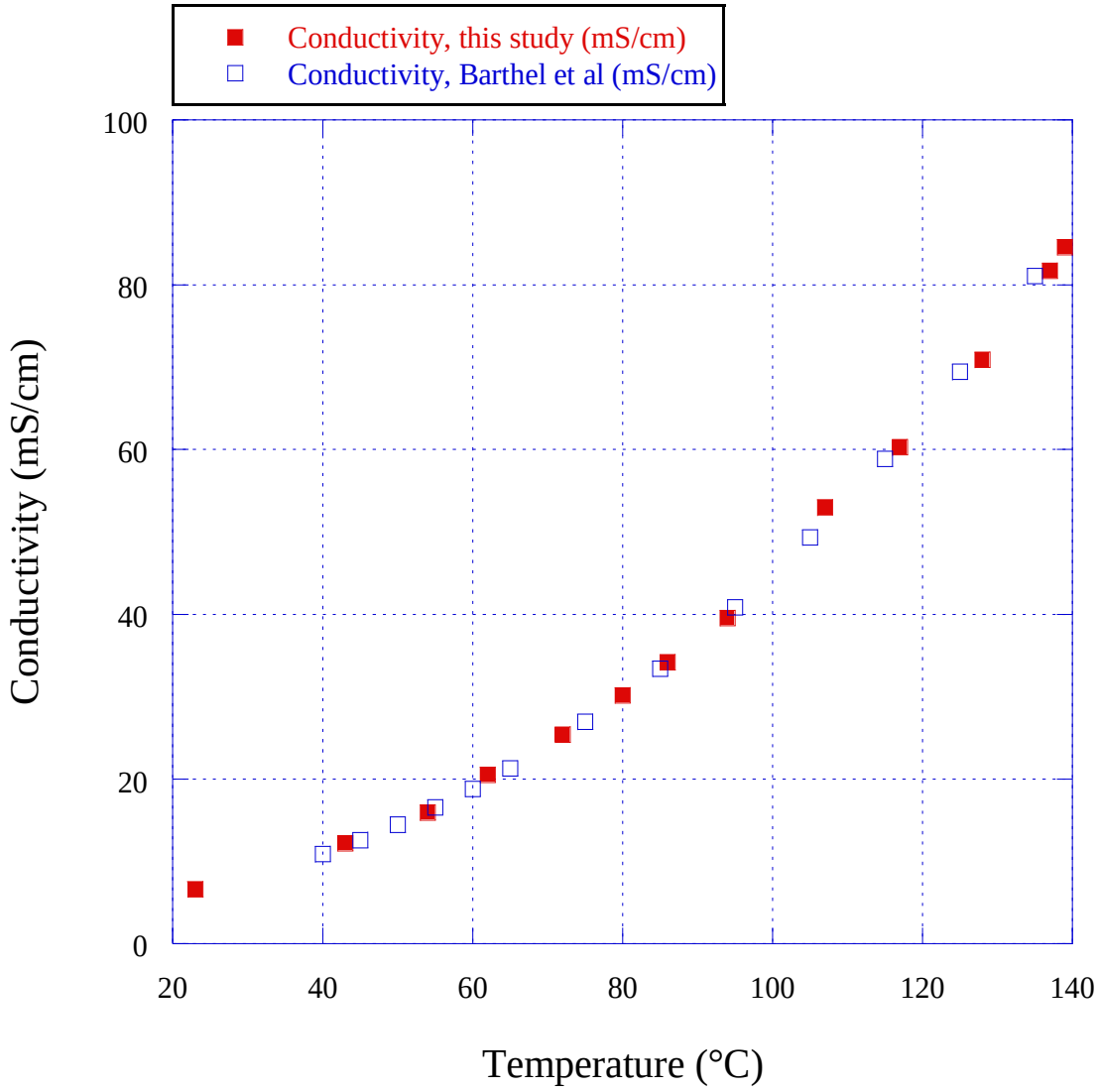

Figure 4.10 Temperature-dependent conductivity of TFMSA monohydrate from this study and its comparison with literature values.

Table 4.4: Kinematic and dynamic viscosity[a] of TFMSA monohydrate.

Temperature (°C)	Efflux Time (s)	Kinematic Viscosity (mm^2/s)	Dynamic Viscosity (mPa·s)
49	4197.3	16.6	27.5
57	3294.2	13.0	21.5
67.5	2440.1	9.65	15.8
80	1783.1	7.05	11.4
89	1416.2	5.60	9.02
104	1033.9	4.09	6.51
121.5	705.10	2.79	4.38

[a] ± 5% error in all viscosity measurements.

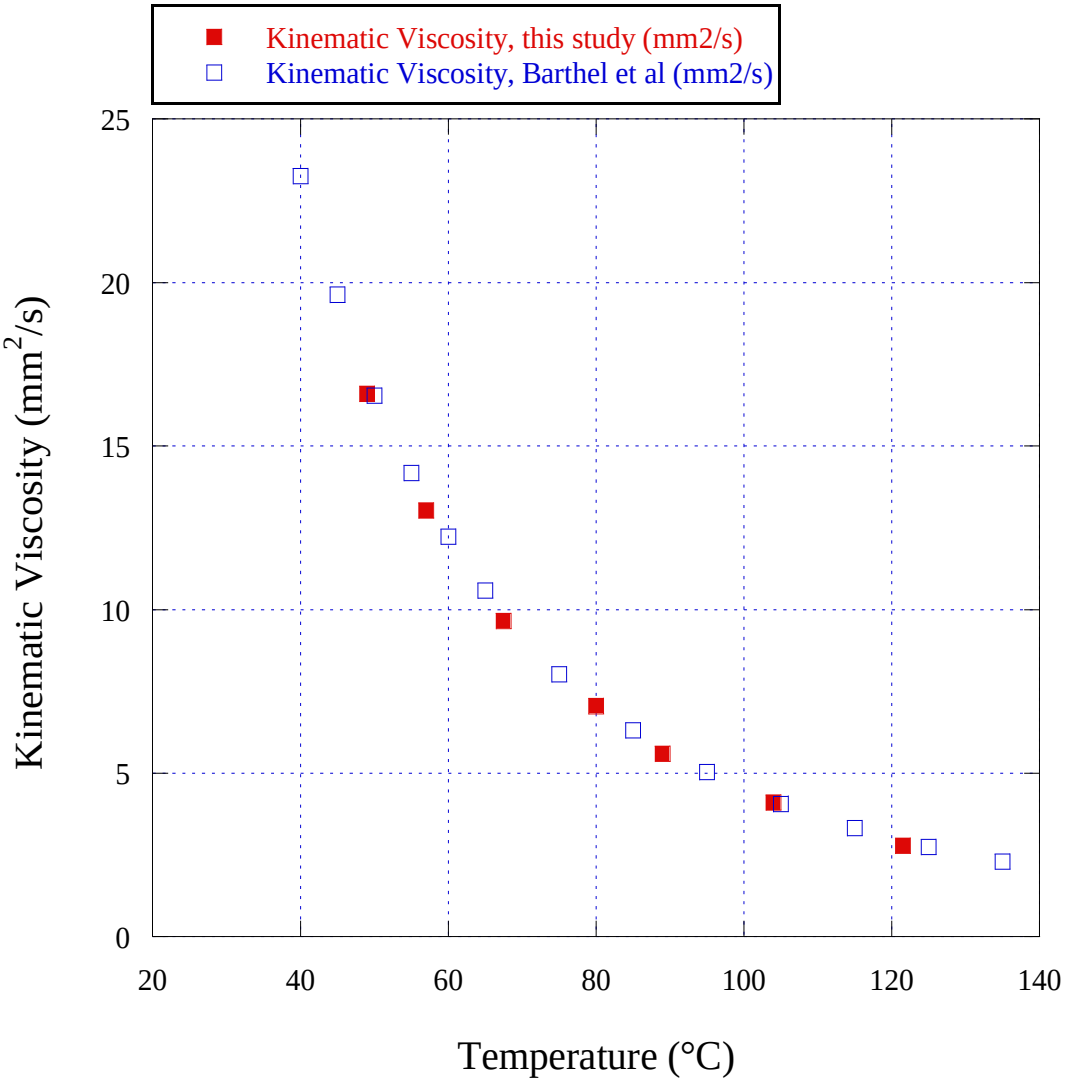

Figure 4.11 Temperature-dependent kinematic viscosity of TFMSA monohydrate from this study and its comparison with literature values.

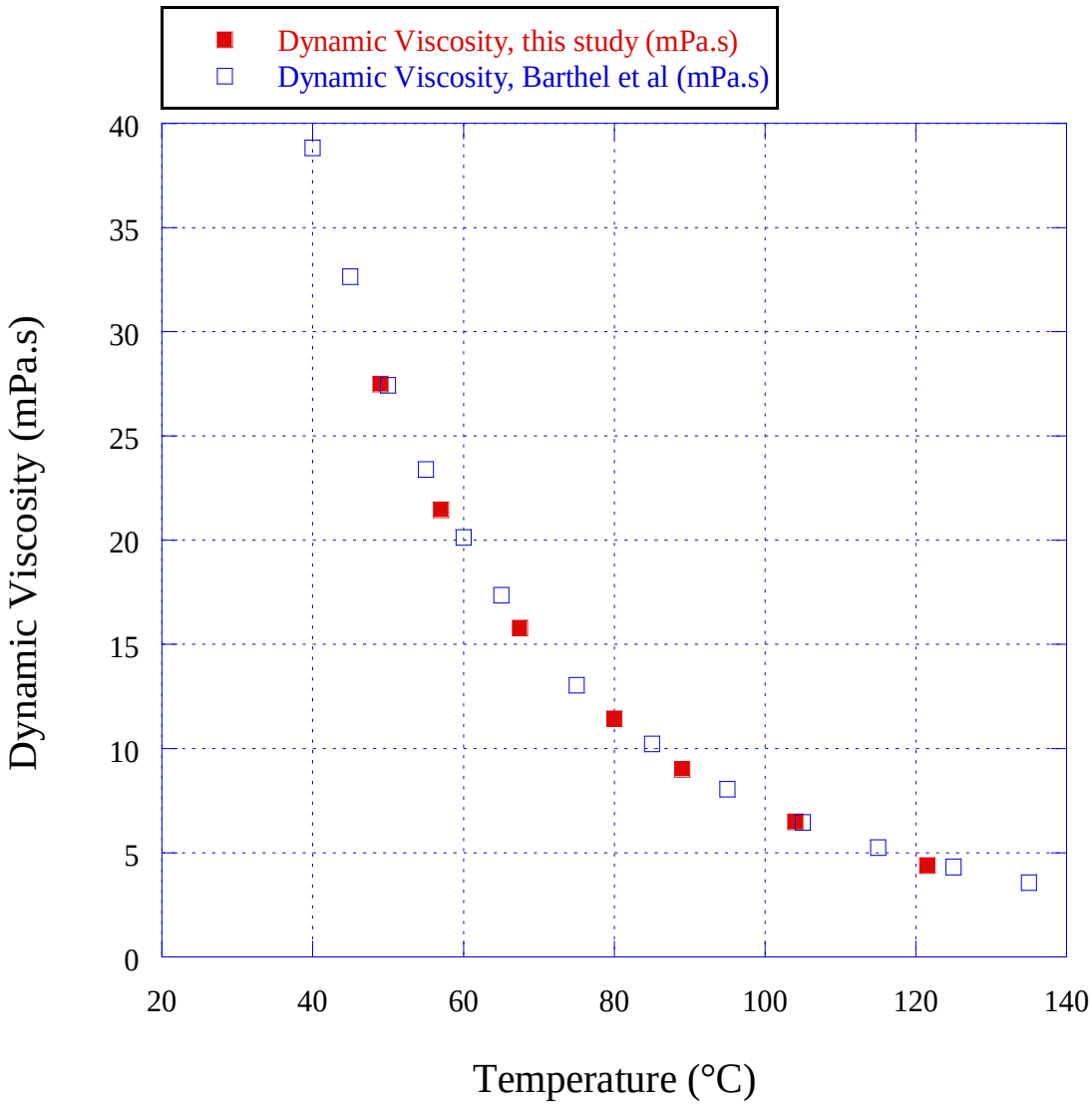

Figure 4.12 Temperature-dependent dynamic viscosity of TFMSA monohydrate from this study and its comparison with literature values.

Table 4.5: Density of TFMSA monohydrate.

Temperature (°C)	Mass of 2.0 ml Sample (g)	Density[a] (kg/m^3)
43	3.3328	1666.4
60	3.2868	1643.4
85	3.2248	1612.4
106	3.1901	1595.0
135	3.1085	1554.3

[a] ± 0.5% error in all density measurements.

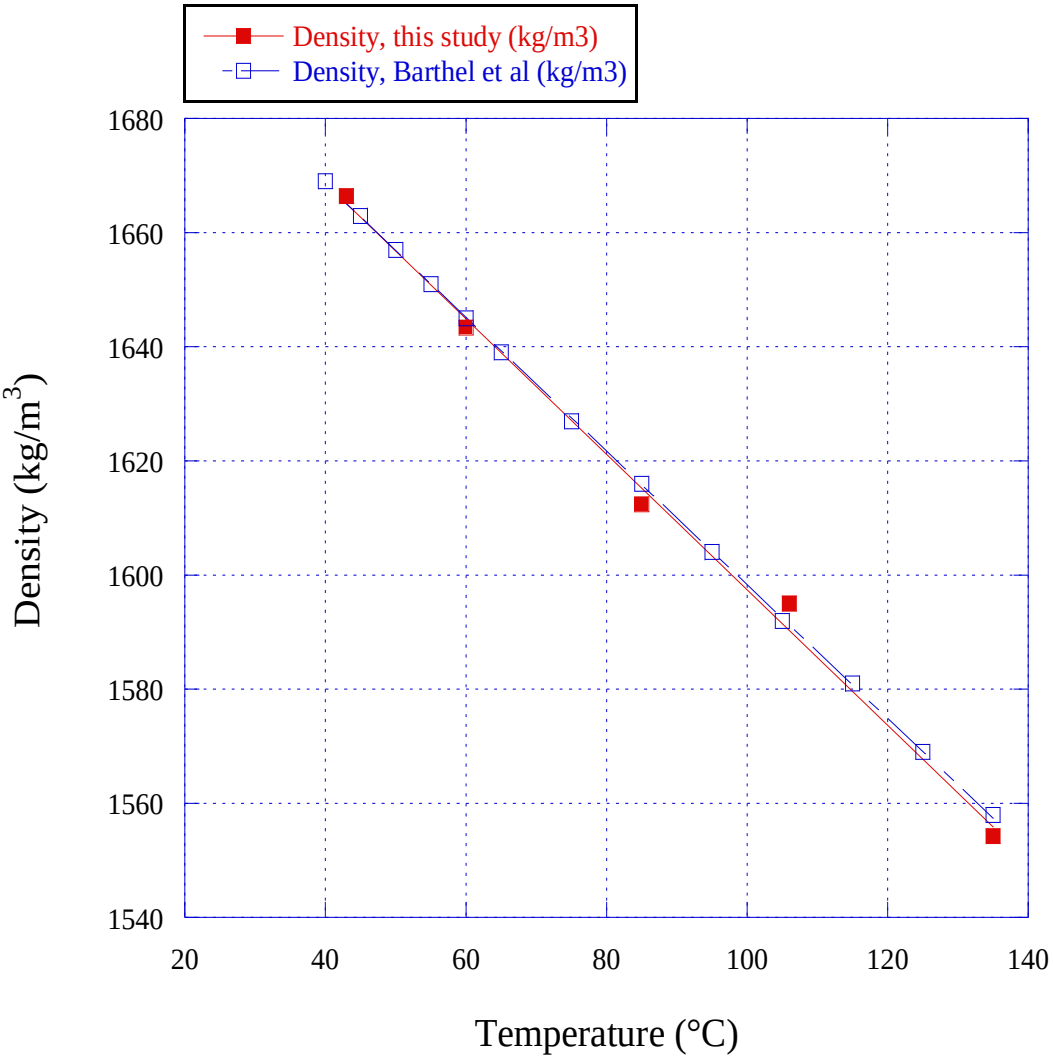

Figure 4.13 Temperature-dependent density of TFMSA monohydrate from this study and its comparison with literature values. Interpolated value of density from a linear fit was used to calculate the dynamic viscosity.

4.4 Discussion

4.4.1 Proton versus fluorine diffusivity

In the high resolution ^{1}H NMR spectra (Figure 4.2) we see a dominant single line at ~11.6 ppm which is identified with the fully protonated molecule of TFMSA, i.e., the proton bound to the triflate anion. Diffusivity measurements made on this line show proton diffusion occurring approximately 1.5 times faster than that of fluorine (triflate anion) over the observed temperature range from 40C to 110°C (Table 4.1 and Figure 4.14). In neat TFMSA, where there is no water present, protons and triflate anions diffuse at the same rate (Marzke *et al.*, unpublished data). This means that, in TFMSA monohydrate, proton motion occurs via hopping from TFMSA molecule to molecule. Water plays no apparent role in this motion, since only a very weak signal at ~4.4 ppm is attributed to water in the ^{1}H NMR spectrum, far from the main line. Thus, this proton motion may be called “dry” hopping.

4.4.2 Activation energies

Figure 4.15 shows $\ln D$ versus $1/T$ plots for proton and fluorine from 40 to 110°C. As seen from the plots, diffusivities of both proton and fluorine demonstrate Arrhenius behavior over the entire temperature range, implying that the mechanisms of diffusion for both species remain unchanged with temperature. From the slopes of the two lines we find the activation energies for proton and fluorine to be 23.4 ± 1.2 kJ/mol and 26.0 ± 1.3 kJ/mol respectively. This is a small difference in activation energies, but a substantial difference exists in their diffusivities, as pointed out previously. Similar Arrhenius behavior is observed in the measured conductivity

(Figure 4.16) and viscosity (Figure 4.17) with an activation energy for conduction of 22.1 $\pm$ 1.1

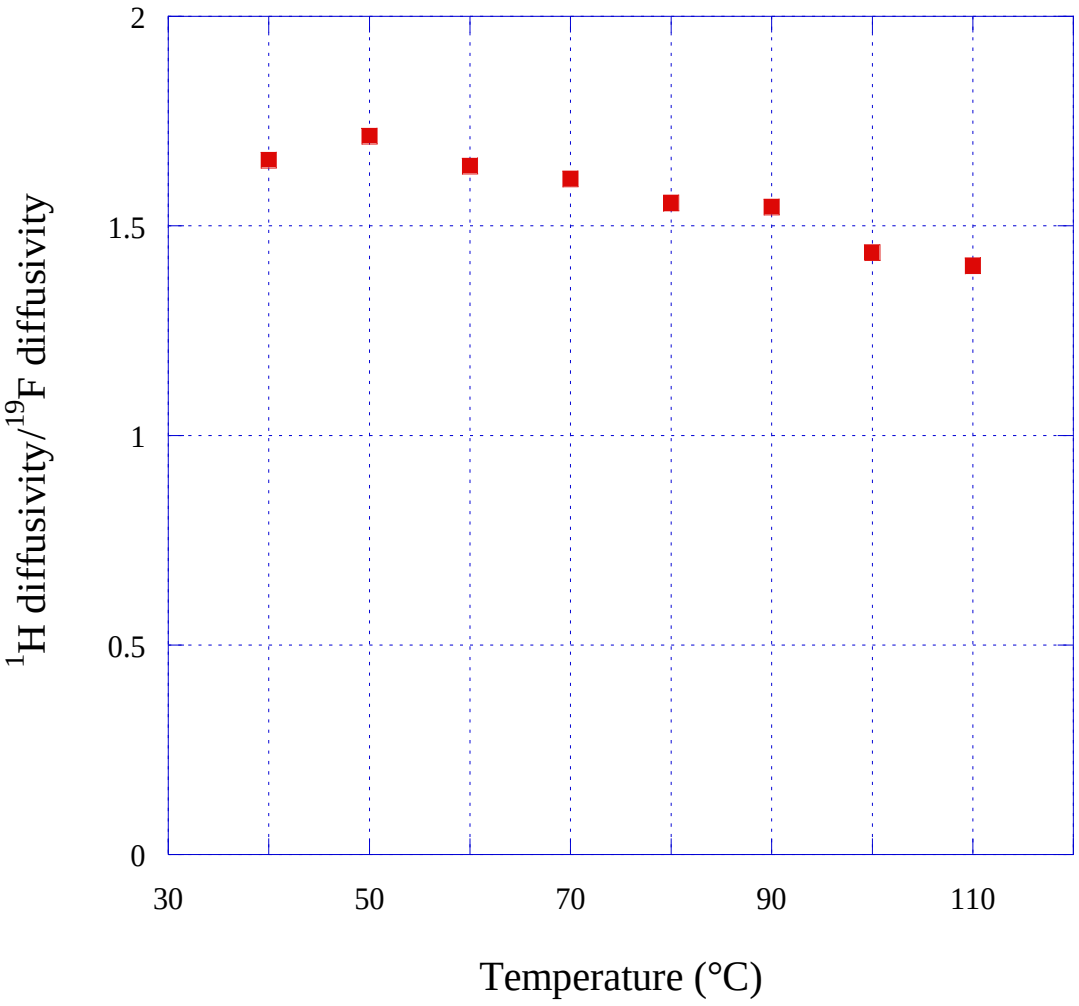

Figure 4.14 Ratio of ^{1}H diffusivity to ^{19}F diffusivity from 40 to 110°C. ^{1}H is observed to diffuse approximately 1.5 times faster than ^{19}F over the entire temperature range.

kJ/mol and that for viscosity of 26.9 $\pm$ 1.3 kJ/mol (for viscosity the slope is $+\frac{E_a}{R}$ since viscosity decreases with increasing temperature). The strong similarity in activation energies for all transport properties indicate that they are governed by essentially the same diffusive motion.

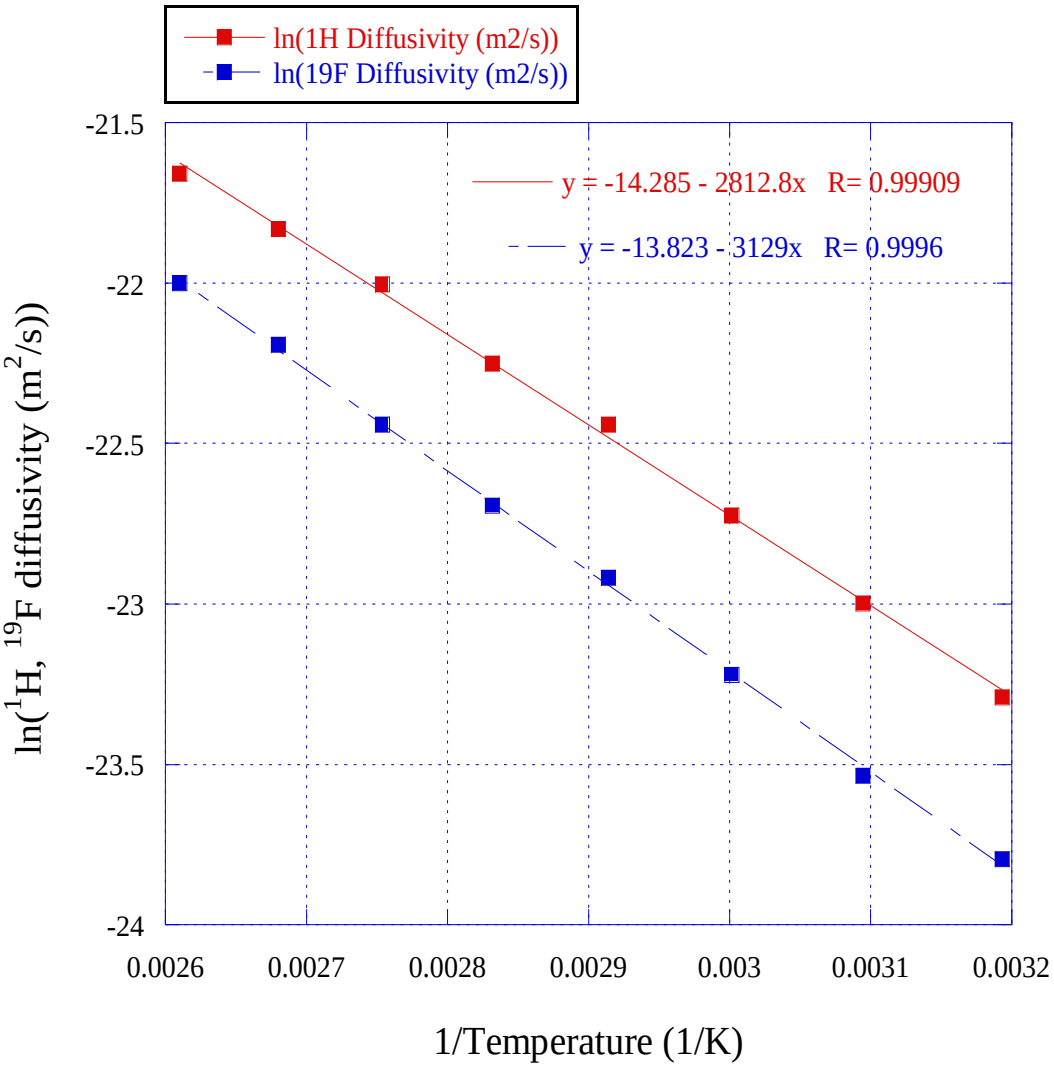

Figure 4.15 ln(Diffusivity) versus 1/Temperature for ^{1}H and ^{19}F showing Arrhenius behavior from 40 to 110°C.

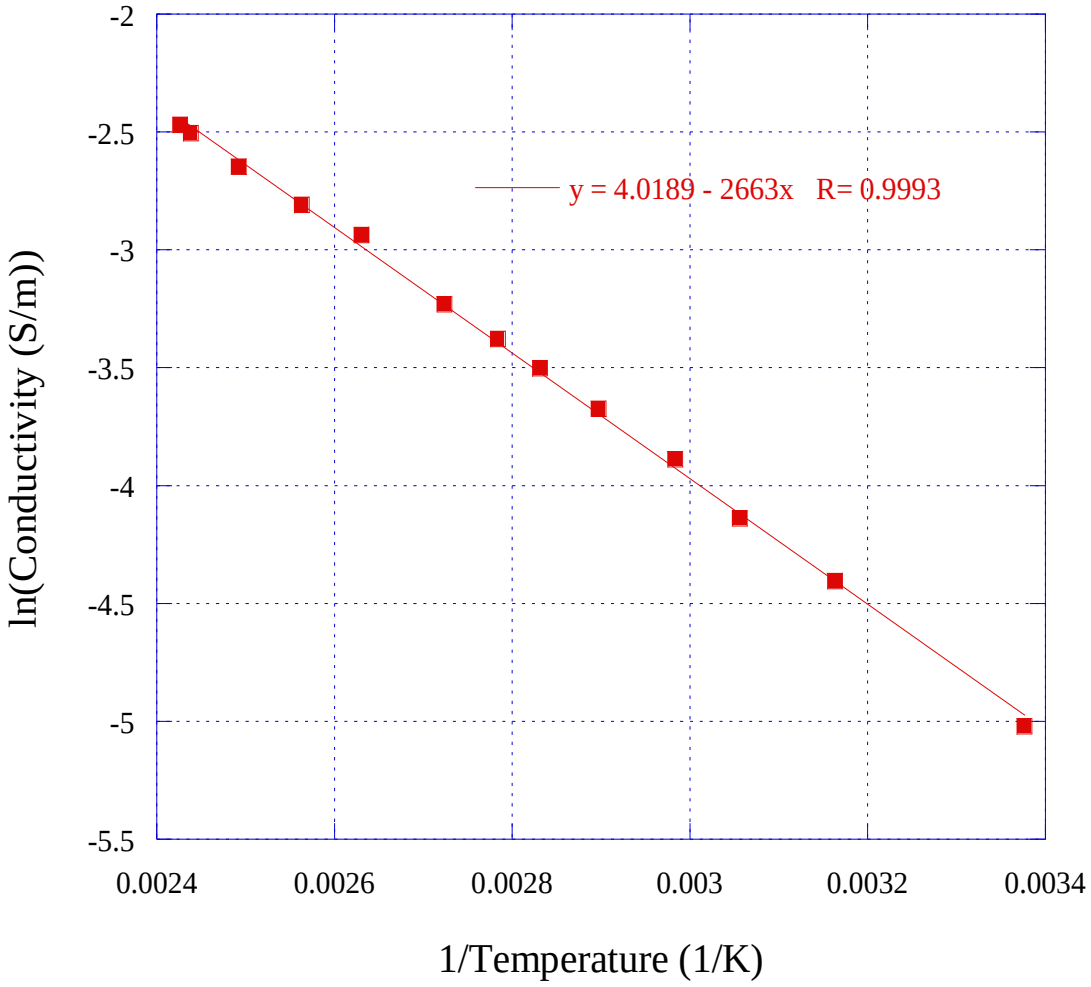

Figure 4.16 ln(Conductivity) versus 1/Temperature for TFMSA monohydrate showing Arrhenius behavior from 40 to 110°C.

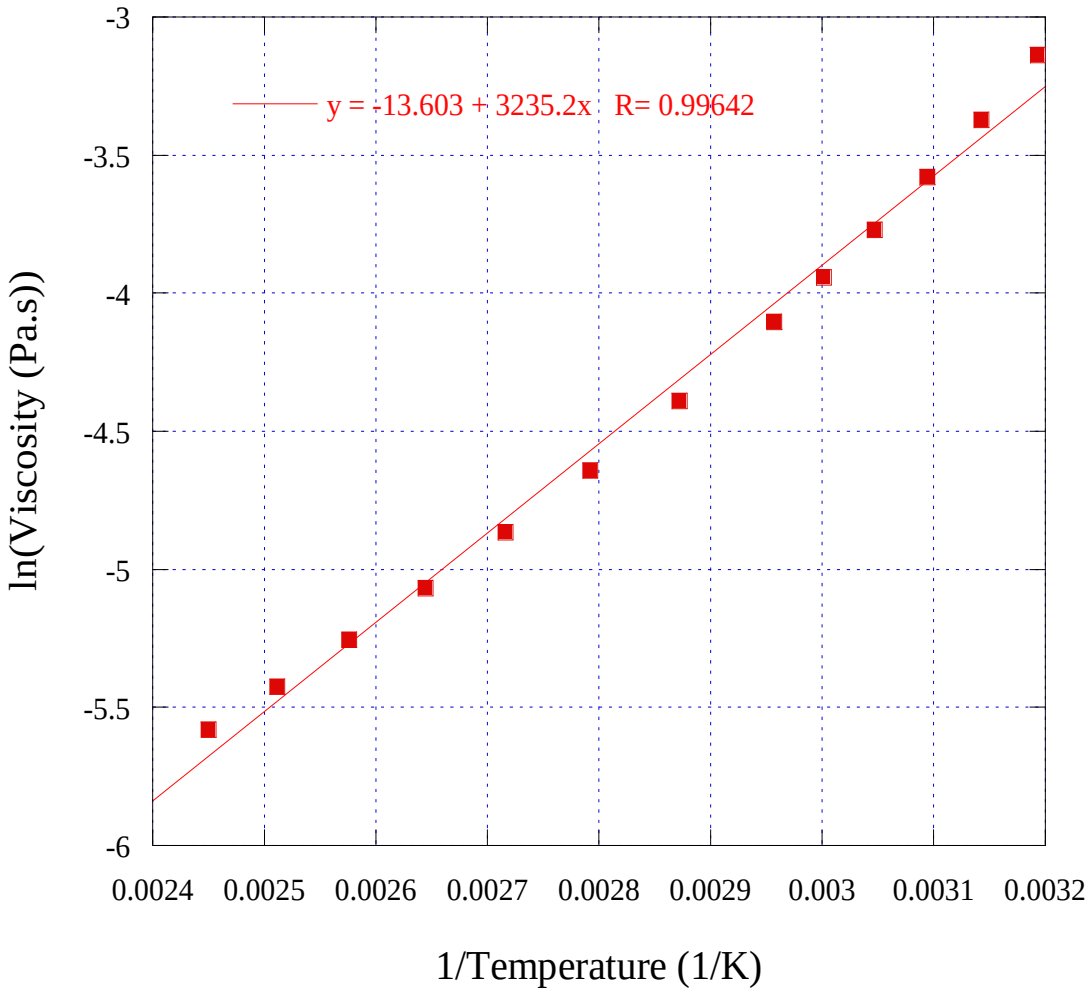

Figure 4.17 ln(Viscosity) versus 1/Temperature for TFMSA monohydrate showing Arrhenius behavior from 40 to 110°C.

4.4.3 Degree of dissociation of the charged species

Use of the Nernst-Einstein equation, under conditions of zero concentration gradient and an applied electric field, leads to a relation between conductivity and diffusivity of a charged species in a solution, given by:

$$k_i = \frac{c_i D_i z_i^2 F^2}{RT}, \qquad (4.1)$$

Where k_i is the conductivity of species *i* in S/m, c_i is the concentration of *i* in mol/m^3, D_i is the diffusion coefficient of *i* in m^2/s, z_i is the charge on ion *i*, F = 96485.3383 coulomb/mol is the Faraday constant, R is the gas constant, and T is the absolute temperature of the solution.

High resolution NMR spectra (Fig. 2) indicate strongly that TFMSA monohydrate solution is highly ionic and has two primary charged species involved in proton motion, namely the hydrated triflate anions ($CF_3SO_3^-$:H_2O) and the protons. The molar concentrations of both species are nearly the same, and in the event of complete dissociation of the two, are equal to the density of the solution divided by its molar mass. The density, ρ of TFMSA monohydrate was measured as a function of temperature in kg/m^3 and given its molar mass of 168.0953×10^{-3} kg/mol, we have

$$c_{anion} = c_{proton} = \frac{\rho}{168.0953\times10^{-3}} \text{ mol/m}^3, \tag{4.2}$$

Inserting the values of F and R in Eq. (4.1), and noting that $z_{anion} = -1$ and $z_{proton} = +1$, we get

$$k_{anion} = 6.6609\times10^{9}\,\frac{D_{anion}\rho}{T} \text{ S/m}, \tag{4.3}$$

and

$$k_{proton} = 6.6609\times10^{9}\,\frac{D_{proton}\rho}{T} \text{ S/m}, \tag{4.4}$$

therefore,

$$k_{net} = k_{anion} + k_{proton} = 6.6609\times10^{9}\,\frac{\rho}{T}(D_{anion} + D_{proton}) \text{ S/m}, \tag{4.5}$$

When the two charged species are completely dissociated, the measured conductivity of the solution should equal to k_{net}. If there is some association, the associated pair's mobility is unaffected by the electric field, lowering the effective values of c_{anion} and c_{proton} in the solution and hence the net conductivity. The ratio of the measured conductivity of the solution, $k_{measured}$ to k_{net} calculated from the measured diffusion coefficients and the density gives the degree of dissociation of the two species at a particular temperature. Figure 4.18 shows the plots of k_{net} and $k_{measured}$ versus temperature from 40 to 110°C and Figure 4.19 shows the degree of dissociation (%) of the two ions over that temperature range. As seen in Figure 4.19, the degree of dissociation is around 25% at 40°C and increases with temperature to around 29% at 110°C.

From the temperature-dependent degree of dissociation, we can estimate the difference in free energy between two states, the dissociated state and the associated state. If $[AB]$ and $[A]$ correspond to the associated ($CF_3SO_3H{:}H_2O$) state and the dissociated ($CF_3SO_3^-$ $+H_3O^+$) state, respectively, then, assuming that the numbers follow the Boltzmann distribution in thermal equilibrium, we get

$$\frac{[A]}{[AB]} = e^{-\frac{E_1 - E_2}{RT}}, \tag{4.6}$$

Where E_1 and E_2 are the free energies of the dissociated and the associated states respectively. From Equation (4.6) we get

$$\frac{[A]}{[A]+[AB]} = \frac{1}{1+e^{\frac{E_1 - E_2}{RT}}}, \tag{4.7}$$

or,

$$\text{Degree of dissociation, \%} = \frac{100}{1 + e^{\frac{\Delta E}{RT}}}, \tag{4.8}$$

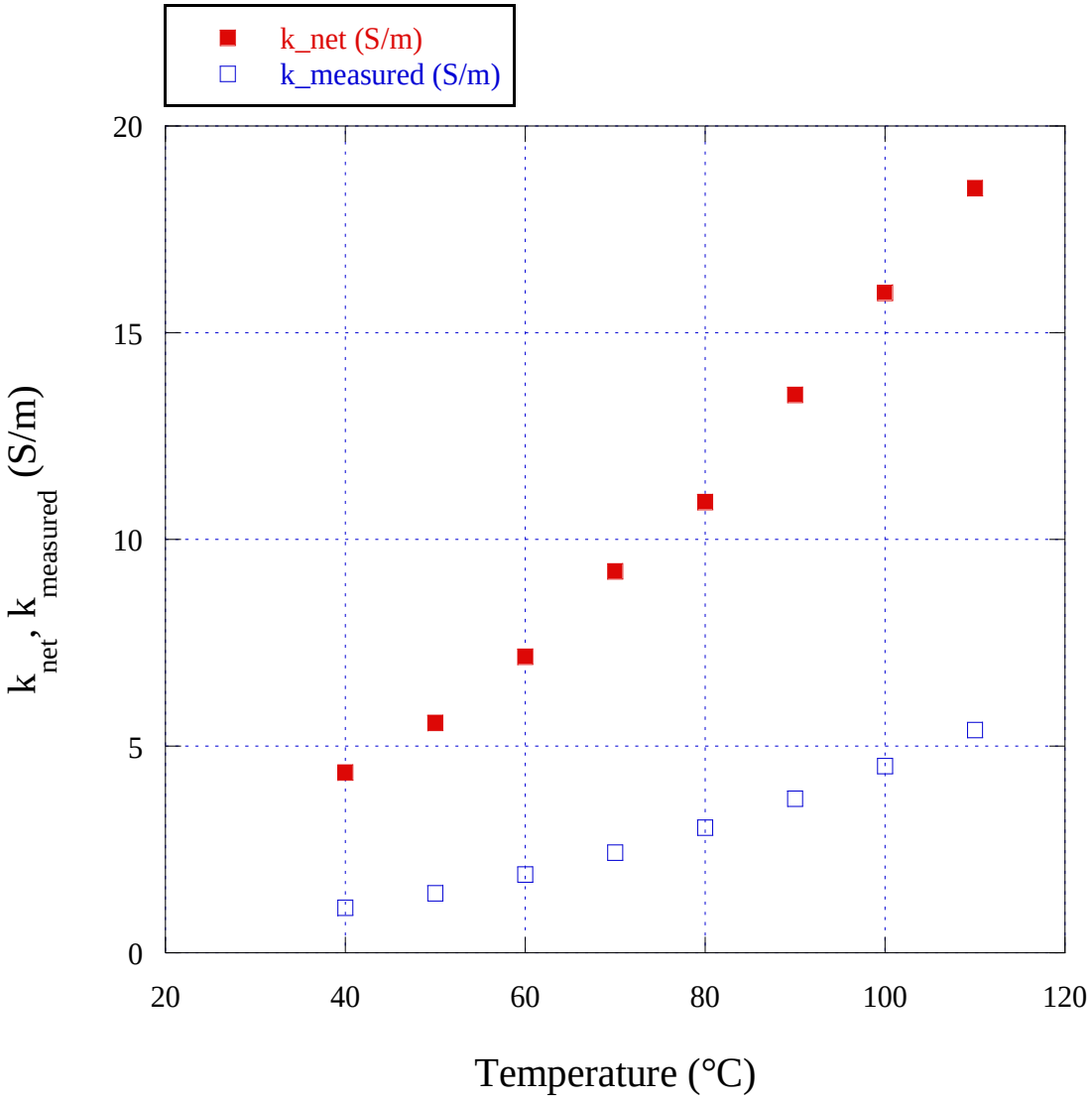

Figure 4.18 k_{net} and $k_{measured}$ for TFMSA monohydrate from 40 to 110°C.

where $E_1 - E_2 = \Delta E$, the difference in free energy between the dissociated and the associated ions. By fitting a curve corresponding to Equation (4.8) through our degree of dissociation versus temperature plot (Figure 4.19) we can estimate the value of ΔE.

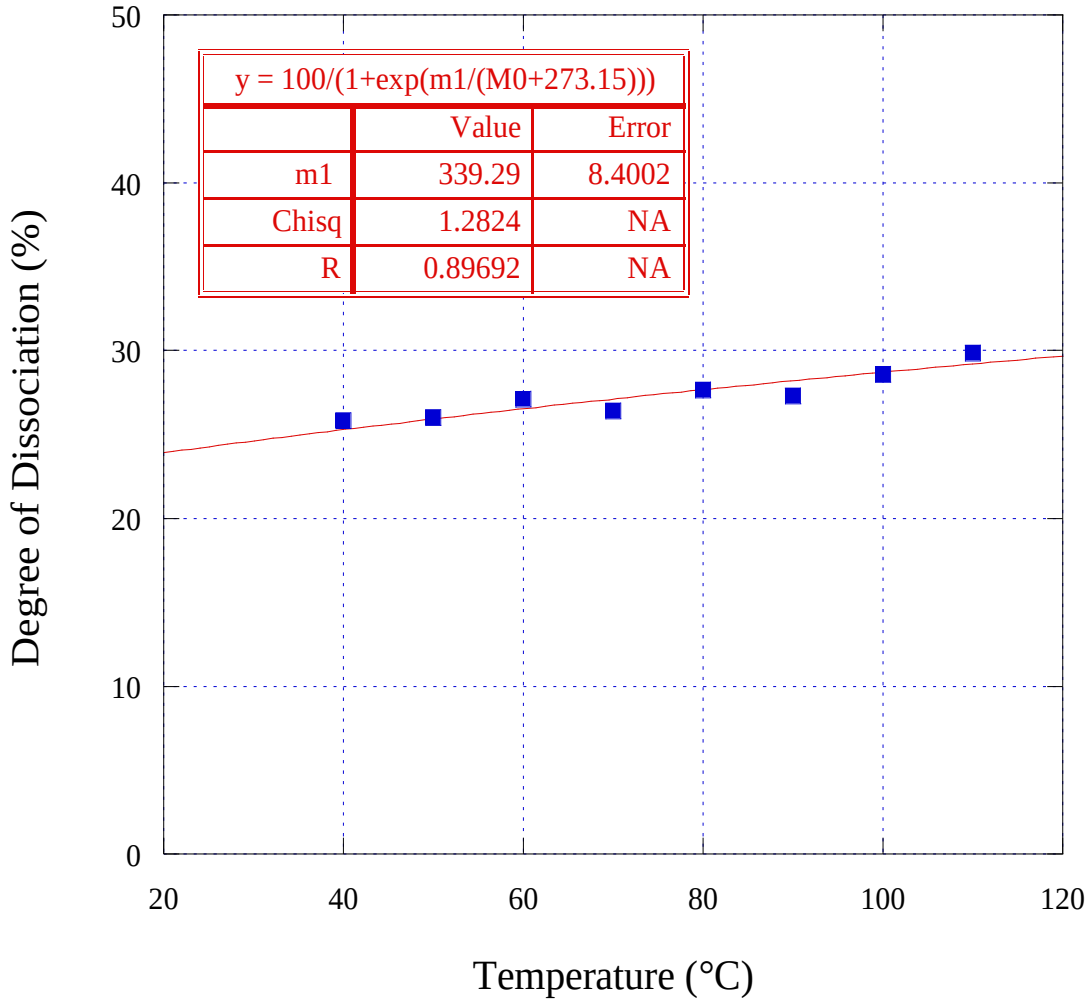

Figure 4.19 Degree of dissociation among charged species in TFMSA monohydrate from 40 to 110°C. A curve corresponding to Eq. (4.8) is fitted through the degree of dissociation versus temperature data to estimate the energy of dissociation.

From the curve fit we get

$$\frac{\Delta E}{R} = 339.29 \pm 8.4 \text{ K}, \tag{4.9}$$

or,

$$\Delta E = 2.8 \pm 0.14 \text{ kJ/mol}, \tag{4.10}$$

This is a relatively low value of dissociation energy considering the high degree of association (71-75%) of the two species.

4.4.4 Walden Plot

Figure 4.20 shows the position of TFMSA monohydrate among some typical ionic liquids on the Walden plot. As seen from the plot, the conductivity-fluidity behavior of TFMSA monohydrate is comparable to these ionic liquids.

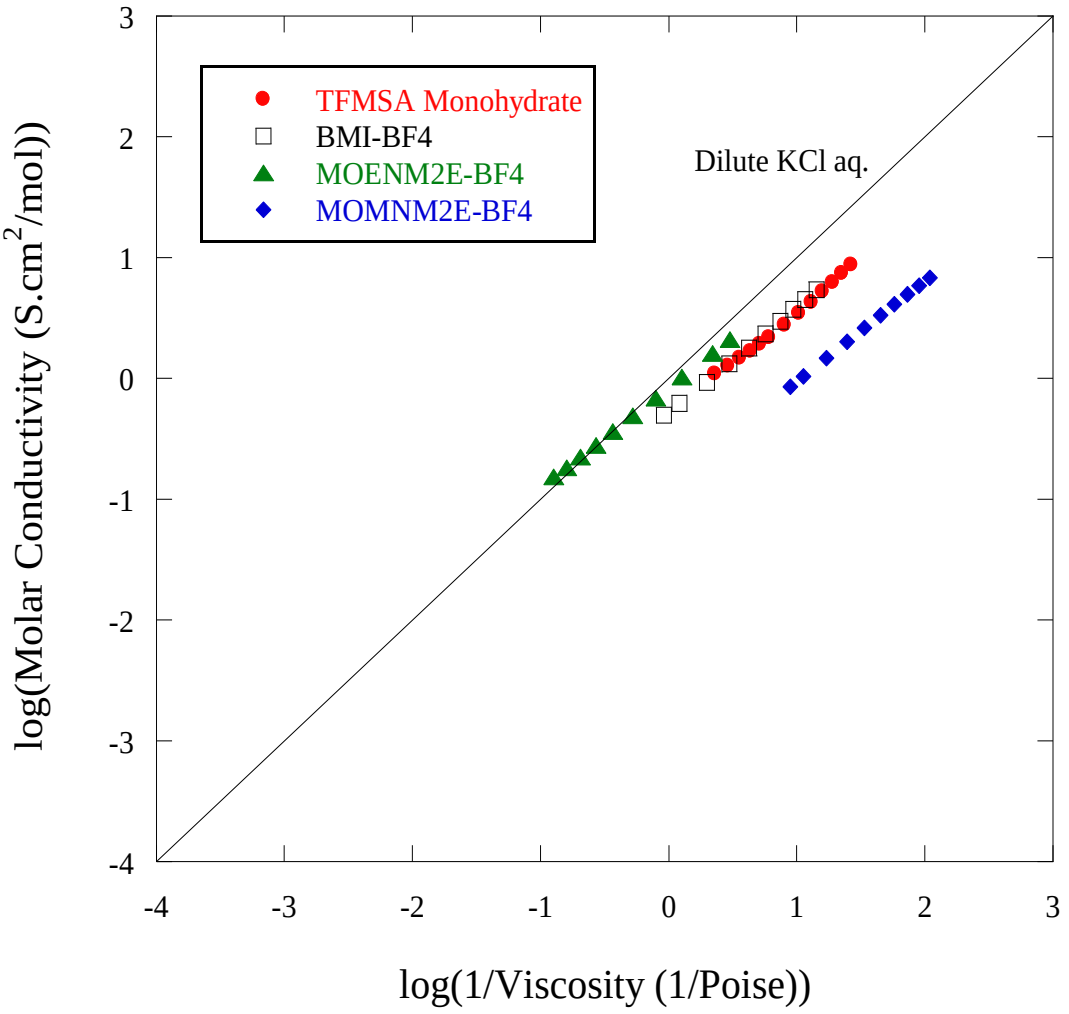

Figure 4.20 Walden Plot for TFMSA monohydrate and other ionic liquids[2]. Data for the monohydrate overlap with those for the tetrafluoroborate (BF4) of 1-n-butyl-3-methyl-imidazolium (BMI). The other two ionic liquids are tetrafluoroborates of methoxyethyl dimethyl ethyl ammonium (MOENM2E) and methoxymethyl dimethyl ethyl ammonium (MOMNM2E). Position of ideal line is fixed by data for dilute KCl aqueous solution.

[2] Data for ionic liquids kindly provided by J.-P. Belieres.

References

Barthel, J., Meier, R. and Conway, B. E., *J. Chem. Eng. Data* 44, 155-156 (1999).

Belieres, J.-P., Gervasio, D. and Angell, C.A., *Chem. Commun.* 46, 4799-4801 (2006).

Holz, M. and Weingartner, H., *J. Magnetic Resonance* 92, 115 -125 (1991).

Marzke, R. F., Gervasio, , D. and Ito, N. (unpublished data).

Mauritz, K. A. and Moore, R. B., *Chem. Rev.* 104, 4535-4586 (2004).

Springer, T. E., Zawodzinski, T. A. and Gottesfeld S., *J. Electrochem. Soc.* **138,** 2334-2342 (1991).

Zawodzinski, T. A., Davey, J., Valerio, J. and Gottesfeld, S., *Electrochim. Acta* **40,** 297-302 (1995).

CHAPTER 5

SUMMARY AND FUTURE WORK

The diffusivity of mobile protons in 2-FPTf was measured using pulsed field gradient NMR spectroscopy, and was found to increase from $(1.84 \pm 0.06 \times 10^{-11}$ m^2/s at 55°C to $(1.64 \pm 0.05) \times 10^{-10}$ m^2/s at 115°C. The diffusivity of 2-fluoropyridine fluorines was also measured, and increased from $(2.22 \pm 0.07) \times 10^{-11}$ m^2/s at 70°C to $(9.40 \pm 0.28) \times 10^{-11}$ m^2/s at 115°C. For TFMSA monohydrate, the diffusivity of protons increased from (7.67 $\pm 0.23) \times 10^{-11}$ m^2/s at 40°C to $3.92 \pm 0.12 \times 10^{-10}$ m^2/s at 110°C while the diffusivity of fluorines increased from $4.63 \pm 0.14 \times 10^{-11}$ m^2/s at 40°C to $2.79 \pm 0.08 \times 10^{-10}$ m^2/s at 110°C. High resolution NMR spectra indicated that the protons observed were bound to the TFMSA molecules. Those protons were found to diffuse approximately 1.5 times faster than fluorines over the entire temperature range, showing that in TFMSA monohydrate proton motion occurs via hopping from TFMSA molecule to molecule. The conductivity of 2-FPTf varied from 0.85 ± 0.03 mS/cm to 35.9 ± 1.08 mS/cm between 25 and 110°C. The conductivity of TFMSA monohydrate varied from 6.60 ± 0.2 mS/cm to 84.6 ± 2.5 mS/cm between 23 and 139 degC and its viscosity varied from 27.5 ± 1.4 mPa.s to 4.38 ± 0.22 mPa.s between 49 and 121.5 degC, in good agreement with literature values. Temperature dependences of the measured properties showed Arrhenius behavior with activation energies for proton diffusion, fluorine diffusion and ionic conduction for 2-FPTf above the melting point of 16.9 ± 0.8 kJ/mol, 48.0 ± 2.4 kJ/mol and 27.8 ± 1.4 kJ/mol respectively. Activation energies for proton diffusion, fluorine diffusion, ionic conduction and viscosity for TFMSA monohydrate were 23.4 ± 1.2 kJ/mol, 26.0 ± 1.3 kJ/mol, 22.1 ± 1.1 kJ/mol, and 26.9 ± 1.3 kJ/mol respectively. Interestingly, the activation

energies are very similar indicating that all the transport properties are governed by the same diffusive motion. The degree of dissociation of the charged species was calculated using the Nernst-Einstein relation, and varied from 13 to 24% for 2-FPTf and from 25 to 29% for TFMSA monohydrate over the temperature range. This shows a high degree of association of the TFMSA molecule in solution, but an estimate of its dissociation energy (based upon the small changes in cation and anion concentrations with temperature) yielded the relatively low value of 2.8 ± 0.14 kJ/mol.

In the future we would like to investigate the effect of sulfonic acid and water interactions in the conductivity of protons in TFMSA by measuring the proton and fluorine diffusivities and ionic conductivities of TFMSA over a wide range of water concentrations. Also, our measured ionic conductivity of 2-FPTf was higher than that measured by Jeffrey Thomson (Thomson 2010), by almost three times at 110°C. We would like to measure the conductivity of 2-FPTf again to check this discrepancy, and also to study its possible molecular origins further via NMR.

CHAPTER 6

FULL LIST OF REFERENCES

Abragam, A. *Principles of Nuclear Magnetism* (Oxford University Press, Oxford, 1978)

Adams, A., and Foley. R.T., *J. Electrochem. Soc.* 126, no. 5 (1979): 775-778.

Andrew, E. R. 1981. MAGIC ANGLE SPINNING IN SOLID-STATE NMR-SPECTROSCOPY. *Philosophical Transactions of the Royal Society a- Mathematical Physical and Engineering Sciences* 299 (1452):505-520.

Appleby, A. J. & Yeager, E. (1986). *Energy*, 1 1 (1 - 2), 137-152.

Arico, A. S., Srinivasan, S. & Antonucci, V. (2001). *Fuel Cells*, 1 (2), 133-161.

Bacon, F. (1969). *Electrochimica Acta*, 14, 569-585.

Barceloux, D. G., Bond, G. R., Krenzelok, E. P., Cooper, H. & Vale, J. A. (2002). *Journal of Toxicology, Clinical Toxicology*, 40(4), 415-446.

Bard, A.J. and Faulkner, L. R., *Electrochemical Methods, Fundamentals and Applications*, 2nd ed. (John Wiley and Sons, New York, 2001), Chap. 10, pp. 368-416. Cole-Parmer Technical Library,

Barthel, J., Meier, R. and Conway, B. E., *J. Chem. Eng. Data* 44, 155-156 (1999).

Belieres, J.P., Gervasio, D. , and Angell, C.A., *Chem. Commun.* 46**,** 4799-4801 (2006).

Belieres, J.-P., Gervasio, D. and Angell, C.A., *Chem. Commun.* 46, 4799-4801 (2006).

Chum, H.L., V.R. Koch, L.L. Miller, and R. A. Osteryoung. *J .Am .Chem. Soc.* 97 (1975): 3264.

Cropper, M. A. J., Geiger, S. & Jollie, D. M. (2004). *Journal of Power Sources*, 131(1-2), 57-61.

Dillon, R., Srinivasan, S., Arico, A. S. & Antonucci, V. (2004). *Journal of Power Sources*, 127(1-2), 112-126.

Fergus, J. W. (2004). *Solid State Ionics*, 171(1-2), 1-15

Fitzgerald, R. *Physics Today* 54 (2001): 22.

Greaves, T.L. and Drummond, C.J., *Chem. Rev.* 108, 206-237 (2008).

Grove, W. R. (1839). *Philosophical Magazine and Journal of Science*, 14, 127-130.

Grove, W. R. (1842). *Philosophical Magazine and Journal of Science*, 21, 417-420.

Hahn, E. L. 1950. SPIN ECHOES. *Physical Review* 77 (5):746-746.

Hemmes, K., Peelen, W. H. A. & De Wit, J. H. W. (1999). *Electrochemical and Solid-State Letters,* 2(3), 103-106.

Holz, M. and Weingartner, H., *J. Magnetic Resonance* 92, 115 -125 (1991).

Holz, M. and Weingartner, H., *J. Magnetic Resonance* **92,** 115 -125 (1991).

Hoogers, G. (2003). *Fuel Cell Technology Handbook*. CRC Press.

http://www.coleparmer.com/Techinfo/techinfo_home.asp

Hurley, F.H. *J. Electrochem.Society* 98 (1951): 207-212.

Ishizawa, M., Okada, S. & Yamashita, T. (2000). *Journal of Power Sources*, 8 6 (1 - 2), 294-297.

Kordesch, K., Gsellmann, J., Cifrain, M., Voss, S., Hacker, V., Aronson, R. R., Fabjan, C., Hejze, T. & Daniel-Ivad, J. (1999). *Journal of Power Sources*, 80(1- 2), 190-197.

Litster, S. & McLean, G. (2004). *Journal of Power Sources*, 130(1-2), 61-76.

Maricq, M. M., and J. S. Waugh. 1979. NMR IN ROTATING SOLIDS. *Journal of Chemical Physics* 70 (7):3300-3316.

Marzke, R. F., Gervasio, , D. and Ito, N. (unpublished data).

Mauritz, K. A. and Moore, R. B., *Chem. Rev.* 104, 4535-4586 (2004).

McLean, G. F., Niet, T., Prince-Richard, S. & Djilali, N. (2002). *International Journal of Hydrogen Energy*, 27(5), 507-526.

Minh, N. Q. (2004). *Solid State Ionics*, 174(1-4), 271-277.

Mond, L. & Langer, C. (1889). *Proceedings of the Royal Society*, 46, 296-304.

Ohno, H. *Electrochemical Aspects of Ionic Liquids.* New Jersey: John Wiley & Sons, Inc., 2005.

Penner, S. S., Appleby, A. J., Baker, B. S., Bates, J. L., Buss, L. B., Dollard, W. J., Fan, P. J., Gillis, E. A., Gunsher, J. A., Khandkar, A., Krumpelt, M., O'Sullivan, J. B., Runte, G., Savinell, R. F., Selman, J. R., Shores, D. A. & Tarman, P. (1995). *Energy*, 20(5), 331-470.

Random walk. (2015, November 18). In *Wikipedia, The Free Encyclopedia*. Retrieved 23:30, November 18, 2015, from https://en.wikipedia.org/w/index.php?title=Random_walk&oldid=691248156

Rogers, R.D., and K.R. Seddon. *Ionic Liquids Industrial Applications for Green Chemistry.* Washington D.C.: American Chemical Society, 2002.

Schultz, T., Zhou, S. & Sundmacher, K. (2001). *Chemical Engineering and Technology*, 24(12), 1223-1233.

Springer, T. E., Zawodzinski, T. A. and Gottesfeld S., *J. Electrochem. Soc.* **138,** 2334-2342 (1991).

Stejskal, E. O. and Tanner, J. E., *J. Chem. Phys.* **42**, 288 (1965).

Thomson, J.K., Dunn, P., Holmes, L., Belieres, J-P., Angell, C.A. and Gervasio,D. , *A Flourinated Ionic Liquid as a High-Performance Fuel Cell Electrolyte*, ECS Transactions, 13 (28), 21 (2008).

Thomson, J. K, *Electrochemical Reduction in Ionic Liquids: Applications for Fuel Cells and Photovoltaics*, Ph.D. Dissertation, Arizona State University, Tempe, Arizona (2010).

Vielstich, W., Lamm, A. & Gasteiger, H. (2003). *Handbook of Fuel Cells: Fundamentals, Technology and Applications*, vol. 1-4. John Wiley & Sons.

Vigier, F., Coutanceau, C., Perrard, A., Belgsir, E. M. & Lamy, C. (2004). *Journal of Applied Electrochemistry,* 34, 439-446.

Walden, P. "Bull. Acad. Sci." 1914: 405-422.

Wasserscheid, P. and Welton, T. (eds.), *Ionic Liquids in Synthesis,* 2nd ed. (Wiley-VCH, Weinheim, 2003).

Williams, M. C., Strakey, J. P. & Singhal, S. C. (2004). *Journal of Power Sources*, 131(1-2), 79-85.

Yuh, C.-Y. & Farooque, M. (2002). *Advanced Materials and Processes*, 160(7), 31-34.

Zawodzinski, T. A., Davey, J., Valerio, J. and Gottesfeld, S., *Electrochim. Acta* **40,** 297-302 (1995).